3 Nucleus-Nucleus Collisions – Compressed Baryonic Matter

Overview

The goal of the research program on nucleus-nucleus collisions at the new accelerator facility at GSI is the investigation of highly compressed nuclear matter. Matter in this form exists in neutron stars and in the core of supernova explosions. In the laboratory, super-dense nuclear matter can be created in the reaction volume of relativistic heavy ion collisions. A large fraction of the beam energy is converted into the excitation of baryonic resonances which subsequently decay into pions and nucleons. This mixture of nucleons, baryonic resonances and mesons is called hadronic matter. At very high temperatures or densities, the hadrons melt and their constituents, the quarks and gluons, form a new phase of matter, the so called quark-gluon plasma. The phases of strongly interacting matter are shown schematically in Figure 3.1.

The baryon density and the temperature of the fireball produced in heavy-ion collisions depend on the beam energy. In other words, by varying the beam energy one may, within certain limits, map the phase diagram of strongly interacting matter. By exploring the phase diagram, one probes the strong interaction and its underlying theory, Quantum Chromo Dynamics (QCD). In particular, fundamental properties of QCD such as confinement and the broken chiral symmetry, which is related to the origin of hadron masses, can be explored in heavy-ion collisions. A quantitative understanding of these two phenomena is still lacking and hence poses a challenge for future research. An experimental approach to these problems is to search for modifications of hadron properties in a dense and hot nuclear medium and for deconfined matter consisting of quarks and gluons.

In heavy-ion experiments at CERN-SPS and RHIC the QCD phase diagram is studied in the region of high temperatures and low net baryon densities. The experimental results provide circumstantial evidence for a new phase of matter existing above a temperature of about 170 MeV. In future heavy-ion experiments at the CERN-LHC this research program will be continued towards higher temperatures and smaller net baryon densities. These conditions prevailed in the early universe as it underwent a phase transition from quark-gluon matter to hadronic matter in the first micro-seconds after the big bang.

In the region of high baryon densities and moderate temperatures the QCD phase diagram is much less explored. Baryon densities of up to about 3 times that of nuclei are reached in heavy-ion collisions at the present SIS18 accelerator of GSI. The highest net baryon densities are expected for nuclear collisions in the beam energy range between 10 and 40 GeV/u. The analysis of the ratio of strange to non-strange mesons measured at AGS and CERN-SPS indicates a maximum abundance of strange baryons around 30 GeV/u. The energy range up to 15 GeV/u was pioneered at the AGS

in Brookhaven. In a second generation experiment the energy range from 10 to 40 GeV/u should be scanned searching for:

- in-medium modifications of hadrons in dense matter.
- indications of the deconfinement phase transition at high baryon densities.
- the critical point providing direct evidence for a phase boundary.
- exotic states of matter such as condensates of strange particles.

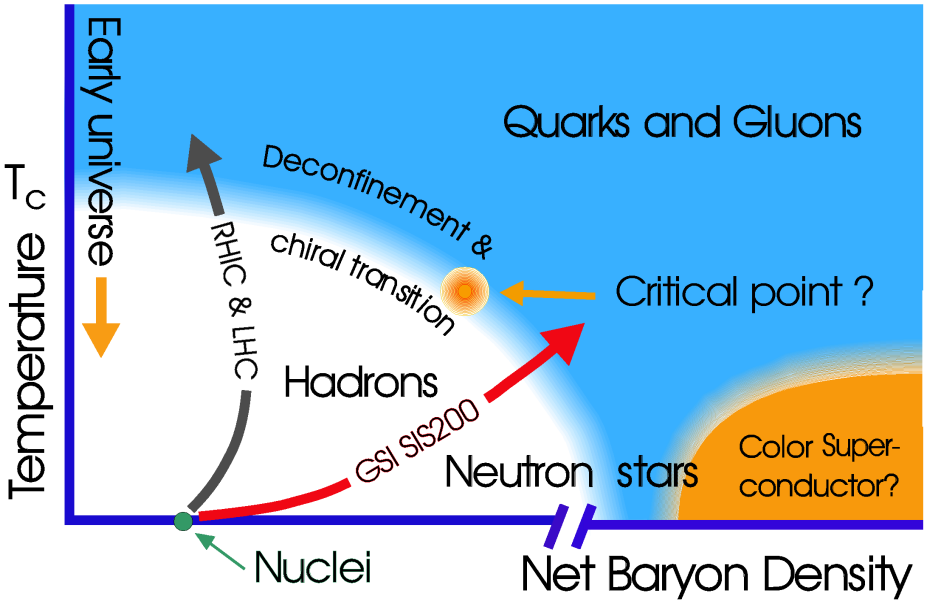

Figure 3.1: A schematic phase diagram of strongly interacting matter. The net baryon density is the density of baryons minus the density of antibaryons. Similar to water, nuclear matter exists in different phases as function of temperature and density. The "liquid" phase is realized in atomic nuclei at zero temperature and at saturation density (300 million tons/cm³). At low densities, the nucleons (i.e. protons and neutrons) behave like a gas. As the temperature is raised, the nucleons are excited into "baryon resonances". Furthermore, quark-antiquark pairs ("mesons") are produced. The hadronic phase is represented by the white area. At higher temperatures, a phase transition from hadronic matter to quark-gluon matter takes place ("deconfinement"). The transition temperature is about 170 MeV (at net baryon density zero) which is 130 thousand times hotter than the interior of the sun. Such conditions did exist in the early universe a few microseconds after the big bang and can be created in heavy ion collisions at ultra-relativistic energies as provided by the accelerators SPS (CERN), RHIC (Brookhaven) and the future LHC (CERN). In highly compressed cold nuclear matter – as it may exist in the interior of neutron stars – the baryons lose their identity and dissolve into quarks and gluons. The critical density at which this transition occurs, however, is not known. The same is true for the entire high density area of the phase diagram. At very high densities and low temperatures, beyond the deconfinement transition, a new phase is expected: the quarks are correlated and form a color superconductor. At the "critical point" the deconfinement/chiral phase transition is predicted to change its character. The new GSI facility permits the exploration of the "terra incognita" of the QCD phase diagram in the region of high baryon densities. This research program is complementary to the investigations performed at the RHIC facility at Brookhaven, USA, and at the SPS and in the future, the LHC facility (ALICE project) at CERN.

Our approach towards these goals is to measure simultaneously observables which are sensitive to high density effects and phase transitions. In particular, we focus on the investigation of:

- short-lived light vector mesons which decay into electron-positron pairs. These penetrating probes carry undistorted information from the dense fireball.
- strange particles, in particular baryons (anti-baryons) containing more than one strange (anti-strange) quark, so called multistrange hyperons.
- mesons containing charm or anti-charm quarks.
- collective flow of all observed particles.
- event-by-event fluctuations.

In the experiment particle multiplicities and phase-space distributions, the collision centrality and the reaction plane will be determined. For example, the study of collective flow of charmonium and multi-strange hyperons will shed light on the production and propagation of these rare probes in dense baryonic matter. The simultaneous measurement of various particles permits the study of cross correlations. This synergy effect opens a new perspective for the experimental investigation of nuclear matter under extreme conditions.

The measurements have to be performed systematically by varying the experimental conditions like beam energy, atomic number of the colliding nuclei, impact parameter and orientation of the reaction plane. This requires a dedicated accelerator with high beam intensities, large duty cycle, excellent beam quality and high availability.

The proposed Compressed Baryonic Matter (CBM) experiment is shown in Figure 3.2. The setup will measure both hadrons and electrons with large acceptance up to beam energies of about 40 GeV/u following a new concept: the particle tracking and momentum determination will be performed with high resolution in a magnetic field close to the target, whereas the particle identification will take place downstream the magnet. The apparatus consists of the following components:

- 7 layers of Silicon pixel and strip detectors in the field of a super-conducting magnet. These detectors provide an excellent track and vertex reconstruction which is crucial for the measurement of charmed D mesons.
- Ring-imaging Cherenkov detector (RICH) for electron identification.
- Transition radiation detectors (TRD) for identifying high-energy electrons.
- Resistive plate chambers (RPC) for time-of-flight measurement.

The detectors are based on modern technologies as developed for the experiments at LHC. GSI has expertise in designing TRD's (for ALICE at LHC) and RPC's (for the

FOPI detector at GSI). A large RICH detector (part of the HADES spectrometer) is operated at GSI. The HADES spectrometer will also be used in the reaction physics program at the future facility for beam energies between 2 and 7 GeV/u (see left part of Figure 3.2). The design, construction and commissioning of the CBM detector can be accomplished by 2009. The estimated costs amount to approximately 27 Mio. Euro. Physicists from more than 20 European and Asian universities and institutes have expressed their interest in the CBM project.

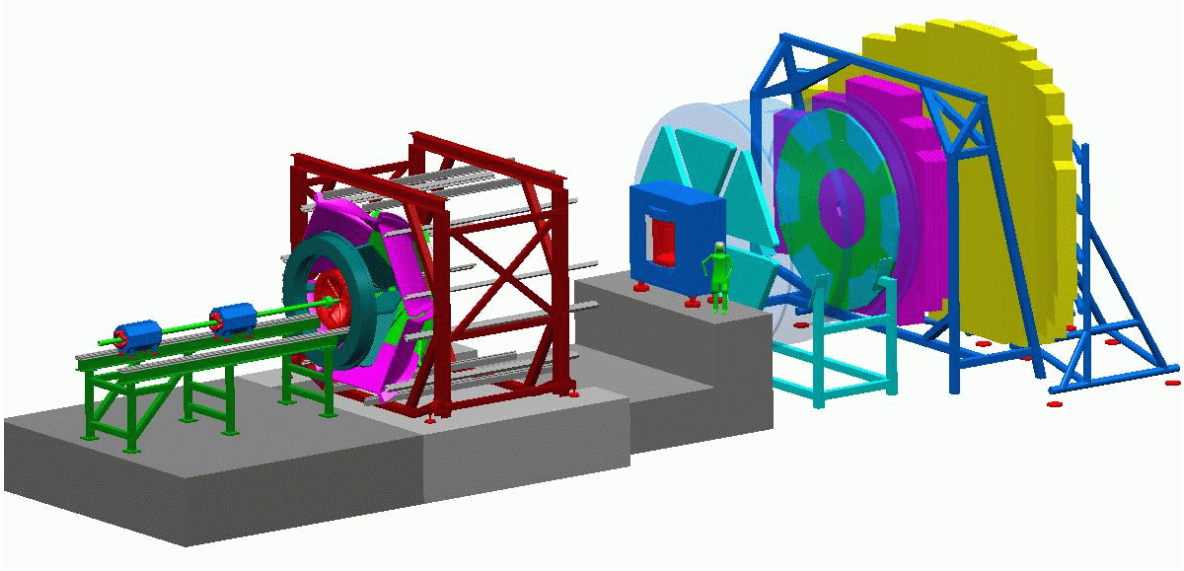

Figure 3.2: Sketch of the proposed experimental setup. The beam enters from the left hand side. The first device is the HADES detector which will be used (after some modification) to measure dilepton pairs and hadrons in the beam energy range up to about 7 GeV/u. The HADES target is placed at the entrance of the spectrometer. The Compressed Baryonic Matter (CBM) detector will measure dilepton pairs and hadrons with large acceptance up to beam energies of about 40 GeV/u. The CBM setup consist of a dipole magnet (blue), a RICH Detector (turquoise), a TRD detector (pink) and a RPC TOF wall (yellow). The Silicon tracker is mounted inside the magnetic field of the dipole. The CBM target is at the entrance of the magnet. The beam line optical system has to provide a focused beam either for the HADES or for the CBM detector.

3.1 The scientific case

3.1.1 Introduction

The strong interaction is a basic force of nature which plays a crucial role in the evolution of the universe and in the synthesis of elements. Strongly interacting matter – which constitutes more than 99% of the visible mass in our world – exists in different forms:

- quarks, the elementary constituents of matter which have not been observed as free particles.
- hadrons, composite particles like protons and neutrons (3 constituent quarks) and mesons (quark-antiquark pairs). Quarks are bound together by the exchange of gluons, the mediators of the strong force.
- atomic nuclei, consisting of up to about 270 protons and neutrons. These nucleons are bound by a short-range mutual attraction which is generated by the strong force leaking out from the nucleons.
- neutron stars, consisting of about 10^{57} neutrons which are bound by gravitation.

The quantitative understanding of the rich phenomenology of strong interaction physics is a fascinating challenge for modern fundamental research. This is the focus of the future accelerator facility at GSI.

Novel phases of strongly interacting matter, as illustrated in Figure 3.3, are expected to occur in the core of neutron stars, where the baryon density exceeds that of nuclei by up to a factor of 10. In this case, various competing forms of matter are predicted [1], such as condensates of mesons, a large abundance of hyperons (particles containing up, down and strange quarks) or a plasma of quarks and gluons. In particular, particles carrying strangeness are likely to play a crucial role in neutron stars. Moreover, strangeness may exist in the form of unconfined quarks in chemical equilibrium with up and down quarks and/or with hadrons, populating extended regions inside the neutron star. So far none of the proposed scenarios can be excluded by astronomical observations or theoretical considerations.

Further progress in the understanding of strongly-interacting matter at high densities requires new information (i) on the properties of hadrons in dense nuclear matter, (ii) on the deconfinement phase transition from hadronic to quark-gluon matter at high baryon densities, and (iii) on the nuclear equation of state at high baryon densities.

These aspects can be explored in heavy ion collisions which provide the unique possibility to create and investigate compressed nuclear matter in the laboratory.

Moreover, such experiments permit the study of fundamental properties of the strong interaction and its underlying theory, quantum chromodynamics (QCD).

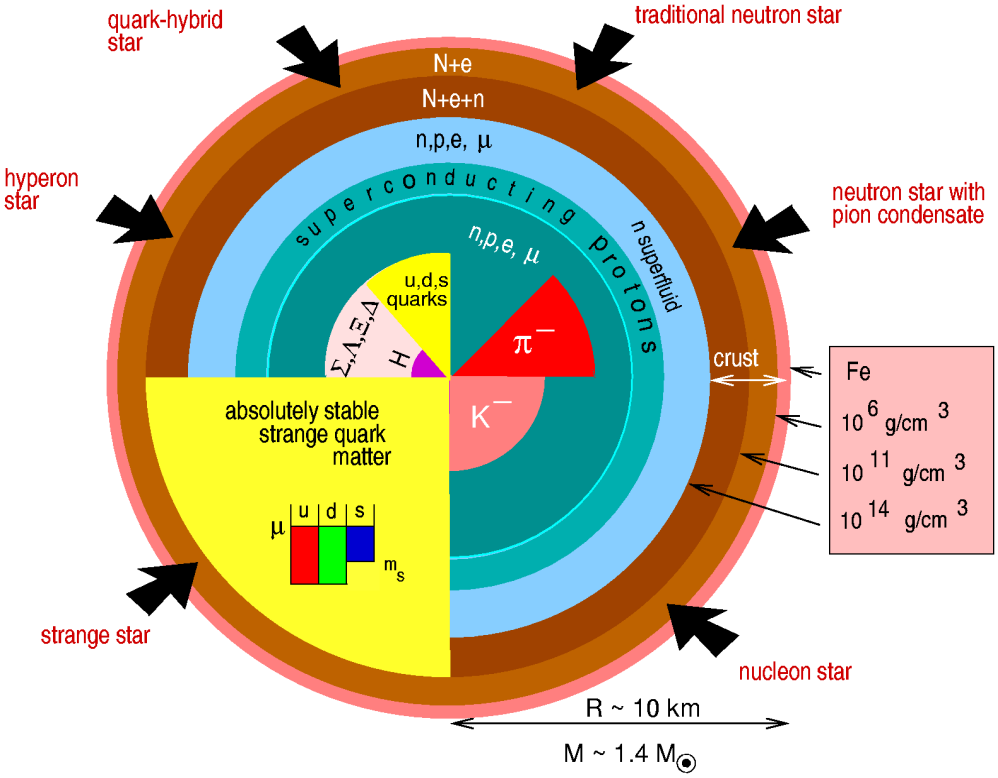

Figure 3.3: Possible novel phases and structures of subatomic matter: (i) a large population of hyperons (Λ,Σ,Ξ), (ii) condensates of negatively charged mesons with and without strange quarks (kaons or pions), (iii) a plasma of up, down, strange quarks and gluons (strange quark matter). Compilation by F. Weber [1].

QCD describes the dynamics of quarks and gluons [2]. It has the remarkable property that the interaction between two particles, quarks or gluons, becomes weak as the separation between them is reduced. This phenomenon, called asymptotic freedom, simplifies the description of certain high-energy processes and is the rationale behind the successful account of short distance phenomena in QCD. Conversely, at large distances, comparable to the size of the nucleon, the interaction between two quarks is strong. The amplification of the force with increasing distance is consistent with the phenomenon of **confinement**, i.e., the fact that only composite particles, built out of quarks and gluons ("hadrons"), are observed while isolated quarks and gluons are not. Due to the strong coupling, calculations in this regime (strong QCD) are very complex and difficult to control. Thus, although QCD is a very successful theory, basic aspects of the strong interaction, like confinement, are still not understood.

Another enigma of strong-interaction physics is the **origin of hadron masses**. It is remarkable that – on the one hand - the masses of the up and down quarks, the main constituents of stable matter, are very small when viewed at a short distance scale.

On the other hand, the hadrons that are composed of light quarks are much heavier than their quark constituents. The nucleon, for instance, is roughly 50 times heavier than the sum of the masses of its three basic constituents, the light up and down quarks. In other words, almost the total mass of matter around us is of dynamical origin – it is due to the strong interactions of the quarks and gluons in the hadrons. A quantitative understanding of this enormous mass generation within QCD has not yet been achieved[1]. It is clear, however, that **chiral symmetry**, a fundamental property of QCD for massless quarks, has a profound impact on hadron masses, through its spontaneous breakdown and the formation of condensates in the ground state ("vacuum").

Within the theory of QCD, the interaction of a quark with gluons does not change the orientation of the quark spin relative to its momentum. The "chirality" (handedness) of the quark is conserved: a particle is right (left) handed when its spin is parallel (anti-parallel) to its momentum. The conservation of chirality – which is a consequence of chiral symmetry – is strictly valid only in the limit of vanishing quark masses. In reality the chiral symmetry is approximate because the quark masses are not zero. However, since the masses of the up and down quarks are very small, the chiral symmetry is in fact a very useful concept in strong interaction physics. In vacuum the chiral symmetry is spontaneously broken, much like the breaking of the rotational symmetry of a ferromagnet below the Curie temperature. An observable consequence of this **spontaneous chiral symmetry breaking** is the absence of parity doublets[2] in the hadron spectrum and the existence of an almost massless Goldstone boson (the π meson). A detailed quantitative understanding of the mechanism of chiral symmetry breaking and its influence on the generation of hadron masses is still lacking.

A natural way to explore the phenomena of confinement and hadron mass generation is to heat and to compress nuclear matter. At high temperatures and densities one expects a new phase of matter, a quark-gluon plasma [3]. In this phase the quarks and gluons are deconfined and, at high temperatures, weakly interacting. Furthermore, in the quark-gluon plasma the chiral symmetry of QCD is eventually completely restored. Below the phase boundary, the quarks and gluons are confined in hadrons, forming an interacting hadron gas. During the first microseconds after the big bang the universe went through such a phase transition at very high temperatures but very low net baryon density. Simultaneously, the chiral symmetry was spontaneously broken. A similar deconfinement phase transition is expected to occur at high net baryon densities and very low temperatures, e.g. in the inner core of neutron stars. The phases of strongly interacting matter as function of temperature and net baryon density are illustrated in Figure 3.1.

---

[1]This mass generation should not be confused with that due to the conjectured Higgs boson which is responsible for the masses of quarks, electrons etc.

[2] In a chirally symmetric world hadrons come in pairs. The chiral partners differ in parity, i.e. their mirror symmetry is opposite.

There are robust theoretical predictions that chiral symmetry is at least partly restored in hot and dense hadronic matter. Under such conditions one expects hadron masses to be modified, since the masses of chiral partners must coincide as chiral symmetry is restored. Hence, the study of in-medium properties of hadrons is of great interest for exposing the relation between chiral symmetry and hadron masses: by investigating matter close to and beyond the phase transition, one can explore fundamental aspects of the strong interaction, such as confinement and the role of chiral symmetry in QCD.

In the laboratory, hot and dense hadronic matter can only be created in collisions between two heavy nuclei at high beam energies. Therefore, experiments with heavy ion beams are of particular importance for the study of deconfinement and chiral symmetry restoration. At ultra-high beam energies, heating dominates and the fireball consists mainly of quark-antiquark pairs. Such a hot, meson-dominated matter existed in the early universe. Corresponding measurements are performed at the Super Proton Synchrotron (SPS) at CERN and at the new Relativistic Heavy-Ion Collider (RHIC) in Brookhaven and are planned at the Large Hadron Collider (LHC) at CERN. In these experiments the region of the QCD phase diagram at high temperatures but low baryon densities is studied (see Figure 3.1).

A complementary experimental approach is to explore the properties of matter at high baryon densities and low temperatures. This region of the QCD phase diagram – which is to a large extent *terra incognita* both experimentally and theoretically – can be reached in heavy ion collisions at intermediate beam energies. Such reactions create a fireball with moderate temperatures and baryon densities several times the density of ordinary nuclear matter (i.e. the density in the interior of nuclei). As noted by F. Wilczek, the exploration of the high baryon density regime will put a new challenging perspective on the problems of confinement and chiral symmetry breaking [2].

The main focus of the new GSI experiment, which is proposed in the following, is to produce and to study highly compressed baryonic matter. In collisions between very heavy nuclei at energies around 25 GeV/u, a fireball is created with baryon densities several times the density of nuclei. This may be considered as a state of baryonic matter with collective properties and degrees-of-freedom very different from those of a dilute hadron gas. The key observables are so-called “penetrating probes” that provide almost undistorted information from the interior of the fireball – even at the time of its highest compression. In particular, electron-positron pairs stemming from the decay of short lived vector mesons represent a very promising diagnostic probe for the high baryon density regime below the deconfinement phase transition.

In collaboration with scientists from all over the world GSI plays a leading role in the field of relativistic heavy ion collisions. In particular, a rich experience exists in the investigation of dense nuclear matter as created in central collisions between two heavy nuclei at beam energies of up to 2 GeV/u. Data on strange meson production and the collective flow of nucleons – obtained with the KaoS and FOPI detectors at

GSI – provide information on the nuclear matter equation-of-state up to about three times the saturation density. Experimental results indicate that the properties of strange mesons are modified in dense nuclear matter. The modification of in-medium properties of vector mesons – which is expected for partially restored chiral symmetry – is experimentally studied with the Dilepton Spectrometer HADES at GSI. The HADES detector can measure hadrons and electrons emitted in heavy ion collisions also at higher beam energies up to about 7 GeV /u, and, hence, will be part of the experimental equipment at a new accelerator facility.

In central collisions between gold (lead) nuclei studied at the Alternating Gradient Synchrotron (AGS) in Brookhaven/USA and at the CERN-SPS one has found a maximum in the relative abundance of strange particles (i.e. particles which contain a strange quark) in the beam energy range between 15 and 40 GeV/u. This observation indicates that particular conditions are created in high-density fireballs. Calculations based on a statistical model predict that the ratio of strange to non-strange particles reaches a well defined maximum near a beam energy of 30 GeV/u. This effect is unique to heavy-ion collisions and consequently does not occur in proton-proton collisions. A detailed investigation of strange (and multistrange) particle production will help to unravel the nature of this genuine high baryon density phenomenon.

The new GSI facility will permit the experimental study of high baryonic densities with new observables. The proposed experiments will be able to identify particles which so far have not been measured in heavy ion collisions at beam energies between 2 and 30 GeV/u. These are light vector mesons, multistrange baryons (and antibaryons) and mesons containing charm quarks. Light vector mesons – measured via their decay into electron-positron pairs – will be used to probe the interior of the dense fireball. Baryons containing two or three strange quarks (or antiquarks) probe the strangeness content of the reaction volume. Mesons containing charm quarks – a degree-of-freedom which becomes energetically accessible with the new machine – offer the possibility to explore the deconfinement and chiral phase transition at high baryon densities. The simultaneous measurement of the phase-space distributions of all these particles requires a dedicated facility with an universal detector running for a sufficiently long period of time.

Based on the expertise of GSI in designing and constructing accelerators and large scale detectors we propose a second generation fixed target experiment with unique properties. It will permit simultaneous measurements of both hadrons and leptons and to identify various rare probes in a background of about thousand charged particles. These data will provide a comprehensive picture of the highly compressed baryonic fireball and thus shed light on the circumstances under which hadrons are dissolved and their masses are modified. Results from heavy ion collisions will be complemented by data obtained in collisions between antiprotons and nuclei (see the antiproton proposal). With the planned experiments at the new GSI facility one will be able to study a wide range of baryonic densities with new probes and thus contribute to the solution of the fundamental questions on confinement and the origin of hadron masses.

3.1.2 Matter under extreme conditions: what do we know ?

Because of asymptotic freedom, there are robust predictions for the properties of matter at very high temperatures and/or extremely high densities. At high temperatures, one finds a plasma of weakly interacting quarks and gluons [4], while at high densities and low temperatures, the quarks form a weakly interacting fermion system. Here, the attractive interaction between quarks leads to a color-superconducting phase, the QCD counterpart of an electrical superconductor [5].

At low densities and temperatures, on the other hand, reliable predictions for the properties of hadron matter are obtained using low-density expansions, which, depending on the channel considered, may remain valid even up to nuclear matter saturation density. A prominent example of the predictions obtained with such expansions is the density and temperature dependence of the quark condensate $\langle \bar{q}\, q \rangle$, an order parameter of the chiral transition which, as noted above, may have a profound impact on the hadron masses in matter [6]. In a phase where chiral symmetry is broken, $\langle \bar{q}\, q \rangle$ is non-zero, while in a chirally symmetric phase it vanishes. To leading order in the nucleon density, a model-independent relation for the quark condensate in matter can be derived [7,8]

$$\frac{\langle \bar{q}\, q \rangle(\rho_N)}{\langle \bar{q}\, q \rangle_0} = 1 - \frac{\sigma_N\, \rho_N}{f_\pi^2\, m_\pi^2} + \cdots \approx 1 - \frac{\rho_N}{3\,\rho_0} + \cdots . \qquad (1)$$

Here $\sigma_N \approx 45$ MeV is the pion-nucleon sigma term, ρ_N the nucleon density, ρ_0 the saturation density of nuclear matter, $f_\pi \approx 92$ MeV the pion decay constant, m_π the pion mass, and $\langle \bar{q} q \rangle_0$ the quark condensate in vacuum. Similarly, the leading dependence of the quark condensate on temperature is given by [9]

$$\frac{\langle \bar{q}\, q \rangle(T)}{\langle \bar{q}\, q \rangle_0} = 1 - \frac{T^2}{8 f_\pi^2} + \cdots \qquad (2)$$

These relations show that the quark condensate decreases with increasing baryon density or temperature: there is a tendency to restore chiral symmetry in hadronic matter. However, these relations cannot be used to predict the properties of hadronic matter when approaching the critical density or temperature, since they apply only at small densities or temperatures. In order to connect the high and low density regimes in a quantitative manner - and to describe for example the "melting" of the condensate - a new approach to QCD at intermediate densities is needed. Because of the large interaction strength in this regime, progress is possible only with input from dedicated experiments.

The situation is similar along the temperature axis of the phase diagram. At high temperatures one expects a weakly interacting quark-gluon plasma and at low temperatures a gas of hadrons. Unlike the high-density case, however, here the phase

transition can be studied in lattice simulations of QCD [10]. One finds a critical temperature of about $T_c \approx 170$ MeV for both the deconfinement and chiral transitions [10]. Whether the two transitions are inseparable also at non-zero baryon density is presently not clear, and this question is a subject of future studies. The energy density of a quark-gluon plasma at $T=T_c$ is, according to lattice calculations, approximately 1 GeV fm^{-3}, which is about six times the energy density of nuclear matter.

At low densities and temperatures one expects a gas of hadrons (and normal cold nuclear matter at zero temperature). Conversely, at high densities and relatively low temperatures, i.e., close to the density axis in the phase diagram, one expects a color superconducting phase. How the two regions in the phase diagram are joined with each other is one of the outstanding open problems in QCD. The exploration of the non-perturbative region near the phase transition is a very challenging problem, both theoretically and experimentally. Reliable estimates of the critical density and temperature for the onset of colour superconductivity are difficult. It seems unlikely that such a phase is formed in nucleus-nucleus collisions. Nevertheless, it may be possible to explore precursor effects of this transition, for example, modifications of the ratio of strange to nonstrange mesons [11,12]. This may give indirect information on the properties of the superconducting phase and on the confinement and chiral transition at low temperatures and high baryon densities.

Furthermore, lattice calculations suggest that the phase transition at vanishing baryon chemical potential is second order [10], while model calculations [5,13] predict that the chiral transition is first order at finite baryon density and low temperature. This would imply that there is a critical point on the phase boundary as indicated in Figure 3.1. In a recent paper, the critical point was predicted at a temperature of T = 160 MeV and a baryon chemical potential of μ_B = 725 MeV using finite scaling arguments on the lattice [14]. In the vicinity of such a point, the scalar correlation length becomes very large, and one expects large fluctuations. These would show up as increased fluctuations in observables, like the kaon to pion ratio, transverse momentum, rapidity density etc., measured event-by-event [15].

In summary, the properties of strongly interacting matter can be predicted for very low as well as for very high densities and temperatures. At intermediate densities – where the phase transitions are located – our knowledge is still poor. The regions close to the phase transitions are, however, of vital importance for obtaining a comprehensive understanding of confinement and chiral symmetry restoration. Further progress in this field of research requires input from new experiments, such as those proposed for the future GSI facility.

3.1.3 Probing the fireball: experimental situation

The connection between the QCD phase diagram and the conditions inside the fireball created in a heavy ion collision is far from obvious. The applicability of thermodynamics requires a chemically and thermally equilibrated system which is not realized in the early stage of the reaction. Furthermore, even if equilibration is rapidly achieved, the expansion of the fireball leads to a time dependence of the thermodynamic conditions. Particles which decouple from the system at distinct times because of differences in their mean free paths in hot an dense matter, would experience dissimilar conditions in the collision zone. One would expect these differences to influence observables like particle multiplicities and spectra. Nevertheless, the analysis of particle ratios in a thermal model of heavy ion collisions supports the picture with a sudden freeze-out of an equilibrium system at a given temperature and baryochemical potential [16]. It seems that the fireball has reached local chemical equilibrium by the time the particles cease to interact inelastically. This picture, remarkably simple as it appears to be, needs further detailed confirmation.

In Figure 3.4 we show a compilation of the freeze-out points in the QCD phase diagram obtained at different energy regimes [16,17,18,19]. The analysis of the SPS experiments indicates that in collisions between two lead nuclei at a bombarding energy of 158 GeV/u a fireball is produced which freezes out at a temperature close to the critical one of T=170 MeV at a baryon chemical potential of about μ_B=270 MeV. These values correspond to a baryon density of only about one third the density of nuclei ($\rho_0 \approx 0.16$ fm^{-3}). Most probably the fireball has spent some time in the deconfined (quark-gluon) phase before it expands and hadronizes into about 2000 pions, 200 kaons, 200 etas and other particles.

The main experimental goal is to investigate the properties of the fireball prior to chemical freeze-out. Heavy-ion experiments at CERN-SPS and RHIC search for signatures of the quark-gluon-plasma at ultra-relativistic beam energies, i.e. at high temperatures and low baryonic chemical potentials. Experimental findings such as the enhanced production of strangeness, in particular of multistrange hyperons, and the anomalous suppression of charmonium have been related to the transient existence of a deconfined phase. Penetrating probes like electron-positron pairs – which carry undistorted information from the interior of the hot and dense fireball – have been used to explore the in-medium spectral function of short-lived vector mesons. The data indicate a "melting" of the ρ meson, an effect which is expected if chiral symmetry is restored in hot and dense hadronic matter. Furthermore, event-by-event fluctuations of hadronic observables (K/π ratio, $\langle p_t \rangle$) have been studied in order to obtain information on whether the collision zone has undergone a phase transition from quark to hadronic matter. For a recent review of the data taken at AGS, CERN-SPS and RHIC see [20].

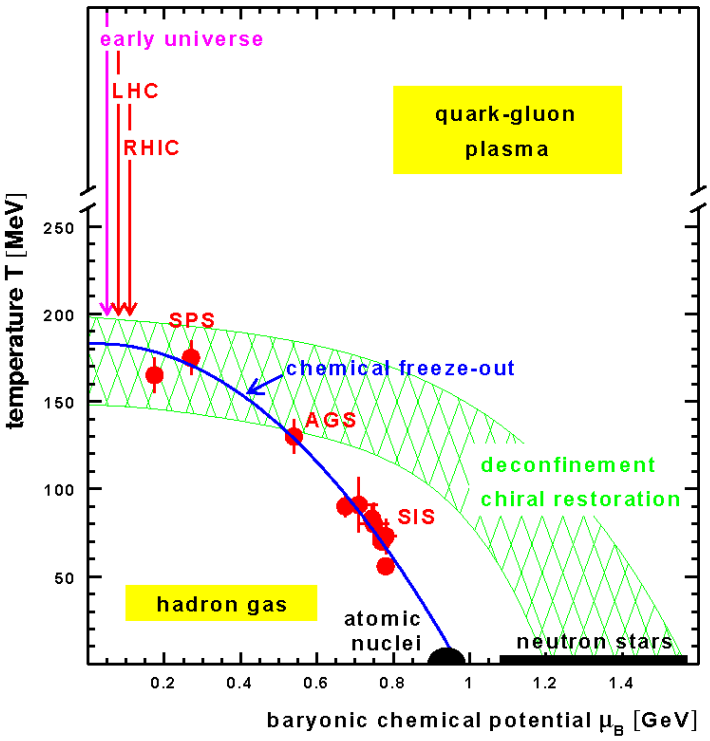

Figure 3.4: The phase diagram of strongly interacting matter. The symbols represent freeze-out points obtained with a statistical model analysis of particle ratios measured in heavy collisions. The solid line indicates the chemical freeze-out curve as function of temperature and chemical potential. Taken from [19].

At intermediate beam energies, e.g. at AGS, where high baryon densities at moderate temperatures are created in nucleus-nucleus collisions, none of these probes (multistrange hyperons, charmonium, di-electrons from light vector mesons) have been measured so far. Hence, a detailed study of high baryon density phenomena – including these rare probes – is still missing. It is the goal of the proposed nuclear reaction program at the future accelerator facility at GSI to provide a comprehensive set of experimental information.

A first glimpse of in-medium effects at baryon densities up to 3 ρ_0 has been seen in the experiments performed at the existing SIS18 accelerator at GSI. In particular, data on the yield and the propagation of strange particles in heavy-ion collisions at beam energies close to threshold provide evidence for a modification of the effective mass of kaons and antikaons in dense baryonic matter. The HADES experiment will perform detailed studies of in-medium effects on vector mesons by measuring electron-positron pairs.

Results from heavy-ion experiments on the production of strange mesons, multistrange baryons (Ξ, Ω), charmonium (J/ψ, ψ') and light vector mesons (ρ, ω, φ) will be briefly reviewed in the following.

3.1.3.1 Strange particles

The effective mass of strange mesons is predicted to be substantially modified in (dense) nuclear matter [21,22,23]. As a consequence, the production and propagation of kaons in heavy ion collisions – in particular at beam energies close to threshold – are expected to be sensitive to the baryonic density. Experimental evidence for strong kaon potentials in the nuclear medium has been found in experiments performed by the KaoS and FOPI collaborations at SIS/GSI. An example is shown in Figure 3.5 which presents the K^+ and K^- multiplicity densities dN/dy and their ratio for near central collisions as a function of rapidity (the value y_{cm} = 0 corresponds to midrapidity and y_{cm} = ±0.89 to projectile or target rapidity).

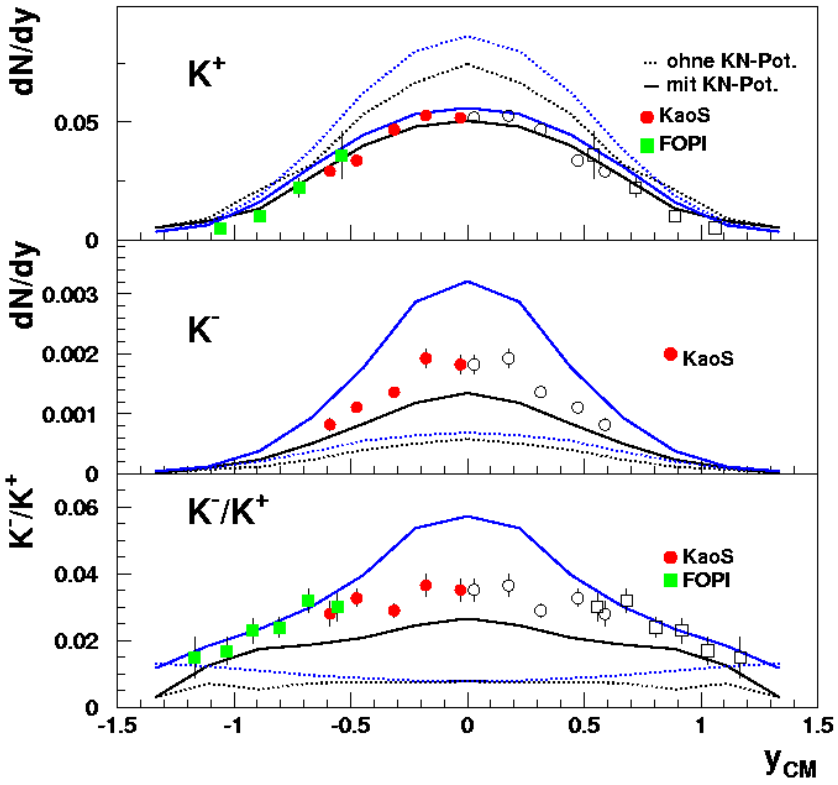

Figure 3.5: Multiplicity density distributions of K^+ (upper panel) and K^- mesons (center panel) for near-central Ni+Ni collisions at 1.93 GeV/u. Circles: KaoS data [24], squares: FOPI data [25,26]. The measured data (full symbols) are mirrored at y_{cm}=0 (open symbols). Lower panel: K^+/K^- ratio. The data are compared to transport calculations (blue lines [27], black lines [28]). Solid lines: with in-medium effects. Dotted lines: without in-medium effects.

The data [24,25,26] are compared to results of transport calculations performed by the groups from Stony Brook [27] (blue lines) and Giessen [28] (black lines). The dashed lines represent the results of calculations with bare (vacuum) kaon and antikaon masses. These calculations clearly overshoot the K^+ and undershoot the K^- data and thus demonstrate the need to take in-medium effects into account. When assuming an enhanced in-medium K^+ mass (which corresponds to a repulsive K^+N potential) the data can be reproduced (see solid lines in the upper panel). In contrast, the in-medium

K^- mass has to be reduced (corresponding to an attractive K^-N potential) in order to enhance the K^- yield (solid lines, center panel).

The K^-/K^+ ratio is strongly enhanced in nucleus-nucleus collisions as compared to nucleon-nucleon collisions [29]. Another observable sensitive to in-medium effects is the azimuthal angle distribution of kaons. Experimentally one has found in Au+Au collisions at 1 GeV/u that K^+ mesons are emitted preferentially perpendicular to the reaction plane at midrapidity [30]. Moreover, K^+ mesons with low transverse momenta are emitted into the reaction plane oppositely to the nucleons in Ru+Ru and Ni+Ni collisions [31]. These observations represent an independent experimental signature for a repulsive in-medium K^+N potential. Within transport calculations, both the yields and the azimuthal emission patterns of K mesons are described consistently when taking the in-medium modifications of kaons and antikaons into acount [28,32,33].

The understanding of the in-medium properties of kaons is needed in order to extract information on the nuclear compressibility from kaon yields. Recent measurements of the K^+ excitation function in Au+Au and – as a reference system – in C+C collisions provide evidence for a soft nuclear equation-of-state [34,35].

The excitation function for strange meson production (normalized to the pion yield) in heavy ion collisions exhibits a very intriguing feature in the beam energy range of the future accelerator at GSI. Figure 3.6 shows the ratio of K^+ and π^+ meson yields as function of beam energy in Au+Au (Pb+Pb) collisions [36,37]. The K^+/π^+ ratio seems to have a maximum between top AGS energy (10.7 GeV/u for Au beams) and the lowest CERN-SPS energy used so far (40 GeV/u). It is presently a matter of debate whether this non-monotonic behavior of the K^+/π^+ ratio is caused by a phase transition [38] or not. A statistical model description of heavy ion collisions predicts that the yield of strange to nonstrange particles exhibits a well defined maximum around a beam energy of 30 GeV/u [39]. This enhancement - which is not observed in proton-proton collisions – indicates that collective effects dominate strangeness production in this energy regime. The NA49 collaboration plans a measurement at 20 GeV/u in order to find the maximum of the excitation function. However, it is clear that detailed experimental studies – which include the measurement of multistrange particles – are needed to elucidate the origin of the enhanced strangeness production.

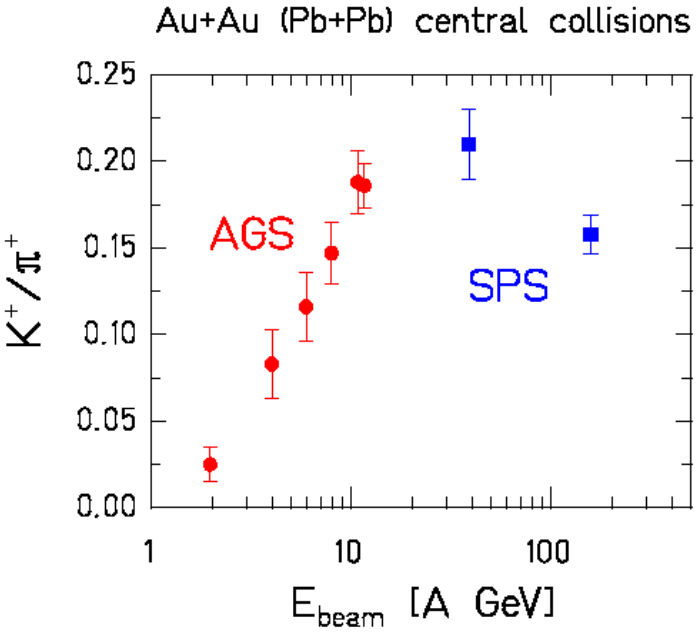

Figure 3.6: Ratio of K^+ and π^+ meson yields as function *of beam energy for central Au+Au (Pb+Pb) collisions. The data were measured by the collaborations E899/E917 [36] at the AGS and by NA49 at CERN-SPS [37].*

Enhanced production of strangeness has been proposed as a signal for the transient existence of a deconfined phase of quarks and gluons in nucleus-nucleus collisions at ultrarelativistic energies [40]. The idea is that the production of strange quark pairs is energetically favored in the quark-gluon plasma as compared to hadronic matter. The enhancement is expected to be most pronounced for particles containing two or even three strange quarks such as Ξ and Ω. Up to now multistrange hyperons have been measured only at CERN-SPS by the NA49 and WA97/NA57 collaborations [37,41]. The WA97/NA57 setup essentially consists of a silicon tracking telescope placed inside a magnetic field which measures position and momentum of the decay products of the hyperons: Ξ (ssd) → Λπ and Ω (sss) → ΛK (with Λ → pπ). This permits a determination of the invariant hyperon masses without identifying the decay products. Figure 3.7 shows the multiplicity of hyperons produced in Pb+Pb as compared to p+Be collisions normalized to the number of participating nucleons. The enhancement factor increases with the strangeness content of the particles up to a value of 15 for Ω^+ and Ω^-. This characteristic behavior is expected if a Quark-Gluon-Plasma is produced in heavy ion collisions.

On the other hand, multistrange hyperons may be produced in nucleus-nucleus collisions by multistep processes like $K^-\Lambda \rightarrow \Xi^-\pi^0$ and $K^-\Xi^- \rightarrow \Omega^-\pi^-$. These collisions are favored in large collision systems and at high densities. Moreover, thermal models reproduce the measured particle ratios including Ξ/Λ and Ω/Ξ assuming a chemical freeze-out temperature of about 170 MeV, a baryon chemical potential of $\mu_B \approx 270$ MeV and a strangeness chemical potential of $\mu_S \approx 70$ MeV [16]. Whether the required fast chemical equilibration is driven by the deconfinement phase transition or by enhanced in-medium hadronic reaction rates is still an open question. The $\Omega\overline{N}$ channel, for instance, may be rapidly populated also by the fusion of three kaons [42].

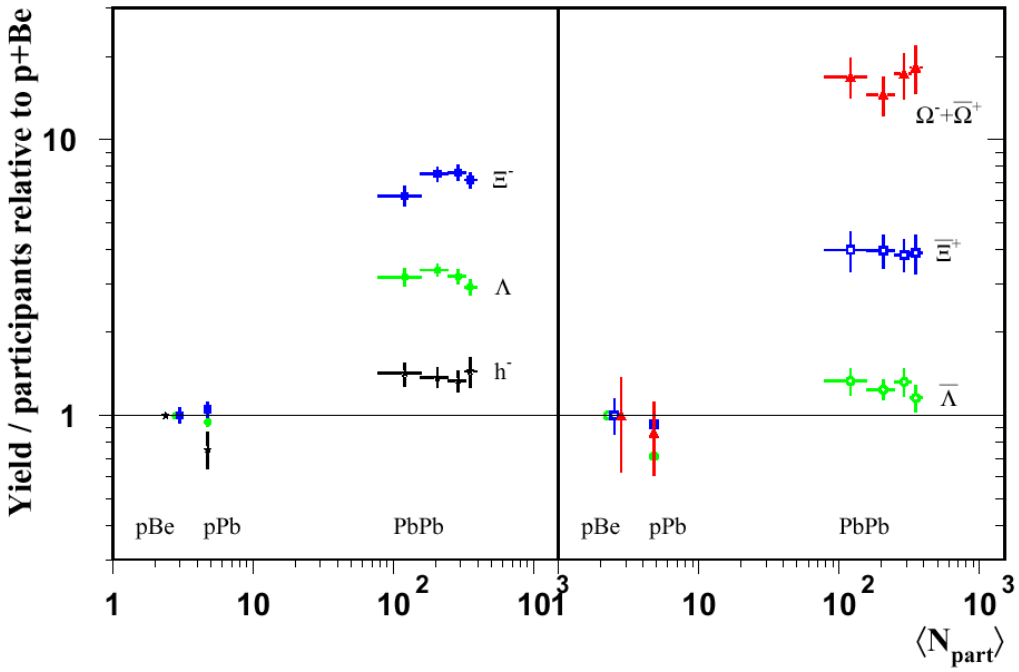

Figure 3.7: Hyperon yield per participating nucleon relative to p+Be collisons measured in Pb+Pb collisions at 158 GeV/u by WA97 [41]

3.1.3.2 Penetrating probes: lepton pairs from vector mesons

Short lived neutral vector mesons with dilepton decay channels are very promising probes of in-medium effects. If they decay inside the dense collision zone, their in-medium spectral functions are reflected in the invariant mass spectrum of the electron-positron pairs. Due to the long mean free path of the leptons, the information carried by the e^+e^- pair is not distorted by the surrounding medium. The deduced modification of the spectral function might be related to the expected (partial) restoration of chiral symmetry in the dense medium.

Pioneering experiments have been performed in nuclear collisions with the Dilepton Spectrometer (DLS) at the BEVALAC in the beam energy range of 1 – 2 GeV/u [43]. Figure 3.8 shows the cross section for the electron-positron pair production as function of the invariant mass for Ca+Ca collisions at 1 GeV/u in comparison with results from transport calculations [28]. The data indicate an enhancement of the dielectron yield at low invariant masses compared to a calculation with in-medium effects neglected. However, even when in-medium modifications of the ρ meson spectral function are taken into account, the data cannot be reproduced by the calculations. Thus a consistent interpretation of the DLS results has not been reached so far. A re-measurement of this reaction with the new HADES spectrometer at SIS/GSI, which has gone into operation, is eagerly awaited.

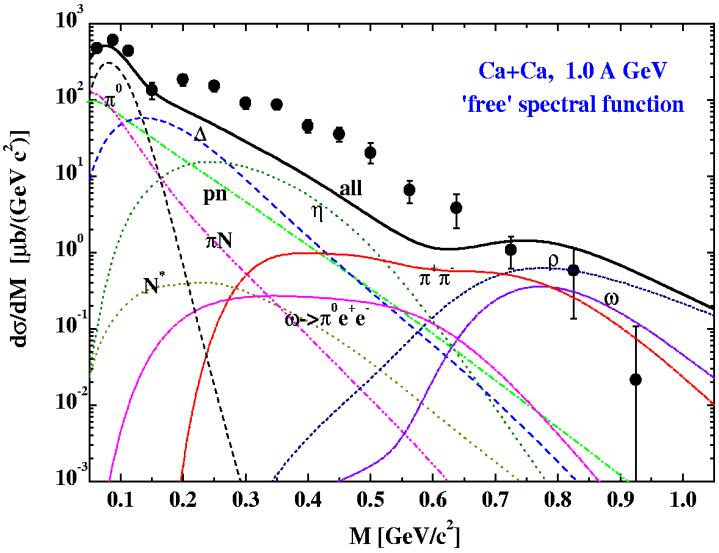

Figure 3.8: Production cross section of electron-positron pairs as function of their invariant mass measured in Ca+Ca collisions at a beam energy of 1 GeV/u by the DLS collaboration [43]. The curves represent contributions from different physical sources as calculated with a transport code [28].

In the energy range of the AGS no heavy-ion dilepton experiment exists up to now. At the CERN-SPS, dielectron invariant mass spectra have been measured in S+Au collisions at 200 GeV/u/c and in Pb+Au collisions at 158 GeV/u/c by the NA45/CERES collaboration [44]. The core of the experiment is a RICH detector which recently was supplemented by a TPC. The results of the measurements are presented in Figure 3.9 which shows the dielectron invariant mass spectrum measured in Pb+Au collisions at 158 GeV/u in comparison to the expected yield from known hadronic sources (as indicated). In the mass range of 0.2 – 0.6 GeV the data exceed the standard "hadronic cocktail" significantly. Whether this enhancement is caused by a shift or a broadening of the ρ meson spectral function, by thermal radiation from the quark-gluon plasma or by some hitherto unknown source is not clear at present [45].

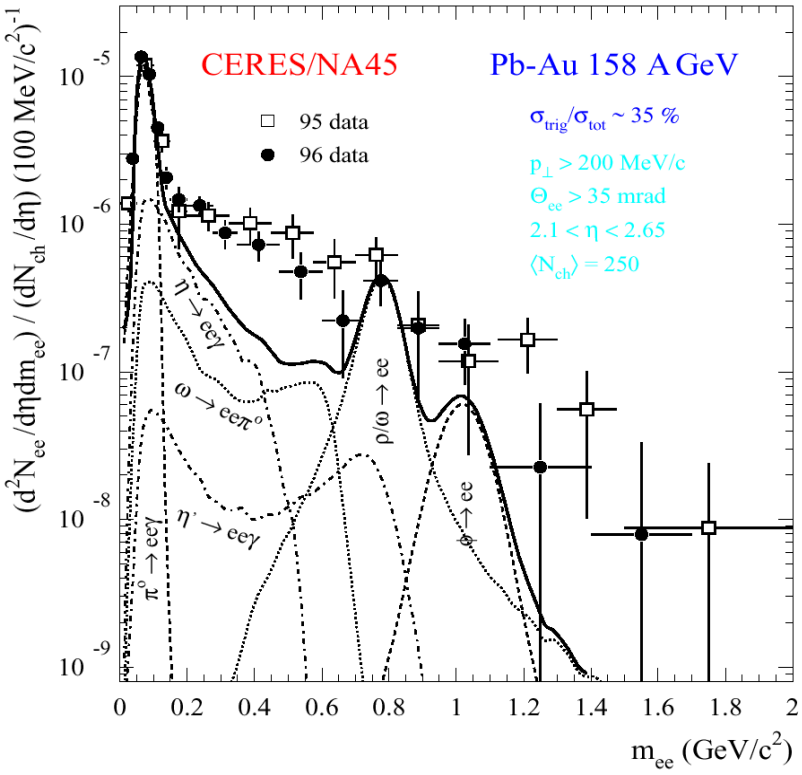

Figure 3.9: Dielectron invariant mass spectrum measured in Pb+Au collisions at 158 GeV/u in comparison to the expectation for hadronic sources [44].

3.1.3.3 The charm of hot and dense matter

The production and propagation of charm in heavy ion collisions is expected to be a particularly sensitive probe of the hot and dense medium. The created $c\bar{c}$ pairs either propagate as charmonium (hidden charm) or pick up light quarks to form pairs of D and $\overline{D}$ mesons (open charm).

The suppression of charmonium is predicted as a signature for the quark-gluon plasma [46]. The free color charges in the deconfined phase are expected to screen the mutual attraction of the charmed quarks and hence prevent the formation of charmonium states. Charmonium production in heavy ion collisions has been measured at the CERN-SPS by the NA50 collaboration using a dimuon spectrometer [47]. The J/ψ mesons are identified by the invariant mass of the measured muon pairs as shown in Figure 3.10.

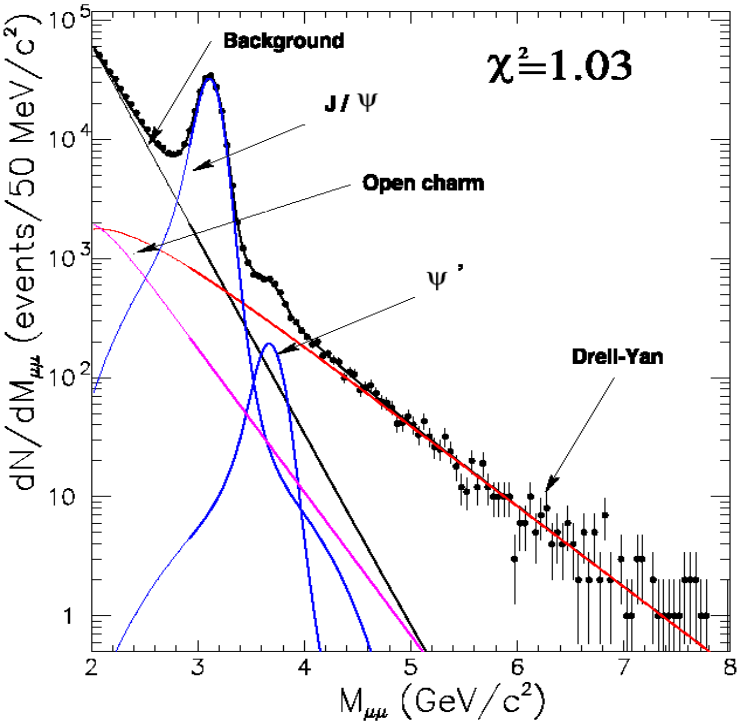

Figure 3.10: Dimuon invariant mass spectrum measured in Pb+Pb collisions at 158 GeV/u by the NA50 collaboration [47].

Figure 3.11 shows the yield of J/ψ mesons normalized to the yield of Drell-Yan pairs as function of the transverse energy as measured in Pb+Pb collisions. This ratio should be constant if charmonium is produced in hard collisions (i.e. in the same way as Drell-Yan pairs) and if there is no absorption of J/ψ mesons. The lines represent calculations that account for J/ψ absorption in hadronic matter. The difference between the calculations and the data above transverse energies of about 80 GeV indicates an anomalous J/ψ suppression that can be interpreted in terms of the formation of a quark-gluon plasma at an early stage of the collision.

As of today there are no measurements of open charm in heavy ion collisions. Since most of the charmed quarks appear in the final state as D or $\overline{D}$ mesons, data on open charm production are crucial for a deeper understanding of charm production in general and for the interpretation of the charmonium data in particular. Moreover, the D-mesons - which are bound states of a heavy charm quark and a light quark, are predicted to be modified in the nuclear medium [48,49]. To the extend that these modifications are partly related to in-medium changes of the light-quark condensate, they offer another interesting option to probe the restoration of chiral symmetry in dense hadronic matter [48].

Open charm has been measured in hadron-hadron collisions (p, K, π on p) and in collisions between hadrons and nuclei (for a review see [50]). The upper panel of Figure 3.12 shows the excitation function for D (and $\overline{D}$) meson production in proton-

nucleon collisions, while in the lower panel the corresponding data for charmonium production are presented (taken from [51]). No data on D meson production exist below a laboratory beam energy of about 250 GeV. On the other hand, J/ψ mesons have been measured in pp collisions in the energy range of the future GSI accelerator.

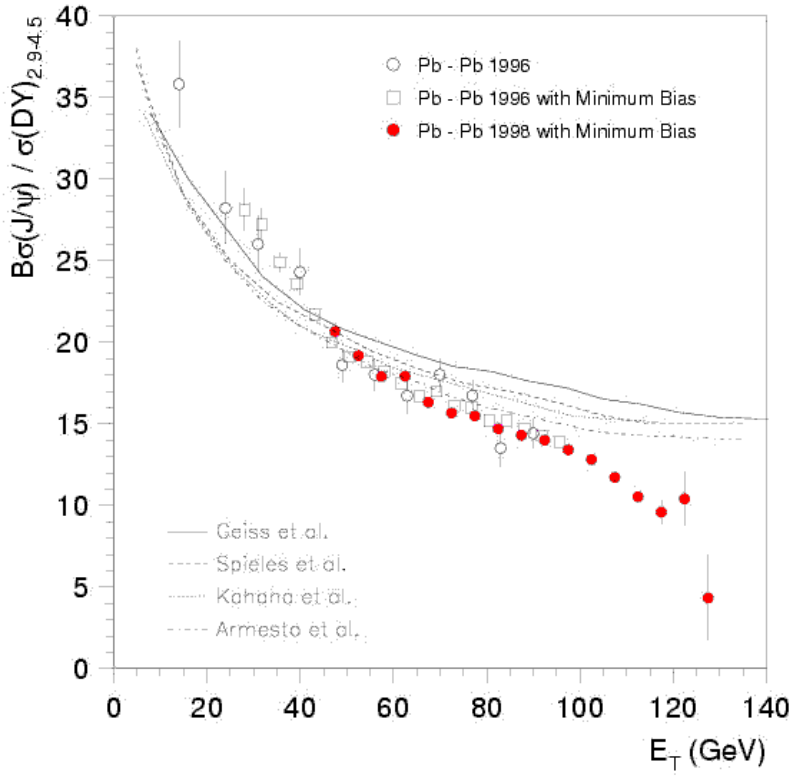

Figure 3.11: Multiplicity of J/ψ mesons normalized to the number of Drell-Yan pairs measured in Pb+Pb collisions as function of transverse energy [47]. The lines represent calculations which take J/ψ suppression in nuclear matter due to hadronic interactions into account. The difference between the calculations and the data above transverse energies of about 80 GeV indicates an anomalous J/ψ suppression as expected if a quark- gluon plasma was formed in the collision.

The dimuon spectrometer at the CERN-SPS will be equipped with an array of silicon pixel detectors in order to look for displaced muon vertices (NA60) [52]. This upgrade project will address the question whether the observed enhancement of the dimuon yield in the intermediate mass region is due to the semi-leptonic decay of open charm. At LHC, the ALICE experiment will be able to measure both open charm and open beauty by looking at displaced vertices of electrons.

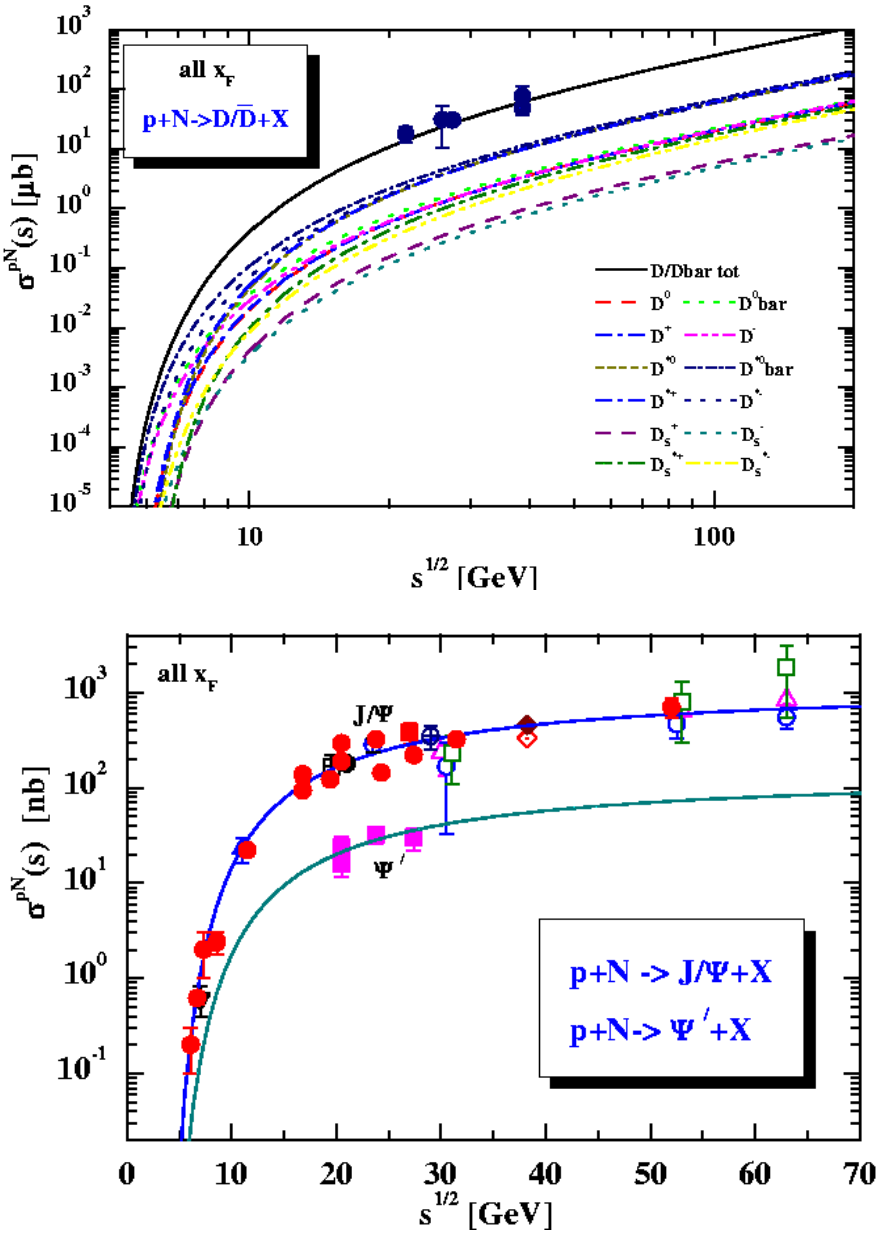

Figure 3.12: D (and $\bar{D}$) (upper panel) and J/ψ and ψ′ (lower panel) production cross sections in proton-nucleon collisions as function of collision energy [50,51].

3.1.3.4 The collective flow of nucleons

The determination of the equation-of-state (EOS) is a major goal of the investigation of nuclear matter at high energy densities. Furthermore, these studies may provide a direct experimental signature of the anticipated phase transitions for deconfinement and chiral symmetry restoration. Calculations indicate a softening of the EOS in the vicinity of the phase transition, with the pressure remaining almost constant with increasing energy density. Pressure gradients are the driving force for the collective

flow of nucleons observed in heavy ion collisions. Therefore, flow measurements provide a unique probe for the pressure developed in the reaction volume and hence may shed light on the nuclear EOS and its change due to a possible phase transition.

An experimental signature for collective flow is the azimuthal anisotropy of the particle distribution. An appropriate measure of the so called directed and elliptic flow are the Fourier coefficients <cosφ> and <cos2φ>, respectively, where φ is the azimuthal baryon emission angle with respect to the reaction plane. While the directed (in-plane) flow depends not only on the pressure but also on the momentum dependence of the interactions, the elliptic flow is found to be quite sensitive to the pressure at maximum compression [53].

Figure 3.13 shows the strength of the elliptic flow (the <cos2φ> coefficient) as function of beam energy measured in semi central Au+Au collisions in three experiments (full symbols) [54]. The remarkable experimental finding is that the sign of <cos2φ> changes at a beam energy of about 4 GeV/u. A negative sign means that the particles are emitted preferentially perpendicular to the reaction plane ("squeeze-out") whereas a positive value of <cos2φ> characterizes the opposite emission pattern, i.e. preferential in-plane emission at midrapidity. The data in Figure 3.13 are compared to results of transport calculations assuming a soft EOS (open circles, dotted line) and a stiff EOS (open squares, solid line) [55].

The data points around 1 and 2 GeV/u seem to be better reproduced by the calculations based on a stiff EOS whereas the data at 4 GeV/u and above are better described by the calculation using a soft EOS. This interpretation of the data suggests a softening of the EOS between beam energies of 2 to 4 A GeV as it is expected for a phase transition. However, one should note that in semi central Au+Au collisions at beam energies of 1 GeV/u the FOPI collaboration has found values of <cos2φ> which favor a soft EOS [56]. This discrepancy may be caused by slight differences in the experimental selection of impact parameter and transverse momentum. A high-precision systematic experimental study of the flow excitation function between 2 and 30 GeV/u is required in order to obtain a conclusive picture of the flow observable.

In future experiments with dedicated setups, rare probes and flow observables will be measured simultaneously. The combination of data on strangeness and charm with those on the collective flow of baryons (as function of beam energy, impact parameter and system size) will provide new and consistent information on possible phase transitions.

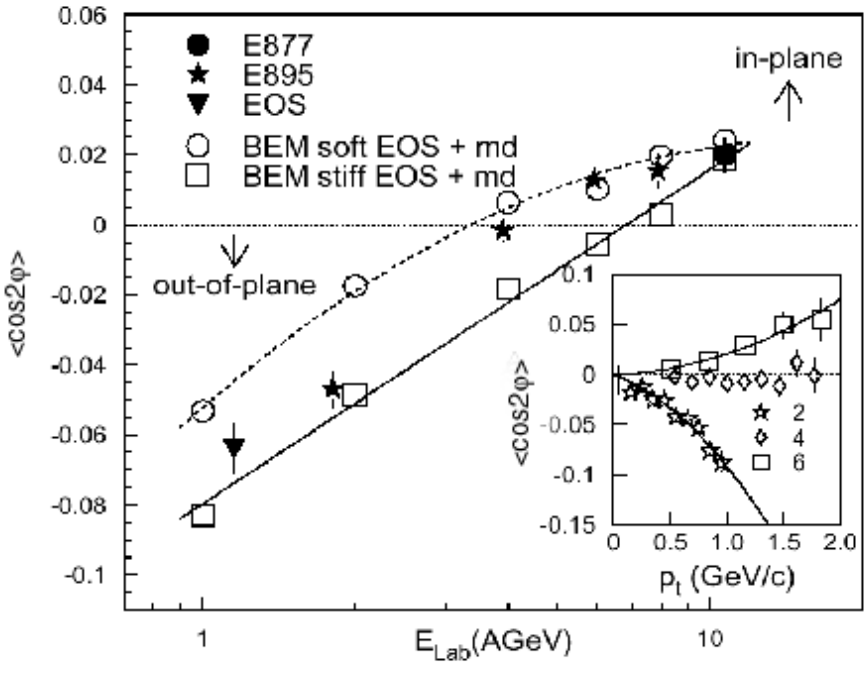

Figure 3.13: Fourier coefficient <cos2φ> (elliptic flow) of protons as function of beam energy measured in semi central Au+Au collisions (full symbols) [54]. Open symbols and lines represent results of transport calculations [55]. The insert shows measured values of <cos2φ> as function of transverse momentum for 2, 4 and 6 GeV/u beam energy.

3.1.4 Future experiments at high baryon densities

3.1.4.1 The goal

The major goal of the proposed experiment is to explore the presently almost unknown region of high baryon densities in the phase diagram of strongly interacting matter. The territory of dense baryonic matter accessible in heavy-ion collisions is located between the line of chemical freeze-out and the hadron/parton phase boundary, as indicated by the hatched area in Figure 3.14. New states of matter beyond the deconfinement and chiral transition at high net baryon densities and moderate temperatures may be within the reach of the experiment. A particular challenge for future heavy-ion experiments is the search for the predicted "critical point" in the phase diagram of strongly interacting matter.

A calculated chemical freeze-out curve and the freeze-out points as derived from particle production data obtained at SIS, AGS, SPS and RHIC are shown in Figure 3.14 [19]. The sum of baryon and antibaryon density at freeze-out (pink line) corresponds to a value of 0.75 ρ_0. The blue curve represents the phase boundary as predicted by a recent QCD lattice calculation for finite baryon chemical potential [14].

According to the calculations, the phase boundary and the freeze-out curve merge at small baryon chemical potentials (μ< 200-300 MeV). The SPS and RHIC data suggest that – at ultra-relativistic beam energies – hadronization and chemical freeze-out occurs almost simultaneously (which implies that the fireball was born in the quark-gluon phase).

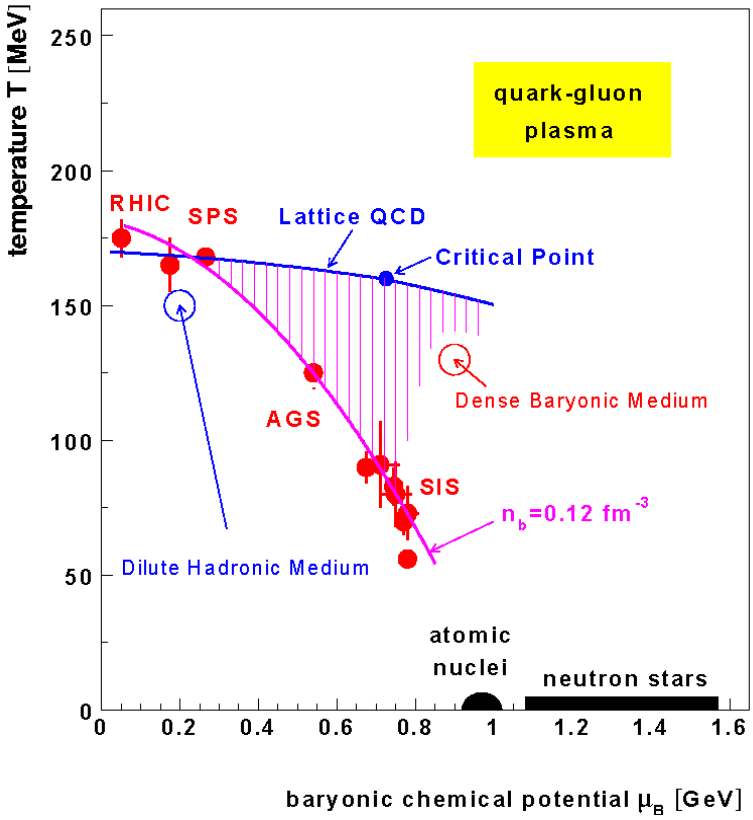

Figure 3.14: The phase diagram of strongly interacting matter. The red symbols represent freeze-out points obtained with a statistical model analysis from particle ratios measured in heavy collisions [16,17,18]. The pink curve refers to a calculation of the chemical freeze-out which occurs at a constant density (baryons + antibaryons) of $\rho_B = 0.75\ \rho_0$ (with $\rho_0 = 0.16$ fm^{-3}). The blue curve represents the phase boundary as obtained with a QCD lattice calculation [14] with a "critical point" (blue dot) at T=160±3.5 MeV and μ = 725±35 MeV ($\rho_B \approx 3\ \rho_0$). In the region of the blue circle the baryon density is ρ_B=0.038 fm^{-3} ≈ 0.24 ρ_0 ("dilute hadronic medium"). The corresponding value for the red circle is ρ_B=1.0 fm^{-3} ≈ 6.2 ρ_0 ("dense baryonic medium"). The hatched area marks the region of equilibrated matter at high baryon densities.

The QCD lattice calculation predicts a critical point at a temperature of 160±4 MeV and a baryon chemical potential of 725±35 MeV (corresponding to a baryon density of about 3 ρ_0). The critical point is located not too far from the AGS freeze-out point and hence could be reached with the future GSI accelerator. The discovery of the critical point or rather its corresponding signal in the finite system would represent a major progress in the exploration of the QCD phase diagram [5].

The experimental challenge is to identify observables which are messengers from the dense fireball rather than from the dilute freeze-out configuration. Some promising diagnostic tools are:

- short lived vector mesons which decay into an electron-positron pair (a "penetrating probe").
- The yields of rare particles containing strangeness and charm – in particular when produced at beam energies close to the corresponding threshold – depends on the conditions inside the early fireball [28]. To a good approximation the created flavor is conserved during the expansion.
- The collective flow of nucleons is driven by the pressure gradients in the early phase of the collision [57]. The "flow" of pions and kaons is caused by shadowing and by in-medium potentials, respectively, and hence reflects the space-time evolution of the collision [30,58,59,60]. A very interesting observable would be the "flow" of probes like light vector mesons (ρ, ω, φ), multistrange hyperons (Ξ, Ω) and charmonium (J/ψ), which has not been measured so far.

With the proposed experimental setup one will be able to measure the observables discussed above in nucleus-nucleus collisions at beam energies between 2 and 30 GeV/u. The energy range from 2 to 7 GeV/u will be covered by the (slightly modified) HADES detector whereas the new "Compressed Baryonic Matter" (CBM) experiment is designed for the energy range from 7 to 40 GeV/u. The envisaged physics program includes:

- search for signatures of chiral symmetry restoration in dense baryonic matter. Probes: Dilepton pairs from light vector mesons, the yield of open charm (D and $\overline{D}$ mesons) and the ratio of open to hidden charm.
- search for signatures of the deconfinement phase transition at large baryonic chemical potentials. Probes: charmonium, strangeness, collective flow.
- search for the critical point. Probes: event-by-event fluctuations of hadronic observables (K/π ratio, $<p_t>$)
- search for exotic states of matter such as condensates of strange particles or color superconductivity. Probes: strange and multistrange particles, K/π ratio

The experimental conditions and observables will be discussed in the following.

3.1.4.2 Experimental conditions

In order to study the high baryon density regime of the QCD phase diagram in the laboratory one would like to produce a long-lived compressed fireball at moderate temperatures. Within a certain range, these properties can be tuned experimentally via the beam energy. With increasing beam energy, the lifetime of the fireball decreases while baryon density and temperature increase. Figure 3.15 shows the baryon density produced in central Au+Au collisions as function of time for different beam energies as calculated with a transport code [61].

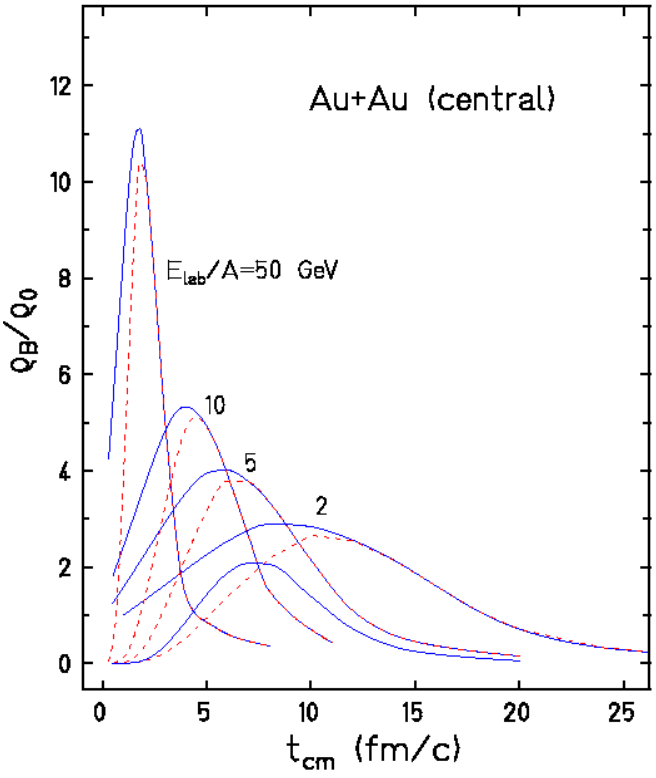

Figure 3.15: Baryon density in units of saturation density in the center-of-mass system calculated for central Au+Au collisions as function of time for different beam energies. The dashed lines represent the densities of nucleons which suffered at least one collision (taken from [61]).

The temperature is reflected in the number of pions produced in the heavy ion collision: the multiplicity of pions varies rapidly with temperature for $T \approx m_\pi$. Figure 3.16 shows the pion multiplicity per participating nucleon measured in nucleus-nucleus (symbols) and nucleon-nucleon collisions (solid line) as function of the available energy in the c.m. system. In heavy ion collisions at AGS energies (e.g. Au+Au collisions at 10.7 GeV/u) the pion to baryon ratio is about 1 while it is about 5 in Pb+Pb collisions at the CERN-SPS energy of 158 GeV/u. Therefore, the experimental observables from heavy ion collisions at 10-30 GeV/u are more sensitive to baryon density than at higher beam energies where temperature effects are dominating.

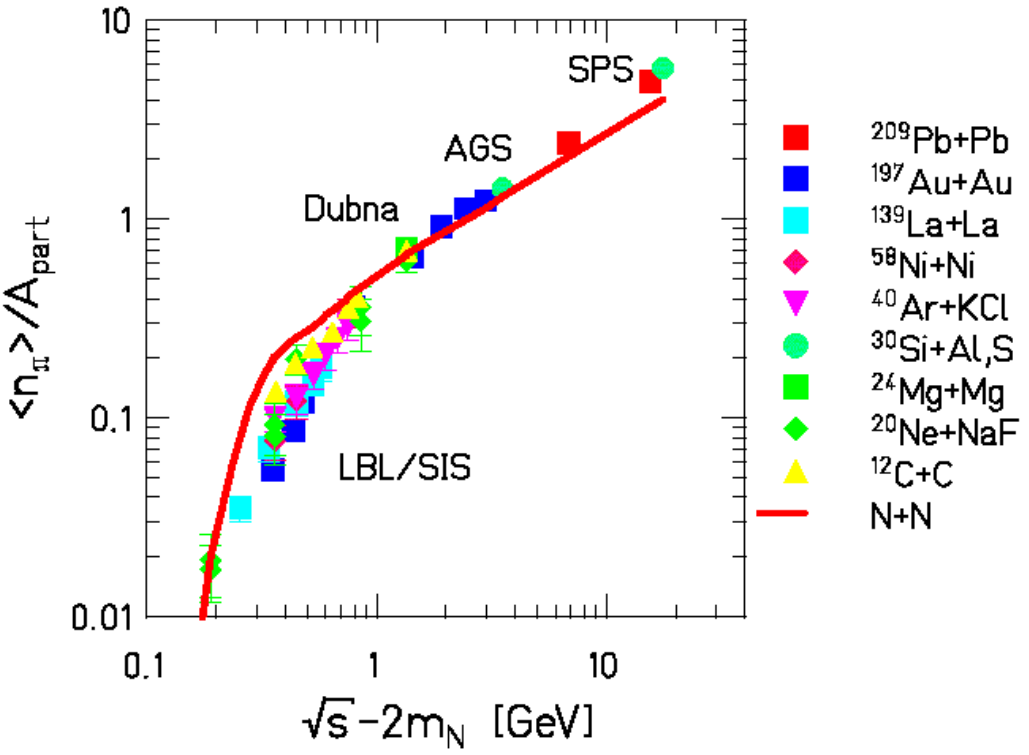

Figure 3.16: Pion multiplicity per participating nucleon for nucleus-nucleus (symbols) and nucleon-nucleon collisions (solid line) as function of available energy in nucleon-nucleon collisions (taken from [62].)

The interest in heavy ion collisions at beam energies around 30 GeV/u was enhanced by recent results of experiments on strangeness production [36,37]. It was observed (see Figure 3.6) that the kaon-to-pion yield ratio (K^+/π^+) measured in central Au+Au (Pb+Pb) collisions exhibits a maximum in the beam energy range between about 20 and 40 GeV/u. This relative maximum of the strangeness content has been attributed to the enhanced production of strange quarks (and antiquarks) in the deconfined phase [38]. On the other hand, a maximum of the ratio of strange to nonstrange particle production is predicted for beam energies around 30 GeV/u by a statistical model calculation without assuming a phase transition [39]. This maximum is unique to heavy ion collisions, and has no equivalent in collisions between elementary particles. The model calculations indicate that the distinct maximum of the ratio of strange to nonstrange particles around 30 GeV/u is dominantly caused by the relative abundance of strange baryons. The results of the calculation is shown in Figure 3.17.

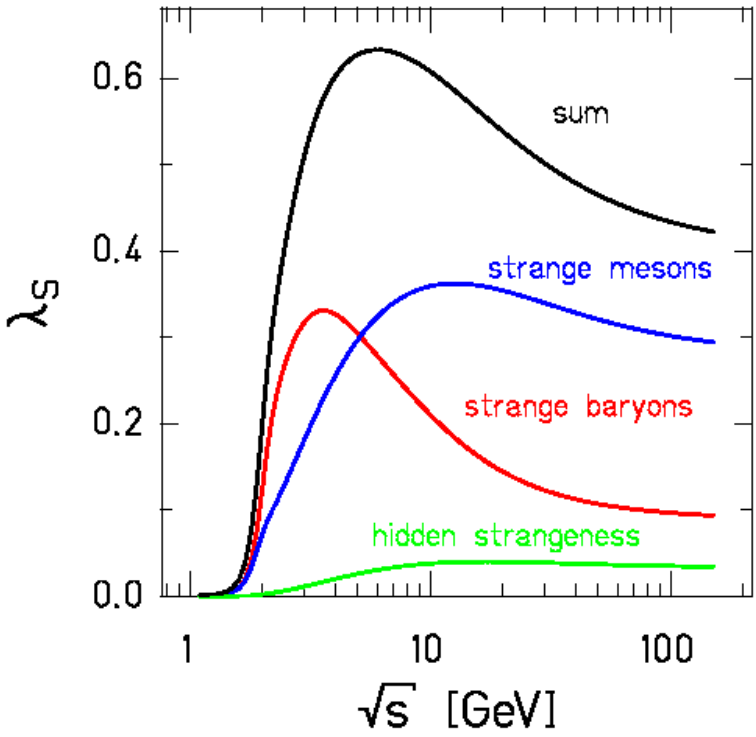

Figure 3.17: Ratio of strange to nonstrange particle multiplicities for strange baryons (red line), strange mesons (blue line) and mesons with hidden strangeness (green line). The sum of all contributions is given by the black line (taken from [39]). The ratio ("Wroblewski factor") is calculated for a chemically equilibrated fireball as function of beam energy. The future GSI accelerator covers the energy range up to $\sqrt{s} \approx 8$ *GeV.*

The data on the K^+/π^+ ratio and their interpretations indicate that "strange" conditions exist inside the fireball as created in heavy ion collisions around 30 GeV/u. Future detailed experimental studies of nucleus-nucleus reactions this energy range - in particular the production of multistrange hyperons (Ξ, $\overline{\Xi}$, Ω, $\overline{\Omega}$) - will help to unravel the role of strangeness at high baryon densities.

3.1.4.3 Looking into the fireball

The measurement of short lived vector mesons via their decay into an electron-positron pair provides the unique possibility to study the properties of hadrons in dense baryonic matter. The lepton pair is a "penetrating probe" because it delivers undistorted information on the conditions inside the dense fireball. The invariant masses of the measured lepton pairs permit the reconstruction of the in-medium spectral function of the ρ-,ω- and φ mesons (if they decay inside the medium).

Such data is expected to shed light on the fundamental question to what extent chiral symmetry is restored at high baryon densities and how this affects hadron masses. In central lead-lead collisions at 158 GeV/u, an enhanced yield of electron-positron pairs

in the low mass region of the invariant mass spectrum has been observed [44]. At present it seems not unlikely that this enhancement is caused by a shift and/or a broadening of the ρ-meson spectral function in matter [6,45].

In Figure 3.18 we show theoretical predictions of the spectral functions of the ρ and the ω-meson in vacuum and in nuclear matter at $\rho = \rho_0$ and $\rho = 1.5\ \rho_0$ [63]. Experiments are presently performed with the HADES detector at GSI in order to study in-medium modifications of vector mesons up to beam energies of 2 GeV/u. This detector will be used also for experiments at the new GSI facility up to beam energies of about 7 GeV/u (after slight modifications). The in-medium properties of vector mesons at the highest baryon densities will be investigated with the proposed CBM detector.

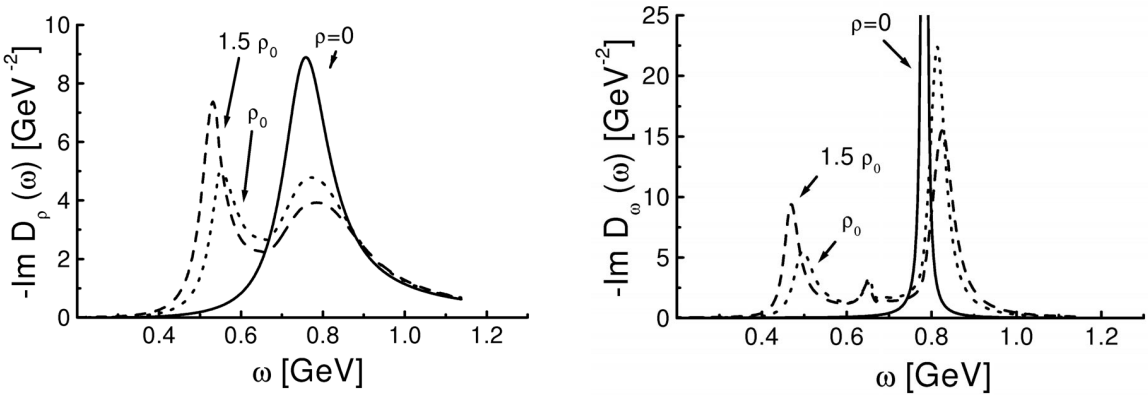

Figure 3.18: The ρ (left) and ω (right) spectral functions in vacuum and in nuclear matter at densities $\rho = \rho_0$ and $\rho = 1.5\ \rho_0$, obtained in a model that describes meson-nucleon scattering data at energies near the vector meson threshold [63]

3.1.4.4 Strangeness and charm production at threshold beam energies

Figure 3.15 suggests that very high baryon densities can be reached during the course of a central Au+Au collision. The maximum density, hovever, is not an observable. The baryon densities determined from particle ratios - which reflect the conditions at hadrochemical freeze-out - are found to be well below saturation density at all beam energies [16,17,18]. The challenge is to find observables which preserve a reminiscence of the dense fireball. In principle, the yield of newly created quark flavors like strangeness and charm is such an observable, in particular for nucleus-nucleus collisions at threshold beam energies. Here, the dominant production processes must involve many particles and thus implies high densities. Then, the yield of strange and charm quarks – once produced in the dense phase –- is to a good approximation conserved throughout the expansion phase.

Experiments on strangeness production in nucleus-nucleus collisions at GSI have demonstrated that effects of the dense nuclear medium can be observed if the beam energy is close to or below the kaon threshold. Figure 3.19 shows the multiplicity of

K^+ and K^- mesons per average number of participating nucleons $M_K/\langle A_{part}\rangle$ as function of the Q value in the nucleon-nucleon (NN) system. The data measured in C+C and Ni+Ni collisions (symbols) [24,29,64] are strongly enhanced with respect to nucleon-nucleon collisions (lines) which are represented by parameterizations of the available proton-proton data averaged over isospin channels [65]. According to transport calculations, this enhancement is predominantly caused by secondary collisions like $\Delta N \rightarrow K^+ Y N$ (with $Y=\Lambda,\Sigma$) and $\Delta N \rightarrow K^+ K^- NN$ with the Δ resonance acting as an energy reservoir. Moreover, processes like $\pi N \rightarrow K^+ Y$ and $\pi \Lambda \rightarrow K^- N$ play an important role. Such multistep processes depend strongly on the baryonic density.

The most interesting result, however, is that the in-medium effects are much larger for K^- than for K^+ mesons: in N+N collisions the K^+ multiplicity exceeds the K^- data by 1–2 orders of magnitude (at similar Q-values) whereas in nucleus-nucleus collisions the kaon and antikaon yields are comparable. Transport calculations describe the K^+ and K^- yields from nucleus-nucleus collisions by an enhanced effective mass of kaons and reduced effective mass of antikaons in dense nuclear matter. These results derived from heavy ion experiments are expected to have consequences also for our understanding of neutron star stability and black hole formation [32].

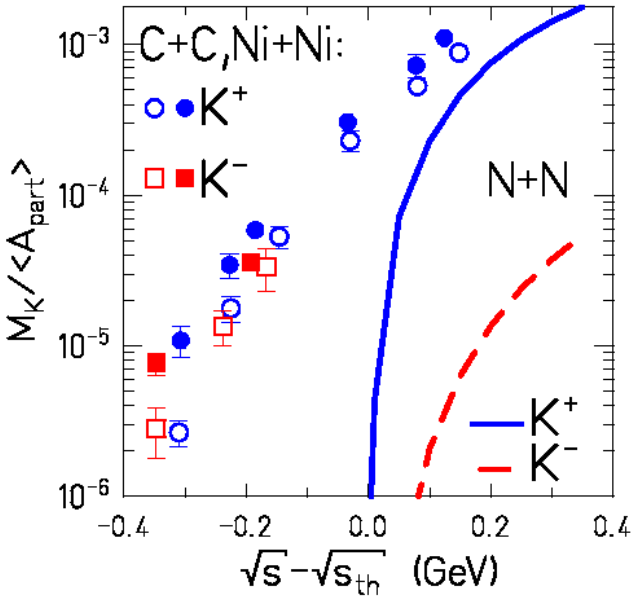

Figure 3.19: K^+ (circles) and K^- (squares) multiplicity per participating nucleon as a function of the Q-value for C+C (open symbols) and Ni+Ni (full symbols) collisions [24,29,64]. The lines correspond to parameterizations of the production cross sections for K^+ (solid) and K^- (dashed) in nucleon-nucleon collisions [65].

In a qualitative picture, the in-medium properties of K mesons are governed by their leading scalar and vector current interactions with nucleons which involve primarily the light quarks of the K mesons. The scalar forces are attractive both for the $u(d)$ and the $\bar{u}(\bar{d})$ quarks whereas the vector current coupling is repulsive for quarks and attractive for antiquarks. Hence, the K^- $(\bar{u}\,s)$-nucleon interaction is attractive

whereas the $K^+(u\bar{s})$-nucleon interaction is weakly repulsive. These interactions contribute to the effective masses of K-mesons in nuclear matter.

The threshold energies for strangeness production in elementary collisions like $NN \rightarrow K^+\Lambda N$ and $NN \rightarrow K^+K^-NN$ are 1.6 and 2.5 GeV, respectively. Central collisions of two gold nuclei at those energies produce baryonic densities of up to 3 times saturation density. Hence, kaon and antikaon production is well suited to probe nuclear matter as it exists in the noncentral region of neutron stars. In order to explore experimentally a system comparable to the inner core of a neutron star, however, more extreme conditions have to be created in the laboratory. According to transport calculations, baryonic densities in the relevant range are reached in central Au+Au collisions at beam energies around 20 GeV/u [66]. The appropriate probe for baryonic matter properties in this energy regime is charm production. This channel opens at beam energies around 12 GeV (in proton-proton collisions) and hence offers the possibility to study in-medium effects at very high baryon densities. The excitation function of strangeness and charm production in central Au+Au collisions is illustrated in Figure 3.20 which shows the results of a transport calculation [51].

The properties of the D-meson are expected to be modified in dense baryonic matter in the same way as those of the K mesons. The $D^+(c\bar{d})$ meson corresponds to the $K^-(s\bar{u})$ and the $D^-(\bar{c}d)$ to the $K^+(\bar{s}u)$. Hence, the D meson masses are predicted to split in a similar way as the K meson masses do [48,49]. In QCD sum rule calculations one finds at nuclear matter density a splitting between the D^- and D^+ mesons of roughly 50 MeV [48] and an overall shift of the $D\bar{D}$ threshold by up to 100 MeV [67]. Due to the steep D production excitation function at beam energies close to threshold (see Figure 3.20) the effective mass of D mesons will translate into a substantial modification of the D yield. Therefore, the D^+/D^- ratio is a promising observable which probes the (chiral) dynamics of a single quark attached, at high baryon densities. We stress at this point that the $D\bar{D}$ and $K\bar{K}$ mass splittings occur only in matter with non-zero net baryon density. Hence, the physics described above is best studied at intermediate beam energies where high net baryon densities are reached.

In order to be able to fully exploit the potential of charm physics at high baryon density, the future GSI accelerator should provide gold beams with energies well above the charm production threshold. This would allow to establish the signal - in particular for open charm which has not yet been seen in a heavy ion collision. The charm experiments with heavy ions will be complemented by corresponding measurements with beams of protons and antiprotons on nuclear targets (see the chapter on experiments with antiprotons). The experimental program at the future GSI facility will provide a comprehensive set of information on the role of charm in hadronic matter under various conditions – from the density of nuclei to that encountered in neutron stars.

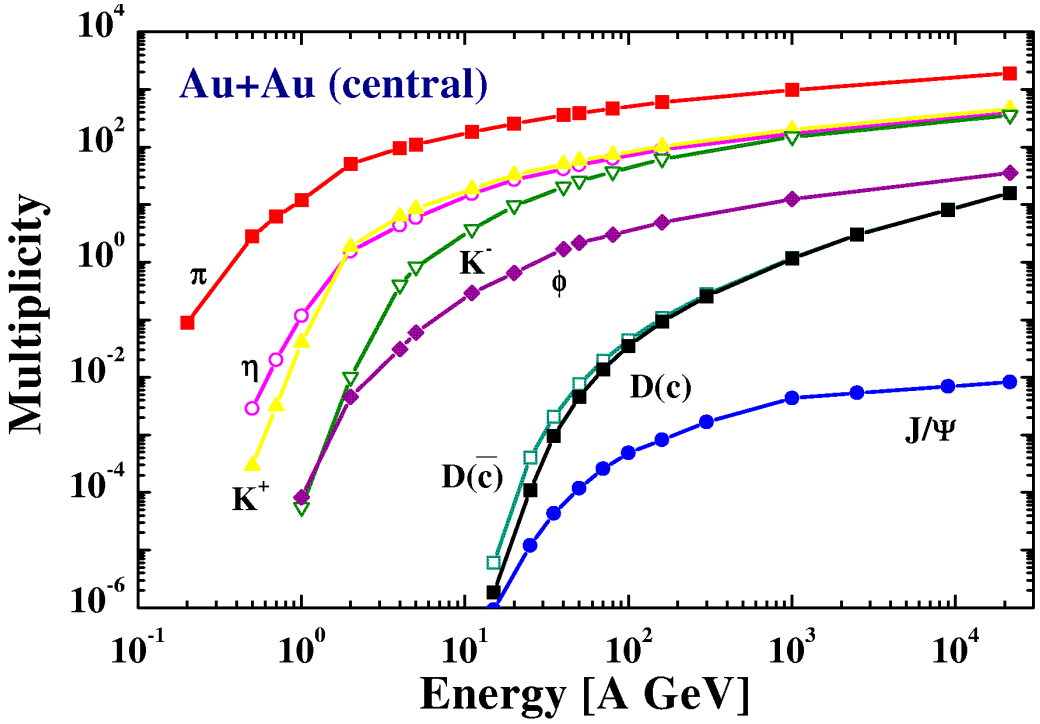

Figure 3.20: The average number of mesons produced per central Au+Au collision (multiplicity) as function of the incident beam energy. The calculation was performed with the HSD transport code. No in-medium mass modification was taken into account (taken from [51]).

3.1.4.5 Charm and more: the demand for completeness

The experiment on charmonium production in Pb+Pb collisions at CERN-SPS energies [47] has probably provided the most direct evidence for the discovery of a "new state of matter" (see CERN Press Release, February 10, 2000). The observed strong decrease of the relative charmonium yield with increasing collision centrality has been interpreted as a signature for anomalous J/ψ suppression in the deconfined phase. The question whether other mechanisms such as the interaction of charmonia with comovers or transverse energy fluctuations [68] might cause the observed behavior is a subject of current debate.

Further progress in the understanding of charmonium production and propagation in heavy ion collisions requires new experimental information such as excitation functions, phase space distributions and, in particular, data on open charm production. Most of the created charm quarks are confined in D or $\overline{\mathrm{D}}$ mesons together with a light quark. Therefore, the observation of open charm in heavy ion collisions is of crucial importance for the interpretation of the charmonium data.

At the future GSI facility, charmonium production and propagation will be studied at very high baryon densities. The dense medium affects the properties and the yield of J/ψ mesons in various ways. The effective charmonium mass is expected to decrease

only slightly in ordinary nuclear matter [48], primarily due to the very moderate in-medium reduction of the gluon condensate. At high baryon densities, this effect should be more significant. In particular, at beam energies close to threshold – where the J/ψ production excitation function is very steep (see Figure 3.20) – a decrease of the J/ψ mass would result in an increase of the J/ψ yield. Moreover, a modification of the D meson mass in dense matter would affect the relative abundance of open and hidden charm. As mentioned above, the J/ψ yield is reduced by two main mechanisms: First by absorption of J/ψ mesons in the nuclear medium and second by disintegration of J/ψ mesons if the baryons "melt" at very high densities and hadronic matter is converted into a plasma of quarks and gluons.

In order to disentangle these effects one has to study the production of both J/ψ and D mesons under different experimental conditions, i.e. one has to vary the beam energy, the size of the collision system and the impact parameter. A new quality of data and new observables are required, i.e. exclusive measurements of rare particles. Future experiments should be able to identify charmonium, light vector mesons and multistrange hyperons and to measure their momenta and emission patterns. For example, the (momentum dependent) elliptic flow of J/ψ mesons would permit the determination of the nuclear absorption in the spectator fragments. This should be feasible for moderate spectator velocities, i.e. at intermediate beam energies.

The proposed CBM experiment will be designed to measure simultaneously charmonium, D mesons, multistrange hyperons and light vector mesons (including protons, pions and kaons). This will permit the study of various probes under identical experimental conditions and to minimize systematic uncertainties. Data on particle multiplicities, phase-space distributions and particle-particle correlations will provide a complete picture of the space-time evolution of the reaction zone. The conditions inside the fireball – such as density and temperature – vary with beam energy, size of the collision system and impact parameter. Observables such as vector mesons, strange and charmed particles will be measured as a function of those parameters. Of particular interest are correlations between rare probes and hadronic observables or even between different rare probes. For example, it would be extremely interesting to measure simultaneously J/ψ mesons and multistrange hyperons and to find conditions where both the yields of strangeness and charmonium change significantly. Such measurements can be performed successfully only at a dedicated facility where a universal detector can run for a (sufficiently) long period of time.

The J/ψ yield measured in nucleus-nucleus collisions will be compared to results from proton-nucleus collisions. At normal nuclear matter density and low temperatures the in-medium modifications of J/ψ mesons are predicted to be small and no quark-gluon plasma will occur. Therefore, the proton-nucleus data will serve as a reference system (including J/ψ absorption in nuclear matter). The experimental study of J/ψ production in antiproton-nucleus collisions will provide additional information (see chapter on the physics with antiprotons).

3.1.4.6 Towards maximum baryon densities

A crucial issue for the experimental study of high density phenomena is the baryon density of the fireball and its lifetime. Estimates based on relativistic transport calculations (e.g. ART [66]) of a central Au+Au collision at 20 GeV/u indicate that densities exceeding five times that of ordinary nuclear matter can last for a time span of 5 fm/c (see Figure 3.21). Both density and reaction time are enhanced considerably in collisions of deformed nuclei which are aligned along their deformation axis (tip-on-tip). This is shown in Figure 3.21 for a central tip-on-tip U+U collision at 20 GeV/u. The effect is somewhat reduced for semicentral collisions (lower panel of Figure 3.21). Tip-on-tip events might be selected experimentally by large values of transverse energy and perfect azimuthal symmetry.

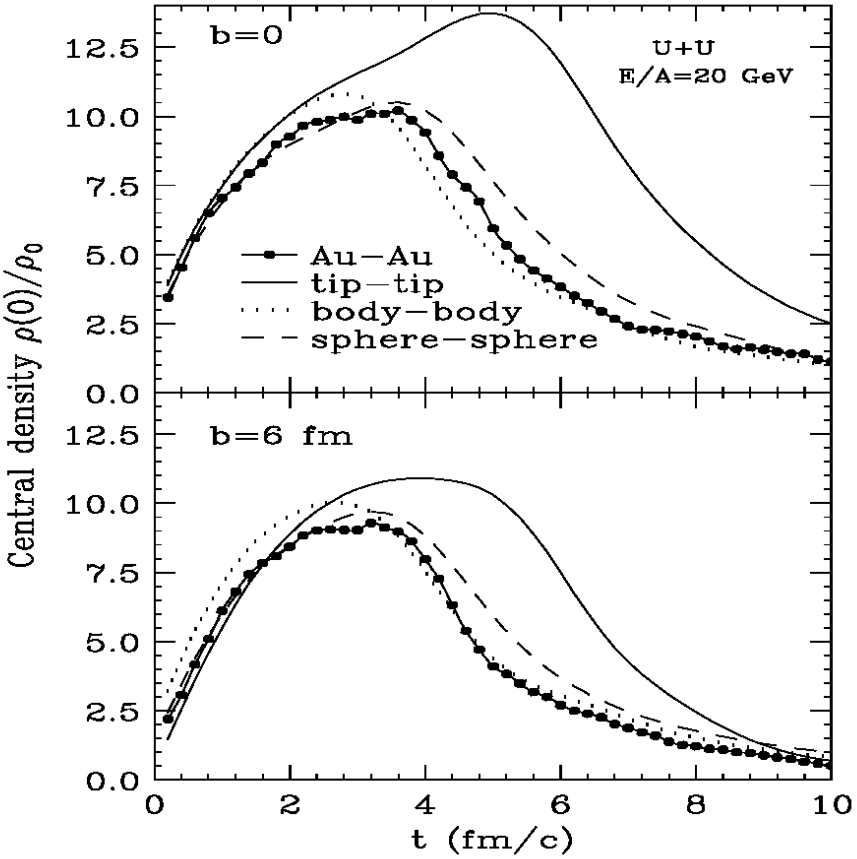

Figure 3.21: Upper panel: central density as function of time for central Au+Au collisions (dotted line) and tip-on-tip U+U collisions (solid line) at 20 GeV/u as calculated with the ART transport code [66]. Lower panel: same for semi-central collisions (b=6 fm).

3.1.4.7 Speculative aspects

The existence of novel states of strongly interacting matter in the high-pressure environment of neutron star cores has been explored theoretically [1]. Among these states are deconfined quark matter, stable strange quark matter, kaon condensates and hyperon-rich matter. In most of the scenarios strangeness plays an important role.

The stability of neutron stars is due to the balance between two forces, the gravitational attraction and the pressure of the strongly interacting particles. However, there are speculations that even microscopic objects consisting of strange quark matter could be stable. These exotic objects, referred to as strangelets, are expected to have a large mass (e.g. 1000 times the mass of a nucleon) and small electric charge [69,70,71]. They could have been produced in the big bang, may still exist as cosmic rays, and are also considered as candidates for the dark matter in the universe [70]. However, the search for stable multistrange objects in the cosmic ray spectrum has not met with success.

Furthermore, it has been proposed that similar objects, stable or metastable, may be produced in the hot and dense fireball of a heavy ion collision [72]. Also here no experimental evidence was found in the searches carried out at BNL-AGS and CERN-SPS. However, the experiments performed so far were not sensitive to short lived candidates, which could be the objective of future studies. A possible signature is a high multiplicity of strange particles which are emitted from a common secondary vertex. The proposed experiment is very well suited for the identification of such events.

3.1.5 A second generation fixed target experiment

The proposed experiment is a universal instrument which will be able to measure both leptons and hadrons, and to identify efficiently rare probes in a large background of charged particles. In order to achieve this goal the experiment will combine state-of-the-art detector components which in part are under development for future experiments at the Large Hadron Collider at CERN.

The layout and the arrangement of the detector components is optimized for the study of collisions between very heavy nuclei at beam energies between 10 and 30 GeV/u. The experiment is focused on the measurement of charmonium, D mesons and multi-strange hyperons (which have not been observed up to now in nucleus-nucleus collisions at beam energies below 158 GeV/u) and of light vector mesons (which have not been measured in heavy ion collisions between 2 and 40 GeV/u). In this chapter we estimate count rates and present the general scheme of the experimental setup. A more detailed description of the detector components and the results of performance simulations are presented in the technical part of the proposal.

3.1.5.1 Particle multiplicities and count rates

No experimental data on particle multiplicities are available for nucleus-nucleus collisions at the highest SIS200 energies. Therefore, we have taken predictions from various calculations: the relativistic transport codes RQMD [73] and HSD [28] and a thermal model [74]. The results of the different approaches are listed in Table 3.1. The transport models simulate central Au+Au collisions at 25 GeV/u whereas the thermal model results are obtained for a temperature of T=140 MeV and a baryon chemical potential of μ_B = 480 MeV.

The NA49 collaboration has studied Pb+Pb collisions at a beam energy of 40 GeV/u. For the most central 5% of the cross section the following multiplicities were measured: 272±15 π^+, 313±15 π^-, 57±3 K^+ and 17±1 K^- [37]. When interpolating these data and the corresponding data measured in central Au+Au collisions at 10.7 GeV/u (E802 at AGS [36]) one obtains values for Au+Au collisions at 25 GeV/u as listed in Table 1. The interpolated values of the measured pion multiplicities are significantly lower than the results of the transport codes whereas the K^+ multiplicities agree within 10%.

Table 3.1: Multiplicities for central Au+Au collisions at 25 GeV/u from simulations using RQMD and HSD. Experimental values are obtained by interpolation of data measured by NA49 and E802. The results of a thermal model with T = 140 MeV and μ_B = 480 MeV are calculated relative to the number of π- which is assumed to be 250.

particle	mass (MeV)	RQMD	HSD 3% central	NA49 (40 GeV/u) E802 (10.7 GeV/u)	thermal
π^0	135	394			
π^-	140	398		234±14	250
π^+	140	369	298	197±12	226
η	550	34	39		17
K^+	494	44	36	39.6±2	46
K^-	494	13	14.5	10.2±0.5	13
ρ^0	770				16
φ	1020		1.0		2.3
Λ	1116	30	37 (incl. Σ^0)		40
Σ^-	1197	11	9.2		10.5
Ξ^-	1321	1.25	0.9		2.4
Ω^-	1672				0.15
D^-	1865		$5 \cdot 10^{-4}$		
J/ψ	3097		$1.5 \cdot 10^{-5}$		$3.7 \cdot 10^{-6}$

In the following we estimate the count rates for charm production in central Au+Au collisions at a beam energy of 25 GeV/u. The estimation is based on the multiplicities as predicted by the HSD transport code. The very low charm yields at 25 GeV/u have to be compensated by a high beam intensity in order to obtain reasonable counting statistics. Other probes like hyperons have much larger production cross sections and a lower experimental background.

J/ψ production

Table 3.2 presents the count rate estimate for J/ψ production in Au+Au collision at 25 GeV/u in comparison to the rates for the CERN-SPS beam energy. Due to the higher beam intensity, the larger spill fraction and the larger experimental acceptance at SIS200 the rate of recorded J/ψ mesons may differ only by a factor of about 2 as compared to NA50 at CERN-SPS. The limitation of the maximum beam intensity due to the performance of the detectors, the trigger and the data acquisition is discussed in the technical part of the proposal. The technical part includes also simulations of the experimental acceptances and of the combinatorial background from pion and eta Dalitz decays and from misidentified pions.

Table 3.2: Expected J/ψ count rates for Au+Au at 25 GeV/u. The corresponding values for the CERN experiment NA50 [46] are shown for comparison.

	25GeV/u Au+Au	158 GeV/u Pb+Pb
J/ψ multiplicity (central collisions)	$1.5 \cdot 10^{-5}$	$1 \cdot 10^{-3}$
beam intensity	$5 \cdot 10^{8}$/s	$2 \cdot 10^{7}$/s
interactions	$1 \cdot 10^{7}$/s (2%)	$2 \cdot 10^{6}$/s (5%)
central collisions	$1 \cdot 10^{6}$/s	$1 \cdot 10^{5}$/s
J/ψ rate	15/s	100/s
6% J/ψ →e+e- (μ+μ-)	0.9/s	6/s
spill fraction	0.8	0.25
acceptance	0.20	0.15
J/ψ measured	0.14/s = $8 \cdot 10^{4}$/week	0.22/s = $1.3 \cdot 10^{5}$/week

Open charm

D meson production in hadron-nucleus reactions has been measured up to now only with high-energy pion, kaon or proton beams. No charmed mesons have been observed so far in nucleus-nucleus collisions. The experimental difficulty is to identify a displaced vertex with a resolution of better than 100 μm in a high track density environment. Even more challenging is to trigger on the decay topology of D mesons.

Nowadays this may become possible with radiation-hard Silicon pixel and strip detectors as for example developed for the ALICE experiment at LHC. Vertex position resolutions in the order of 50 μm are achievable with these tracking devices. We propose to trigger on the electron from the semileptonic D-decay and to identify the second D meson of the produced pair by its hadronic decay topology in a Silicon pixel detector array. The most prominent hadronic decay channels with only charged particles in the final state are $D^+ \rightarrow K^- \pi^+\pi^+$ (or $D^- \rightarrow K^+ \pi^-\pi^-$) (9±0.6%) and $D^0 \rightarrow K^- \pi^+$. (3.9±0.09%). The vertex of the D decay is displaced from the main interaction vertex according to the lifetimes of $c\tau$ = 317 μm and $c\tau$ = 124 μm for $D^{\pm}$ and D^0, respectively. We expect a D-meson rate of about 150 events per week. Details of the count rate estimate are presented in the technical part.

3.1.5.2 Layout of the experiment

The experimental task is to identify both hadrons and leptons and to detect rare probes in a heavy ion environment. The apparatus has to measure multiplicities and phase-space distributions of hyperons, light vector mesons, charmonium and open charm (including the identification of protons, pions and kaons) with a large acceptance. This requires a universal setup with unique properties. We propose to build a second generation fixed target experiment which combines detector components as developed for future experiments at the CERN-LHC. The challenge is to identify those rare probes in Au+Au (or U+U) collisions at beam intensities of up to 10^9 per second and with a charged particle multiplicity of about 1000 per central event. Therefore, the experiment has to fulfill the following requirements:

- fast and radiation hard detectors
- large acceptance
- electron and hadron identification
- high-resolution secondary vertex determination
- selective trigger

The experimental setup consists of the following detector components:

- Dipole magnet for bending the particle trajectories and δ-ray deflection
- Radiation hard Silicon pixel/strip detectors for tracking and vertex determination
- Transition radiation detector (TRD) for electron identification
- Ring imaging Cherenkov detector (RICH) for electron (and hadron) identification
- Resistive plate counters (RPC) for time of flight measurement
- Diamond pixel detector for TOF start signal

The Silicon tracking detectors are placed inside a strong magnetic field. This technology is now sufficiently advanced, in particular because of the experimental efforts of the various LHC experiments, so that low mass and high mass lepton pairs can be measured simultaneously without the need of a field-free region near the target.

The dimensions of the detectors are chosen such that for central nucleus-nucleus collisions at 25 GeV/u and a magnetic dipole field of B = 1 T about 70% of the emitted charged particles are accepted (for details see the technical part). Figure 3.22 displays a sketch of the proposed setup including the HADES spectrometer [75] which will be used to measure dileptons and hadrons at beam energies up to about 7 GeV/u.

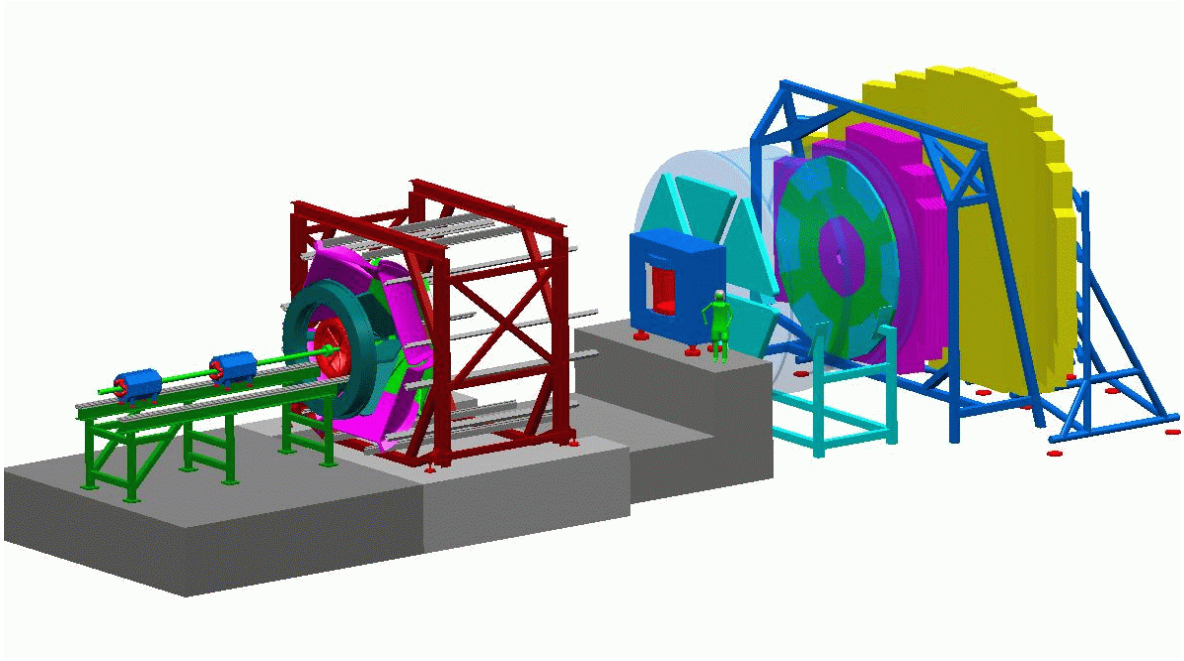

Figure 3.22: Sketch of the experimental setup. The beam enters from the left hand side. The first device is the HADES detector which will be used (after some modification) to measure dilepton pairs and hadrons in the beam energy range up to about 7 GeV/u. The HADES target is placed at the entrance of the spectrometer. The Compressed Baryonic Matter (CBM) detector will measure dilepton pairs and hadrons up to beam energies of about 40 GeV/u. The setup consists of a dipole magnet (blue), a RICH Detector (turquoise), a TRD detector (pink) and a RPC TOF wall (yellow). The Silicon tracker is inside the magnetic field of the dipole. The CBM target is at the entrance of the magnet. The beam line optical system has to provide a focused beam either for HADES or for CBM experiments.

3.2 Instrumentation and detectors

3.2.1 Experimental concept of a dilepton and hadron spectrometer

The experimental setup consists of the following components:

Dipole magnet:
The magnetic field bends the particles according to their momentum (and charge) and prevents most of the abundantly produced δ-electrons from hitting the detectors.

Radiation hard Silicon pixel/strip detectors:
A set of Silicon pixel (and strip) detectors close to the target allows to determine the particle trajectory (and hence the momentum) with high accuracy. This Silicon tracker will measure the decay topology of hyperons and hence their invariant mass. A vertex resolution of better than 50 μm is required for the identification of charmed mesons.

Transition radiation detector (TRD):
The TRD allows to identify high energy electrons ($\gamma > 2000$) and hence the measurement of charmonium via the invariant mass of the electron positron pair.

Ring imaging Cherenkov detector (RICH):
The RICH detector provides identification of electrons with $\gamma > 40$ corresponding to the momentum range of dielectrons from vector-meson decays. When using a radiator gas with higher refractive index the RICH signals can be used to identify high energy pions and kaons.

Resistive plate counters (RPC) for TOF measurements:
The large area RPC provides the stop signal for the time-of-flight measurement which allows the identification of low momentum particles. A TOF distance of 10 m results in a time difference of 400 ps for pions and kaons of 3 GeV/c momentum.

Diamond pixel detector for TOF start signal:
A Diamond pixel detector provides the start signal for the TOF measurement. It will count directly the beam particles up to intensities of 10^9 ions/s.

Some parameters of the detector systems are listed in Table 3.3. A sketch of the proposed setup is shown in Figure 3.23.

Table 3.3: Parameters of the detector systems

Detector	# of planes	Size [cm^2]	granularity	# of channels
Silicon tracker	7	19 - 7822		$4.5 \cdot 10^6$
UV detector (RICH)	6 sectors	triangle, L ≈ 2.6 m	1.3 x 1.4 cm^2	82800
TRD	2 x 6 layers	30m^2	1 – 25 cm^2	2 x 6 x 35000
RPC (TOF)	2	120 m^2	4 – 100 cm^2	2 x 35000

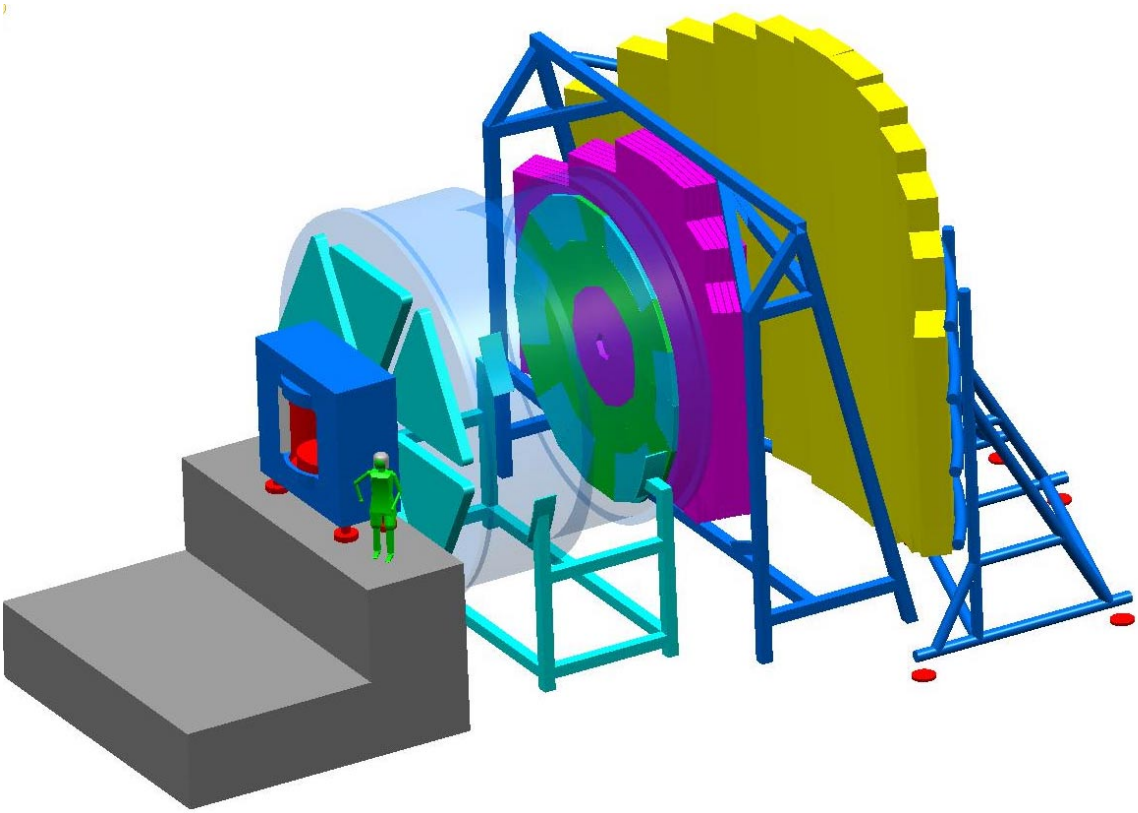

Figure 3.23: The experimental setup consisting of the dipole magnet (blue), the RICH UV detectors (turquoise), the RICH radiator (transparent blue) and the RICH mirror (blue/green), the TRD detector (pink) and the RPC TOF wall (yellow). The Silicon tracker is inside the magnetic field. The target is at the entrance of the magnet (from the left side).

3.2.2 The detector components

3.2.2.1 The Superconducting Dipole Magnet

The requested bending power of the magnet should be in the region of 1-2 Tm. In order to restrict the size of the tracking detectors located inside the field, the field region should be confined within 1 m along the beam axis. The requested acceptance of 25° results in a gap width of 1 m. A simple estimate of the coil requirements assuming a perfect yoke to close the field lines results in 2 coils with 800000A*turns each to provide a field of 2T. This requires a superconducting coil. In the following feasibility study a coil design similar to the Hades magnet was chosen.

- Indirect cooling with liquid He at 4.5 K (Hades 4.7K).
- Cable with 4.5 x 7 mm^2 cross section (without isolation) and 270 turns.
- Current: 3000 A (Hades: 3465 A).
- Current density = 95 A (including Al/Cu Matrix, excluding isolation).
- Coil shape: Double pancake 2x 70.5 x 65 mm^2.
- Maximum field (inner edge of the coil): 3 T (Hades: 3.8 T).
- Differential radial force on the coil: 4000 N/cm (Hades: 6000 N/cm).
- Total net force on the coil: 66000 N (Hades 48000 N).
- Coil case including liquid Nitrogen shield and coil support: 120x200 mm^2 (Hades: case thickness 80 mm).
- Ramp-up / down time (minimise eddy currents): 1/2 hour (Hades: 1hour).

The coil shape consists of two half-circles (radius=0.5 m) connected by a 12 cm long straight section. This geometry optimizes the field configuration (see below). A cross section through the coil and the surrounding iron (field clamp and yoke) is shown in the left part of Figure 3.24. A vertical cut through the magnet is shown in the right part of Figure 3.24.

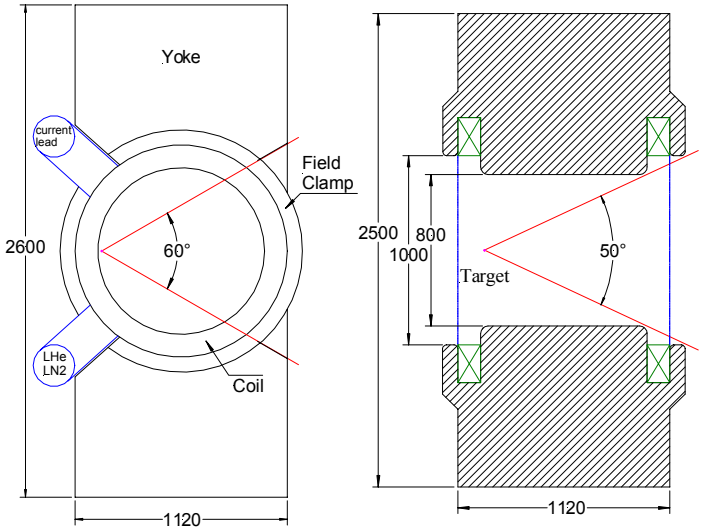

Figure 3.24: Left: Horizontal cross section through the magnet (coil, field clamp and yoke). A horizontal acceptance of ± 30° and the Cryo infrastructure is indicated. Right: Vertical cross sections through the magnet (numbers in mm)

The field of the coil was calculated using Biot-Savarts formula. The induced field in the iron was modelled by infinite long coils starting at the pole tip and the field clamp surface, respectively, using corresponding shapes. This crude approach cannot account properly for details of saturation effects and needs to be replaced by TOSCA calculations. The calculated vertical field at different distances from the mid-plane of the gap are shown in Figure 3.25. The low field strength at the edges of the iron pole tip is due to the decreasing field induced by the coil. The iron is saturated in this region. The integrated horizontal bending power along straight trajectories (transverse kick) is presented in Figure 3.26.

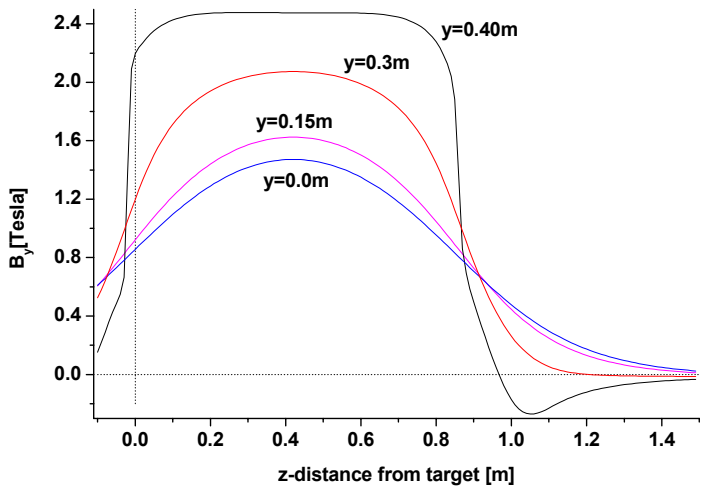

Figure 3.25: Estimated vertical field at various distances y from the mid-plane of the magnet (y=0).

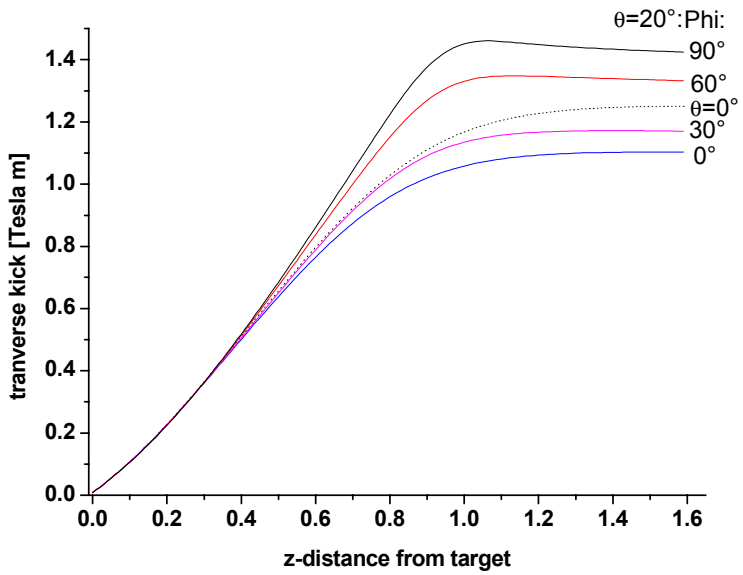

Figure 3.26: Estimated transverse kick (integrated horizontal deflection strength) for θ=0° (dashed line) and θ=20° and various azimuthal angles ϕ.

3.2.2.2 The Silicon Tracking System

The task of the tracking system is to perform a measurement of the charged particle trajectories in the magnetic field of the dipole up to emission angles of 25^0. The track information should allow to determine the momentum with an accuracy of better than 1% and secondary decay vertices with a resolution of about 50 µm. The anticipated reaction rates will be up to 10^7/s with a multiplicity of up to 1000 charged particles per event. Therefore, the tracking system has to fulfill the following requirements:

- high granularity
- fast read out to avoid pile up and for 3rd trigger operation
- radiation hardness
- operation in high δ-ray background

Charged particle multiplicities and hit densities

The following estimates of particle multiplicities are based on central Au+Au collisions at an energy of 25 GeV/u as simulated with the URQMD transport code [73]. For such a reaction the calculations predict an average number of charged particles of approximately 1000. However, an interpolation of measured data (see Table 3.1) results in a value of about 700. Therefore, the estimation should be considered as an upper limit.

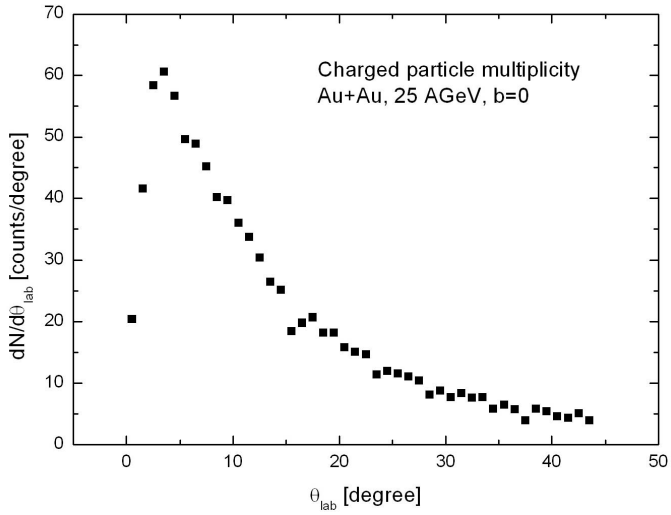

Figure 3.27: Charged particle multiplicity for central Au+Au collisions at 25 GeV/u as function of the laboratory polar angle. Result of a simulation using the URQMD transport code [73].

Figure 3.27 shows the laboratory polar angular distribution of charged particles produced in central Au+Au collisions at 25 GeV/u according to the URQMD calculation. Due to the strong kinematical focusing, the particle flux is very high at small opening angles downstream the target. On a plane perpendicular to the beam axis 5 cm downstream of the target the flux exceeds 100 cm^{-2} at a radial distance smaller than 0.7 cm. The respective distributions as function of the distance from the target are depicted in Figure 3.28. To cope with the tasks listed above, the tracking detectors are grouped in 7 planes. The hits in five planes at 5, 10, 20, 30 and 40 cm distance from the target define a track with high position and angular resolution in order to optimize the vertex resolution. Two further planes at 80 and 100 cm distance allow the determination of the curvature caused by the magnetic field.

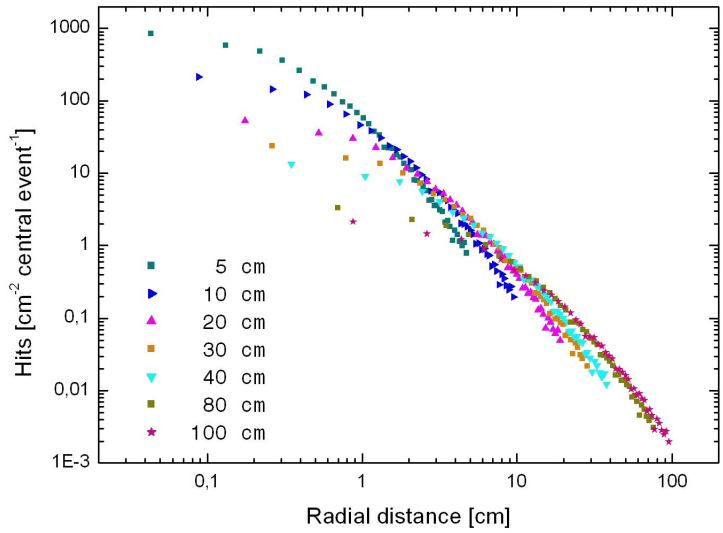

Figure 3.28: Local hit density on the various tracking planes as a function of the radial distance from the beam axis for Au+Au at 25 GeV/u. The distances indicated refer to the distances of the tracking planes from the target.

Silicon Tracking Detectors

The high track densities reached and the required tracking precision clearly call for a highly granular detector system with sub-millimeter pixel dimensions. The requirements for such a detectors system are close to those for the so-called Inner Tracking Systems (ITS) of next generation (LHC, TESLA) collider experiments [76-80]. The common choice for the IT systems at LHC are radiation hard silicon detectors partly in combination with highly integrated radiation hard read-out structures which are ball bonded to the detector chips. Respective R&D programs are carried out in large collaborations since many years. Naturally, the layout of the tracking system will rely on this technology.

For regions with highest hit densities (up to 100 cm^{-2} for central Au+Au collisions at 25 GeV/u) silicon pixel detectors (SPD) are foreseen [81]. These systems make use of highly integrated CMOS technology allowing to place a complete readout chain for a single pixel as small as 50 x 300 μm^2 [82]. This results in an occupancy of about 1.5 %. Several read-out chips containing typically 5000 such structures are surface packed onto an appropriate silicon detector. Such a truly 2-dimensional device delivers binary information: the signal is amplified shaped and discriminated to switch the bit high in case the signal in a pixel is above the threshold. Operated in this way, the sensor works with very short intrinsic dead time. It is defined by the shaping time of the preamplifier and the discriminator response time (25 ns in case of the ATLAS PIRATE chip, a number dictated by the bunch crossing time of the LHC).

In regions where the local hit density drops below 1 cm^{-2}, double-sided strip detectors are the best choice. VLSI chips sitting at one end of the sensor and being bonded to the bond-pads of the strips read out these detectors. Double-sided technology with stereo stripes on the front and back-side allows two-dimensional co-ordinate information on a single wafer.

Granularity

To determine the granularity required in such a high rate experiment, both the average local track density and the intrinsic dead time (e.g. shaping time etc.) of the detector has to be taken into account. We anticipate the use of fast binary read-out for the pixels and gated track and hold chips for the strip detectors. Due to the small capacities of the pixel sensors, shaping times as short as 25 ns can be used. Hence, fired cells can be uniquely attributed to the collision triggered. In case of the strip detectors, the longer peaking times of typically 500 ns lead to an event pile-up at interaction rates higher than 10^6 particles per second.

In addition, heavy beams produce δ-electrons while traversing the target. To shield the tracking detectors against the bulk of δ-electrons, already the first tracking station is positioned in the magnetic field. Hence the abundant low-energy electrons are deflected away from the detectors. The remaining yield of energetic δ-electrons was determined using a GEANT calculation and is compared to the particle rates in Figure 3.29. The δ-electron densities are a factor of at least 5 below the hadrons.

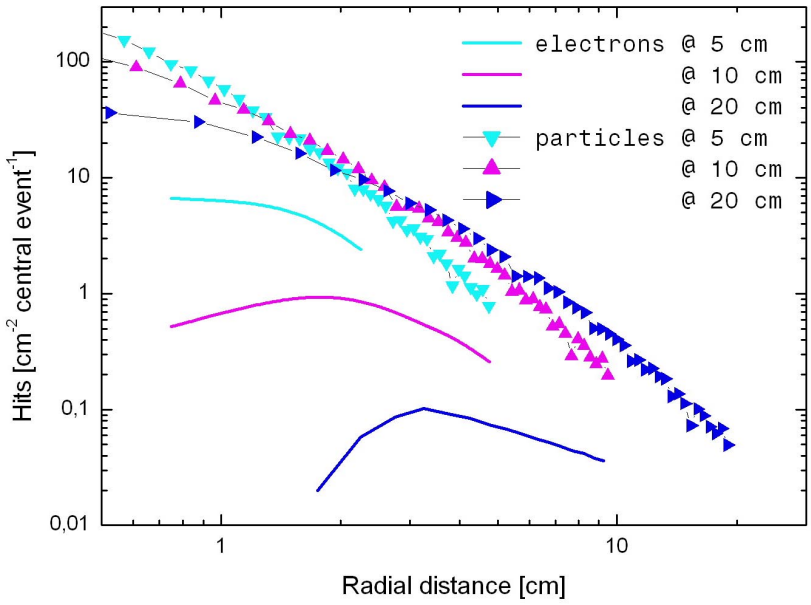

Figure 3.29: δ-electron flux compared to the charged particle flux in central Au on Au collisions. Only the first three tracking stations are considered.

Configuration

The high granularity required for small laboratory polar angles can only be achieved by silicon pixel detectors (SPD). To keep the number of channels under control, pixel sensors are solely placed in regions where strip detectors will saturate. As a consequence, only the first plane is entirely composed of SPD. Tracking planes 2-5 consist of both types of detectors whereas for plane 6 and 7 silicon strips are sufficient. Table 3.4 summarizes the basic design numbers for the silicon tracker. The tracking planes are placed perpendicular to the beam axis. The SPD have an inner hole of circular shape with radius R_{min}. At a radius R_{max} the pixel detectors end and silicon strip detectors are used to cover the active area. The outer border of the silicon strip detectors is of elliptical shape to accommodate the asymmetry caused by the deflection in the magnetic field. The total area of 1.5 m^2 is covered by 4.5×10^6 cells.

Table 3.4: Dimensions of the different tracking planes at distances D from the target. R_{min} and R_{max} refer to the inner and outer dimension of the respective detector (mean of smaller and larger radius in case of elliptic outer shapes).

Plane	D [cm]	Type	R_{min} [cm]	R_{max} [cm]	Area [cm^2]	# of elem. structures	# of cells
1	5	Pixel	0.55	2.5	19	36	177,576
2	10	Pixel	0.55	5	78	120	391,920
3	20	Pixel	1.3	7.5	172	256	842,628
		Strip	7.5	10	137		13,738
4	30	Pixel	1.3	7.5	172	256	842,628
		Strip	7,5	15	530		52,988
5	40	Pixel	1.3	7.5	172	256	842,628
		Strip	7.5	20	1079		107,938
6	80	Strip	3	40	4996		499,574
7	100	Strip	3	50	7822		782,174
Total area = 1.5 m^2					Total # of cells = 4.5 10^6		

The current concept for the pixel detectors is based on a hexagonal structure with a base length of 6 mm. The pixel layout of this elementary structure will be designed such that it can be read-out by one read-out chip. Based on this design, the different active areas can be covered with a limited number of sensor geometries.

Position resolution

For pixel detectors with binary pad response the achievable position resolution is given by the pitch divided by √12. If the energy loss signal is read out and the detectors have an optimized pad response, the resolution can be as good as 1 % of the pitch. Resolutions measured with prototypes of ITS detectors are listed in Table 3.5.

Table 3.5: Performance parameters for Inner Tracking Systems.

Experiment	Type	δx(r,φ) [μm]	δx(z) [μm]
Delphi	Strip	21	36
SLD	CCD	9	14
ATLAS	Pixel	12	60
	Strip	17	500
ALICE	Pixel	12	70
	Drift	38	28
	Strip	20	830

Expected integral dose

The estimation of the integral dose is based on the assumption of 10^{14} interactions between gold nuclei. Scaling the hit densities of Figure 3.28 by a factor 0.25 to accommodate for impact parameter average and taking into account an average hardness factor to account for the particle energy and species [83], the hit density can be transformed to integral normalized particle flux Φ_{eq} by multiplying with 6 10^{12}. Thus the flux reaches values of $\Phi_{eq} = 10^{15}cm^{-2}$ on the very inner part of the first tracking plane. Such values are also assumed for LHC experiments and the RD48 (ROSE)[3] collaboration concludes that oxygen enriched material is able to fulfill these requirements [84].

Material budget

The detectors have a thickness of 250 μm (pixel) and 300 μm (strip) (ALICE type detectors). However, the effective thickness increases because detectors need to be partially stacked if a full coverage of the acceptance window is desired. Moreover, additional material is introduced by read-out needed to transport the information to the data acquisition. Here the degree of parallelism needed to speed up the read-out sufficiently is the essential parameter. As a guideline, a value of 0.5-0.7% X_0 has to be assumed for a single tracking plane.

Cooling

A rough estimate of power dissipation can be made assuming 100 μW/channel for the pixel sensors. Thus the dissipated power will come close to 0.5 kW for the complete tracking system, which necessarily calls for effective cooling.

3.2.2.3 The Transition Radiation Detector

Transition Radiation Detectors (TRDs) are being used in high energy experiments to improve the identification of electrons with respect to pions for momenta above 1 GeV/c (see ref. [85] for a review on TRDs). The TRD will allow to study various aspects of dielectron physics, among them the production of quarkonium states (J/ψ and ψ'), as well as the production of open charm.

Detector principle and characteristics

The TRD is composed of a radiator and a photon detector, the latter being in our case a Drift Chamber (DC) with a 3 cm drift zone and an amplification region of about 6 mm. To cope with the large charged particle multiplicities expected in central Au+Au collisions and to provide the necessary position resolution for track reconstruction, the

[3] R&D on Silicon for future Experiments

readout of the DC is done on a pad plane with pads either rectangular or of chevron type [86].

A cross-section of a segment of one module of the TRD is shown in Figure 3.30 along with a schematic illustration of the signals detected by the DC from a pion and an electron (with Lorentz factor $\gamma > 1000$). The signal from TR photons produced in the radiator is superimposed on the signal from energy loss of electrons, as their angle with respect to the electron trajectory is very small (of the order of $1/\gamma$).The field lines in the DC, depicted in Figure 3.30, are calculated with GARFIELD [87] for the dimensions mentioned above. The radiator is not to scale.

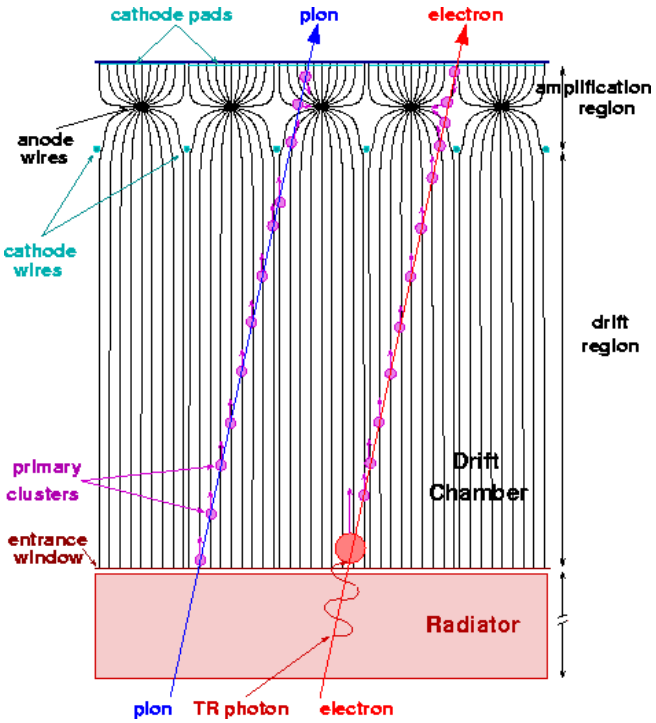

Figure 3.30: The geometry of one TRD module. The geometric proportions and the field lines in the Drift Chamber (DC) are accurate. The radiator is not to scale. Schematic signals produced by a pion and an electron are shown.

The detection gas of the DC must be a Xe-based mixture for an efficient absorption of the transition radiation (TR) photons with energies between 4 and 30 keV.

Six TRD layers will be placed about 5 meters downstream of the target. Each layer covers an area of about 30 m^2. With pad sizes between 1 cm^2 and 25 cm^2 the total number of channels per layer amounts to about 35000, depending on the final geometrical configuration. The layout is based on an occupancy of smaller than 5% for central Au+Au collisions at 25 GeV/u (see Table 3.6).

Table 3.6: Emission angle, charged particle density, detector surface, pad size and number of pads per TRD layer. The numbers refer to a central Au+Au collision at 25 GeV/u and an occupancy below 5%.

θ_{lab}	N/cm^2	area [m^2]	pad size [cm^2]	No. of pads
$1^o - 5^o$	$5 \cdot 10^{-2} - 2 \cdot 10^{-2}$	1.2	1	12000
$5^o - 10^o$	$2 \cdot 10^{-2} - 6 \cdot 10^{-3}$	2.6	3	8700
$10^o - 15^o$	$6 \cdot 10^{-3} - 2 \cdot 10^{-3}$	4.8	8	6000
$15^o - 25^o$	$2 \cdot 10^{-3} - 5 \cdot 10^{-4}$	21.5	25	8600

Whether this type of TRD can stand the high load (in particular for the most forward polar angles where the multiplicities are high) imposed by the required event rates (see section Data Aquisition and Trigger) remains to be tested. However, another possibility exists, the so-called ``fine-grain TRD'' which was adopted for the ATLAS experiment at LHC [88]. It was demonstrated that such a design can achieve count rates as high as 7 MHz per straw (which is a readout cell). Such a Transition Radiation Tracker (TRT) could be an option for a limited portion (most forward angles) of the present setup. However, with such a design it would be difficult to achieve the required granularity.

Results of prototype tests

The results reported here were obtained in tests with prototypes for the ALICE TRD project [89]. For a detailed report see ref. [90]. The measurements have been carried out at beam momenta between 0.6 and 2.0 GeV/c at the pion beam facility of GSI. The electron content of the beam varies as function of momentum, being of the order of 2-3 % for 1 GeV/c. The chevron width is 10~mm and the chevron step is tailored to the anode wire pitch of 5 mm. Each pad is connected to a preamplifier (PA) whose output is fed into a Flash-ADC (FADC), sampling with a frequency of about 20 MHz the drift time of up to 2μs. The DC gas mixture was Xe, CH_4 (10 %) and the chamber has been operated at a gas gain of about 8000. Current- and charge-sensitive PAs were specially designed and built for these tests. For the results presented in the following the charge-sensitive PA was used. It has a gain of 2 mV/fC and a noise of about 1800 electrons rms. We use an 8-bit non-linear FADC system with 100 MHz sampling, integrated in the GSI-standard, VME-based data acquisition system, MBS [91].

The distributions of the integrated energy deposit are shown in Figure 3.31 for pions and electrons with momenta of 1 GeV/c. The pure Landau distribution of pions is skewed towards higher values in the case of electrons by the contribution of the TR. The measured distributions of energy deposit (Figure 3.31) and of the time position of the largest cluster have been employed as probability distributions in simulations aimed at determining the pion rejection factor for the proposed configuration of the TRD with 6 layers.

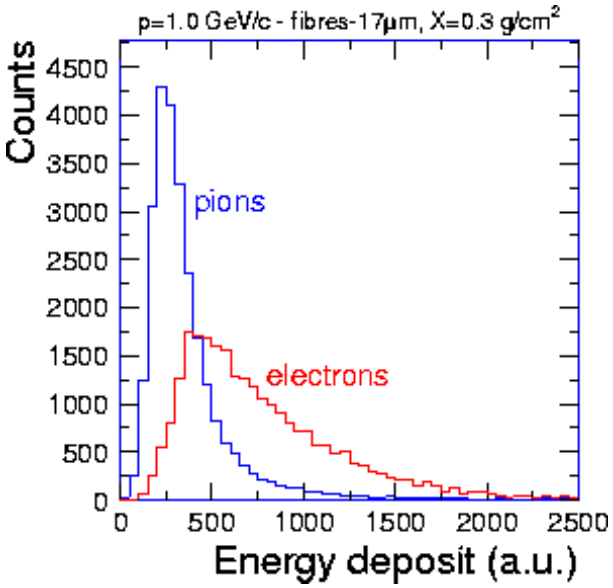

Figure 3.31: Integrated energy deposit for pions and electrons for a momentum of 1.0 GeV/c. A radiator with 17μm fibre with the thickness X=0.3 g/cm² has been used.

To extract the pion rejection factor we have studied three different methods: i) truncated mean of integrated energy deposit, TMQ; ii) likelihood on integrated energy deposit, L-Q [92]; iii) bidimensional likelihood on energy deposit and position of the largest cluster found in the drift region of the DC, L-QX [93]. We assume that the six layers have identical performance as represented by the measured distributions. Both the truncated mean (the truncation is done by excluding the highest value of the integral energy deposit among the layers) and the likelihood (see i.e. [92,94] for details) distributions were constructed over the six (independent) layers for the same number of simulated pion and electron events. Cuts of certain electron efficiency were involved at the end on these distributions and the pion efficiency is derived within these cuts. We note that another method, "cluster counting" is widely used, in particular for "fine grain" TRDs like the one used in ATLAS [88].

Various radiators were tested: regular foils of polypropylene (PP), mats of irregular PP fibres with various fiber diameters (between 15 and 33 μm) and foams of different material type: PP, polyethylene (PE) and Rohacell (RC). As an example, in Figure 3.32 we present the pion efficiency (the rejection factor is the inverse of this efficiency) as function of electron efficiency for a sample of radiators mentioned above. This is done for a momentum of 1 GeV/c, for an equivalent thickness of X=0.6 g/cm² (the foil radiator was however thinner, X=0.5 g/cm²). In general, the fibres show a good TR performance, comparable to that of foils, while the foams are sizeably worse. Similar results concerning the comparison of different radiator materials have been obtained in other experiments [95]. The radiator composed of fibres with 17 μm diameter is a good compromise between TR performance and simple construction. The results presented below are for this case.

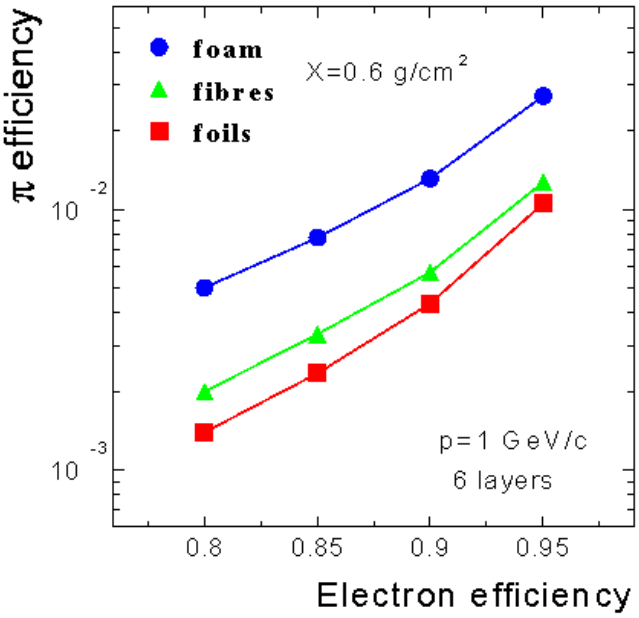

Figure 3.32: Pion efficiency as function of electron efficiency at the momentum of 1 GeV/c for a 6 layer TRD, using a likelihood on the energy deposit (LQ). Compared are radiators composed of foam (Rohacell, ρ=0.11 g/cm³), fibres (polypropylene, ρ=0.09 g/cm³) and foils (220 polypropylene foils of 25 μm thickness, spaced by 250 μm).

In Figure 3.33 we present the pion efficiency as function of electron efficiency (90 % electron efficiency is the commonly used value) in case of radiators with 17 μm fibre diameter, for a momentum of 1 GeV/c. The three methods introduced above are compared. The truncated mean method, although it delivers sizeable worse identification, has the advantage of being very easy to use. It is advantageous especially for an on-line identification. The bidimensional likelihood delivers the best rejection factor and will be studied further in order to optimize the final detector design. As emphasized earlier [93], the use of FADC to process the signals in a TRD can bring up to a factor of 2 in pion rejection power. In general, the three methods employed here give results in good agreement with earlier studies [93]. By doubling the equivalent thickness of the radiator from X=0.3 g/cm² (left panel of Figure 3.33) to X=0.6 g/cm² (right panel) one gains a factor of about 2 in pion rejection power. On the other hand, a more relaxed cut on electron efficiency of 80 % provides a three times higher pion rejection factor.

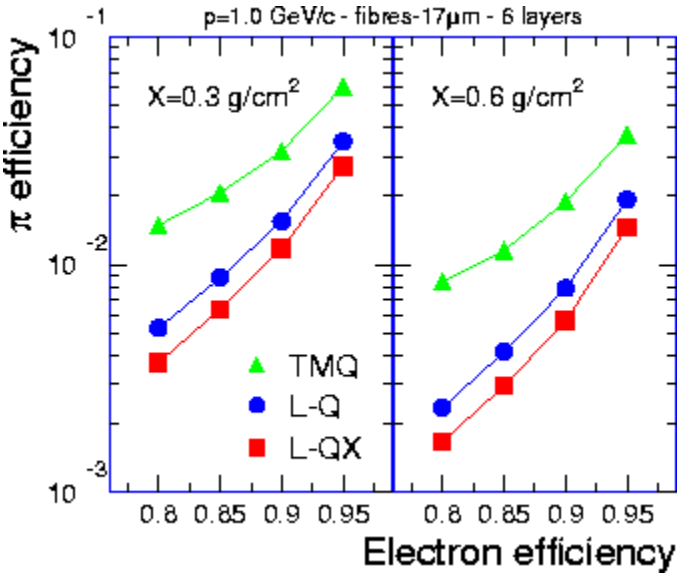

Figure 3.33: The pion efficiency as function of electron efficiency determined with truncated mean on energy deposit (TMQ), likelihood on total energy deposit (L-Q) bidimensional likelihood on charge deposit and DC depth (L-QX).

The pion efficiency at 90% electron efficiency as function of momentum is shown in Figure 3.34. The steep decrease of pion efficiency at momenta around 1~GeV/c is due to the onset of TR production [92,94]. Towards our highest momentum value, 2 GeV/c, the pion efficiency reaches a saturation, determined by the TR yield saturation and by the pion relativistic rise. Due to these effects the pion rejection is expected to get slightly worse for momenta above 3 GeV/c [92]. As one can see in Figure 3.34, at momenta of 2 GeV/c the pion rejection factor of 300 to 500 achieved during these tests is a good starting value. However, one has to bear in mind that a significant degradation of TRD performance has been registered when going from prototype tests to real detectors [85]. This can be the effect of detector loads in a multiparticle environment. On the other hand, impressive pion rejection factors of 1000 and above have been achieved in full size TRDs in the NOMAD [94] and HERMES [95] experiments.

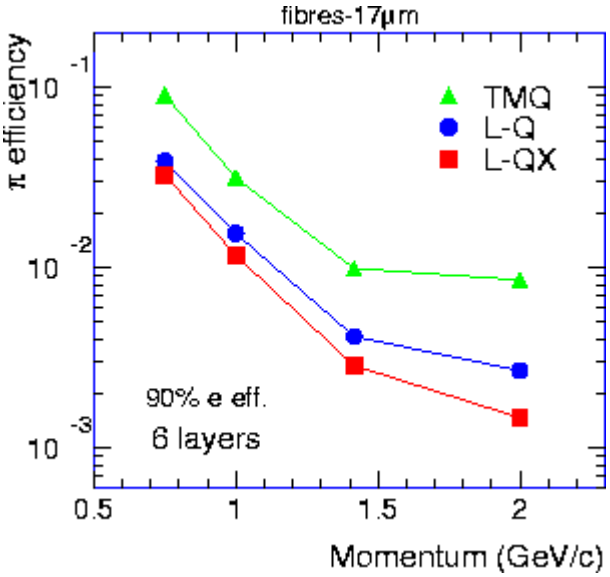

Figure 3.34: Pion efficiency as function of momentum for a radiator with 17μm fibres. The three methods used are discussed in the text.

For momenta below 1 GeV/c (where the TR yield is very low), the electron-pion separation can be improved by employing the truncated mean of the energy loss (on the total number of FADC samples) over the full 6 layers of the detector. Using this method, rejection factors of few hundreds have been obtained with PHENIX prototypes for momenta below 1 GeV/c [96].

3.2.2.4 The Ring Imaging Cherenkov Detector

A ring imaging Cherenkov detector will serve two purposes:

1. Lepton identification up to the highest momenta (approx. 10 GeV/c).
2. Separation of fast pions and kaons. Simultaneous lepton identification in a restricted momentum range (< 5 GeV/c).

The basic design features are:

- Radiator-gas = counter gas
- No window between UV detector and radiator
- Mirror: float glass 1.8 mm thick, 36 segments
- UV-photon detector: solid CsI photocathode

Without a window between the UV detector and the radiator, the choice of radiator gases is limited to CH_4 and C_4H_{10}. However, both gases can be mixed with He and N_2, respectively in order to increase the radiation threshold and decrease multiple scattering. Table 3.7 lists the basic properties of radiator gases and possible admixtures.

Table 3.7: Properties of various radiator/counter gases. The photon yield is based on efficiencies obtained with the current Hades RICH [97,98,99].

radiator gas	$\lambda_{threshold}$ [nm]	n-1 [10^{-4}]	$\gamma_{threshold}$	Θ_c [degree]	detected photons (l = 4m)	radiation length [m]
CH_4	145	4.44	33.6	1.7	54	650
He	<145	0.35	119.5			5300
N_2	<145	2.98	41			304
C_4H_{10}	170	19.0	16.2	3.5	100	169
50% C_4H_{10} + 50% N_2	170	11.0	21.3	2.7	58	218
20% He + 80% CH_4	145	3.62	37.2	1.54	44	787
40% He + 60% CH_4	145	2.804	42.24	1.36	34	999

The arrangement of the mirror and the UV detectors downstream of a dipole magnet is shown in Figure 3.35. In order to shift the focal plane radially away from the beam axis, the mirror is divided into 6 sectors each tilted by 11.5°. Emission of Cherenkov light is indicated schematically by blue lines. A region of up to 0.5 m behind the dipole should be excluded from the radiator volume since the particle trajectories are still bend in the fringe field of the magnet. This results in an effective radiator length between 4.0 and 4.4 m. Figure 3.36 shows the arrangement of the 6 UV detectors shielded from direct charged particle hits by the iron of the magnet. Since the field inside the iron nearly reaches saturation (2T) it can 'trap' quite efficiently low energetic reaction products produced inside the iron like knock-on electrons and hadronic showers. Since the mirror sectors are tilted, sufficient space between the active areas of the UV detectors is available to account for frames and support structure without affecting the acceptance. The horizontal deflection in the dipole field most likely requires a larger horizontal extension of the system than shown in Figure 3.36 in order to get the requested acceptance (25° emission cone).

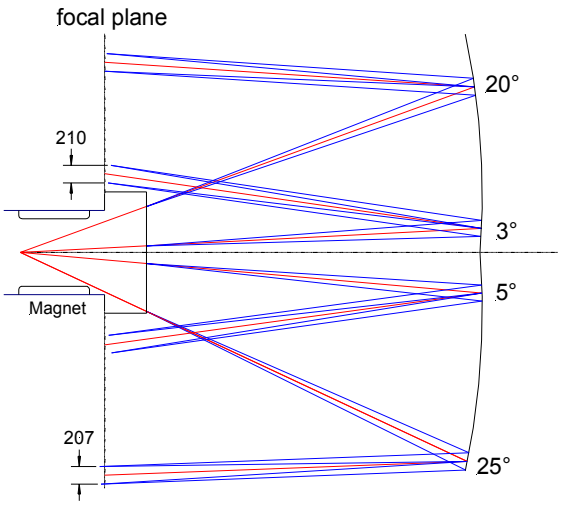

Figure 3.35: Vertical cut through a RICH consisting of 6 mirror segments (R=9m) tilted by 11.5° away from the z axis (horizontal dashed line). A dipole with a gap of 1m / 0.8m is indicated on the left.

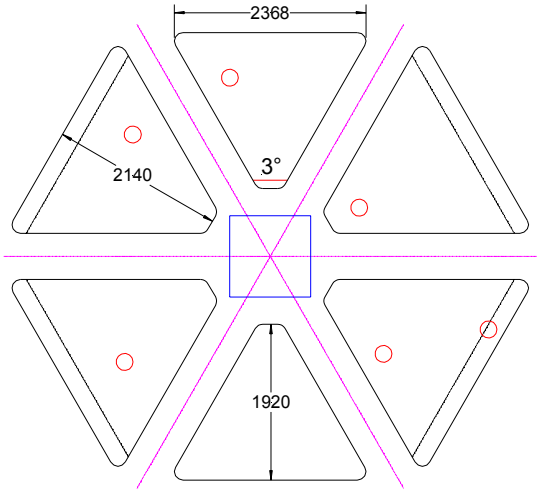

Figure 3.36: Geometry of the UV detectors (black full lines). The dipole gap is indicated as a blue square in the centre.

Mirror

Float glass is manufactured in large quantities at low cost. It does not require any polishing and can be bent applying a mass production technique. Due to the large bending radius (R=9 m) the inhomogeneity in the radius of curvature observed for prototypes of the Hades RICH (R = 0.85 m) should be reduced to values comparable to other distortions of the ring shape due to multiple scattering (0.05°x1GeV/c^2

/momentum for CH_4) or the dispersion of the index of refraction. Figure 3.37 shows a possible segmentation of one sector of the mirror in 6 elements.

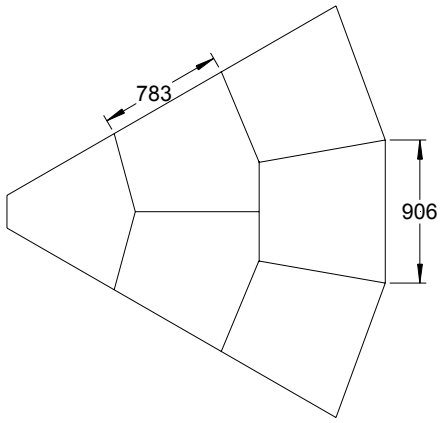

Figure 3.37: One sector of the mirror consisting of 6 segments

Particle Identification

Identification of rare dielectron decays requires a high threshold to discriminate against high energy pions. Table 3.8 lists the pion detection threshold for different radiator gases. Since the ring radius at threshold is zero, an effective threshold is specified requiring a ring radius R of 90% of the asymptotic value R_0.

Table 3.8: Detection threshold for pions (middle column) and discrimination threshold to distinguish leptons from pions (right column) for various radiator gases.

Radiator gas	$p_{\pi,threshold}$ [GeV/c]	$p_{\pi,threshold\text{-}max}$ [GeV/c]
CH_4	4.68	10.7
40%He + 60%CH_4	5.9	13.5
C_4H_{10}	2.26	5.20
50%N_2 + 50% C_4H_{10}	2.97	6.83

Whereas radiator gases like CH_4 or, in particular, He/CH_4 mixtures allow to discriminate electrons from pions up to the highest momenta of interest (~10 GeV/c from J/ψ decays), C_4H_{10} and its mixtures with N_2 allow to identify high momentum pions and still discriminate pions and electrons within a wide range of momenta (< 5-7 GeV/c). In combination with a time-of-flight wall to discriminate low momentum pions from kaons this would allow full particle identification over a wide range of momenta. At highest momenta asymptotic rings are attributed solely to pions unless the transition-radiation detector identifies the electrons. Figure 3.38 shows simulated rings for electrons and a 10 GeV/c^2 pion. A mean number of 1.8 fired pads per detected photon and a pad size of 13.2x13.2 mm^2 is assumed. The pion induced ring can be clearly separated due to its smaller diameter.

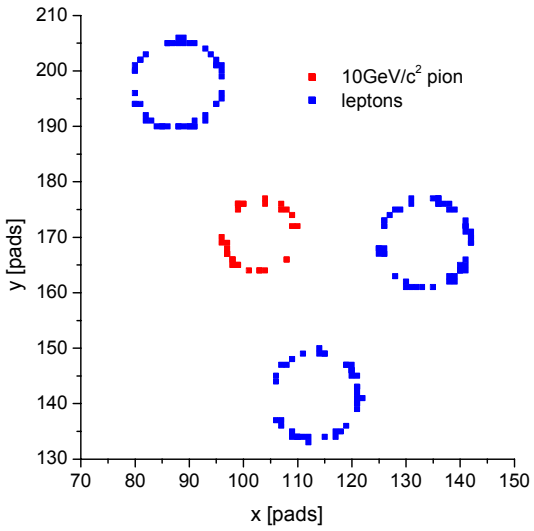

Figure 3.38: Simulated rings for a gas mixture of 40%He and 60%CH_4.

Readout

Assuming a ring radius of 8 pads (Hades RICH: 4 pads), the pad size amounts to typically 13x14 mm^2. This results in 14000 pads per sector and altogether 84000 pads to be read out. As long as no detailed background simulations are available only crude estimates are possible regarding the amount of data to be read out. Assuming an occupancy of 1-2%, 1 byte to specify rows and columns, respectively, and 1 byte to store pulse height, a typical event size could be 2.5-5 kB. An alternative approach is to assume typically 10 rings/event (30 pads/ring), 50 charged particles (10 pads/particle), 100 uncorrelated UV photons and 0.1% electronic noise. This results again in about 1000 fired pads / event and an event size of 3 kB. The numbers stated above refer to a measurement with a high $\gamma_{threshold}$.

RICH Summary

The ring imaging Cherenkov detector based on currently available technologies can cover the full acceptance range. It provides either lepton identification in the full momentum range or can be used to separate high momentum pions from kaons with limited lepton identification depending on the radiator gas.

3.2.2.5 The TOF Stop Detector

Introduction

The development of Resistive Plate Chambers (RPC) has made significant progress during the last few years [100,101]. More recently in the framework of the ALICE collaboration time resolution under 50 ps with an efficiency higher than 99 % were achieved using four gap single Glass RPC [102]. A system with 32 chambers was tested successfully, giving an average resolution of 88 ps at 97 % efficiency [103]. The

rather reduced cost and simple construction make the GRPC technique very attractive for large Time of Flight (ToF) systems compared to scintillators.

The proposed GRPC array has an area of 120 m^2 with a granularity of about 35000 individual detectors. Their area ranges from 4 cm^2 at small deflection angles to 100 cm^2 at larger angles. The total number has been estimated assuming an occupancy below 5 % for a central Au+Au collision at 25A GeV.

Detector Principle

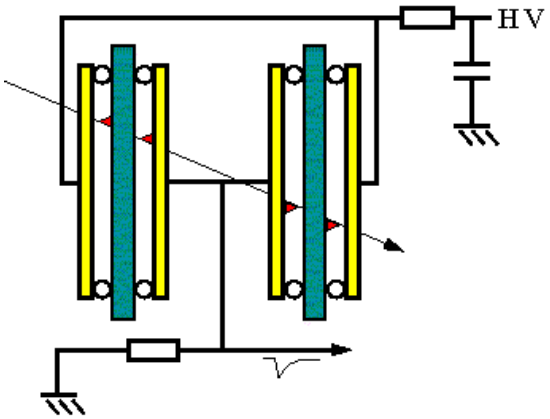

Figure 3.39: schematic view of a GRPC cell.

A schematic cross section of a single four gap GRPC is depicted in Figure 3.39. In this example, the detector consists of two double gap chambers. The middle electrode is made out of glass ($\rho \sim 10^{12}$ Ω·cm) whereas the others electrodes are metallic, generally aluminum to keep the radiation length as low as possible (~5 % X_0). A negative potential is applied to the electrodes whereas the readout signal is taken from the inner ones. The gap distance is maintained by 300 µm spacers (fibers). Various modifications of this principle are feasible as long as each gap is limited by at least one glass plate (instead of a bulk metal plate as HV electrode one may also use another glass plate covered by a metallic foil on its outer side). The detectors are kept under a continuous flow of non-flammable gas consisting of 85 % of freon + 5 % iso-butane and 10 % of sulfur hexafluoride (SF_6). The content of SF_6 ensures to a large extend the suppression of streamers when operating the GRPC in avalanche mode [104].

Results of Prototypes Tests

Encouraged by the excellent time response obtained by single cell GRPCs, the FOPI collaboration at GSI, in a joint effort with the LIP Coimbra, has started the development of GRPCs in view of the ToF upgrade [105,106].

Several different prototypes of GRPCs were tested under beam at GSI and at CERN. At the CERN-PS accelerator, a secondary beam of mostly negative pions at 3.5 and 7

GeV/c momentum was used. The counting rate did not exceed 150 Hz/cm^2. The rate capabilities of the chamber will be discussed in more details at the end of this chapter. Two prototypes were tested during this run: a single cell detector of 5 cm diameter and a 160 × 12 cm^2 large counter with 5 cm wide readout strips. More details about the design and results of the test beam with those GRPCs could be found in ref. 107-110]. The multi-strip GRPC described below was tested with protons of 1.5 GeV at GSI. The rates were similar to those in the other experiments. The counter has an active aera of 90 × 4 cm^2 [106].

Single Cell Chamber

A schematic view of the 5 cm diameter chamber is shown in Figure 3.40. This chamber has the same characteristics as the one described above with two main differences. There are no spacers to maintain the gap, the glass and aluminum electrodes are glued and soldered on a printed board respectively. The glass plates are not on a floating potential but are kept by a resistive voltage divider at half of the voltage applied to the chamber. The readout of the inner electrodes is performed through an aluminum disk. The induced signal is readout on two opposite points of this disk. The signals are directly connecting to a pre-amplifier placed inside the gas volume.

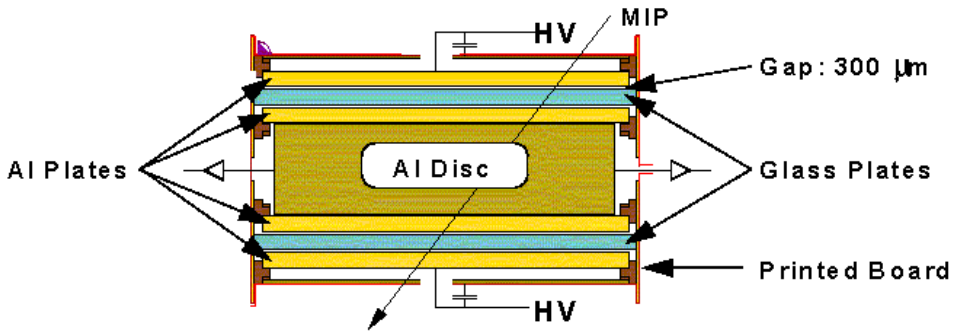

Figure 3.40: layout of the ∅ 5 cm GRPC. The four aluminum plates and the two glass plates are soldered or glued onto a printed board providing the 300 µm gap where the gas flows. The signal is read out on two sides via an aluminum disk and fast pre-amplifiers.

Large Chamber

A large area GRPC has been developed at LIP [107,108], experiments as Harp [111] at CERN were strongly interested in such development for their ToF system. Since large area chambers reduce drastically the number of cells, this option is very attractive. A schematic view of the 160 × 10 cm^2 large chamber is shown in Figure 3.41.

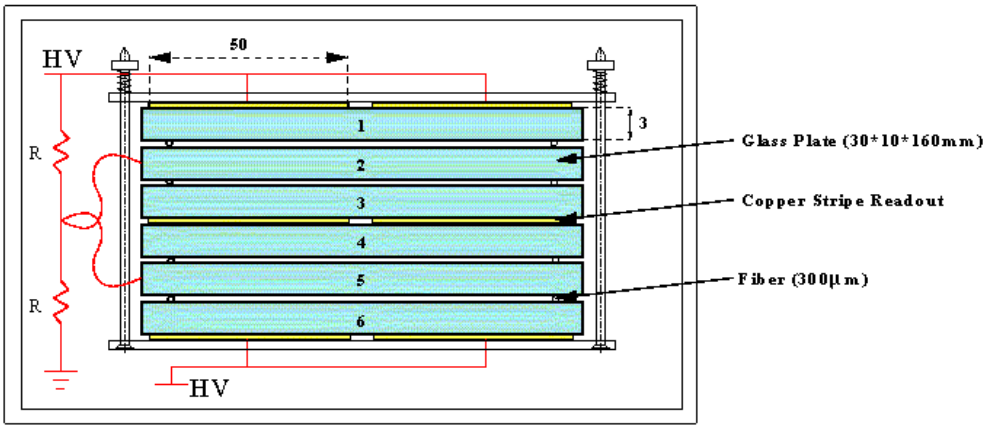

Figure 3.41: layout of the large area GRPC.The stack of six floating glass plates with attached copper foil strips. Regularly spaced spring-loaded plastic bars maintain the stack. The spacers beneath the pressing bars delimit the gaps.

The detector is built from 3 mm thick floating glass with an area of 160 × 12 cm^2 with a measured resistivity of $\rho \sim 2 \times 10^{12}$ Ω·cm. The stack of plates with attached copper foil electrode strips is mounted on a supporting 1 cm thick acrylic plate; controlled pressure is applied to the stack by means of regularly spaced spring-loaded plastic bars. The four gaps are maintained with 300 µm fibers placed beneath the pressing bars. The six individual electrodes strips (160 × 5 cm^2) have a 1 mm inter-space distance leaving an uncovered 1 cm wide region on the outer rim of the glass plates.

Multi-strip Counter

Counters of large active areas as in the previous case require a two-side readout for mean-timing. This principle can be combined with an anode subdivided in narrow parallel strips which increases the detector granularity. In addition such counters offer a position resolution in two dimensions.

A first prototype was 90 cm long and 4 cm wide, conceptually similar to the one sketched in Figure 3.41. The glass plates were only 1 mm thick; the whole setup was hold by a polycarbonate structure placed inside of a tube of 0.5 mm wall thickness. The readout plane in the middle of the stack is 0.6 mm thick and has 12 individual conductive strips with a pitch of 3.44 mm (1.44 mm gap).

Results of the Single Cell

Figure 3.42a shows a time spectrum measured at 6.3kV high voltage. The GRPC was irradiated in its center over an area of about 3 cm^2. The chamber signal is readout on the two sides and the average value is plotted (double readout). Since the time response is not a purely gaussian shape, the absolute tail is defined as the proportion of events outside the window ± 300 ps with respect to the total number.

The intrinsic resolution is then around 50 ps with a proportion of absolute tail less than 0.1 %, while the efficiency is higher than 99 %. The proportion of streamer events was about 20 % of the total number of events in this case. One should stress here that for non-minimum ionizing particles, the probability of operating in streamer mode increases, even with an important proportion of a strong electro-negative gas as SF_6. In Figure 3.42b the time response is plotted for a 60 % proportion streamer events, when applying a 6.5 kV high voltage. The intrinsic resolution is still below 60 ps, while the absolute tail is less than 0.3 %. Therefore streamer events do not destroy the resolution of the chamber but only affects the time response in a moderate manner.

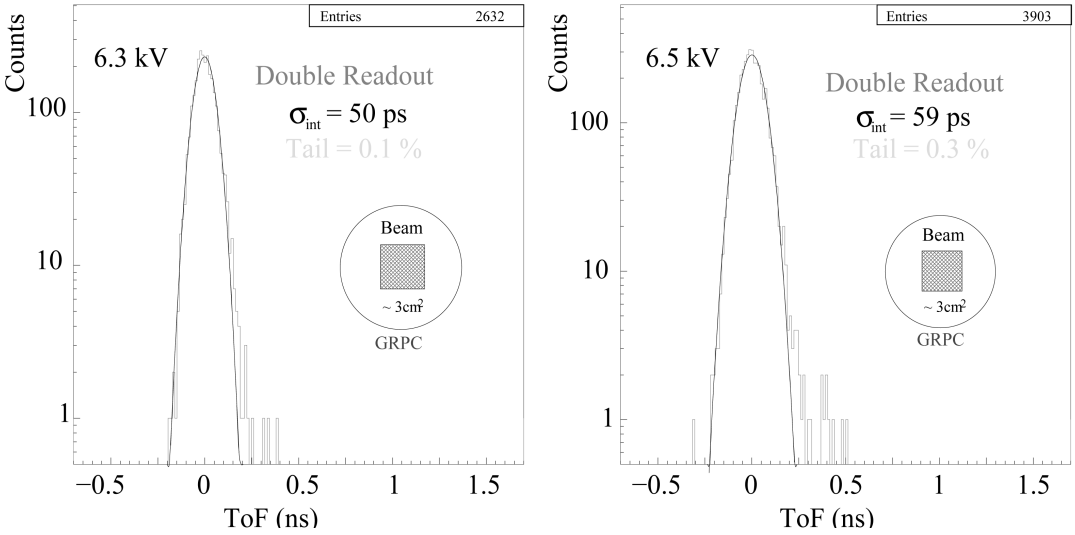

Figure 3.42: ToF spectrum of the 5 cm GRPC when irradiating the center of the chamber, in a double readout mode. Panel a) shows the ToF spectrum measured at 6.3 kV whereas panel b) shows the spectrum measured at 6.5 kV (60 % streamer events).

Results with the Large Chamber

The ToF spectrum shown in Figure 3.43 was obtained by irradiating the center of one strip. The intrinsic resolution is in the order of 55 ps with a tail less than 1 %. Along the middle axis of one strip the dependence of the efficiency, resolution and absolute tail were measured for various positions. The intrinsic resolution has a rather flat dependence, it ranges from 50 ps to 70 ps with a tail proportion less than 1.5 %. The efficiency in this case is always higher than 97 %. The propagation velocity of the signal along a strip was deduced from the time difference between both strip ends, leading to a value of 14.1 cm/ns. The corresponding position resolution was found to be about 12 mm σ.

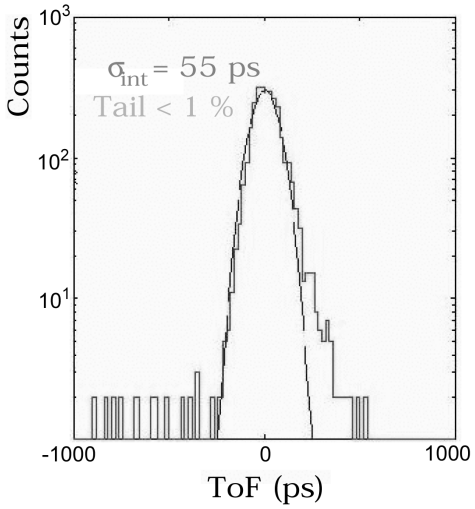

Figure 3.43: ToF spectrum of the large area GRPC when irradiating the center of one strip.

Results with the Multi-Strip Detector

In the mentioned first tests, resolutions of 70 to 80 ps were reached at 95 % efficiency. This value was rather constant along the counter as well as among the readout strips. The time difference between the ends delivers a position along the counter within 5 to 6 mm. The hit position in perpendicular direction is derived by averaging the charge recorded on neighbouring strips yielding resolution below 1 mm.

Rate capabilities of GRPCs

One of the main issue when using GRPCs in high density particle experiments is the rate capability of the chambers. Measurements with the large chamber of Figure 3.41 were performed as a function of the rate [108]. Figure 3.44 shows the efficiency and the resolution of the chamber for increasing counting rate density. A slight degradation of the response is observed up to 300 Hz/cm² (σ ~ 60 ps, ε ~ 96 %) compared to the nominal value of 140 Hz/cm² (σ ~ 50 ps, ε ~ 97 %).

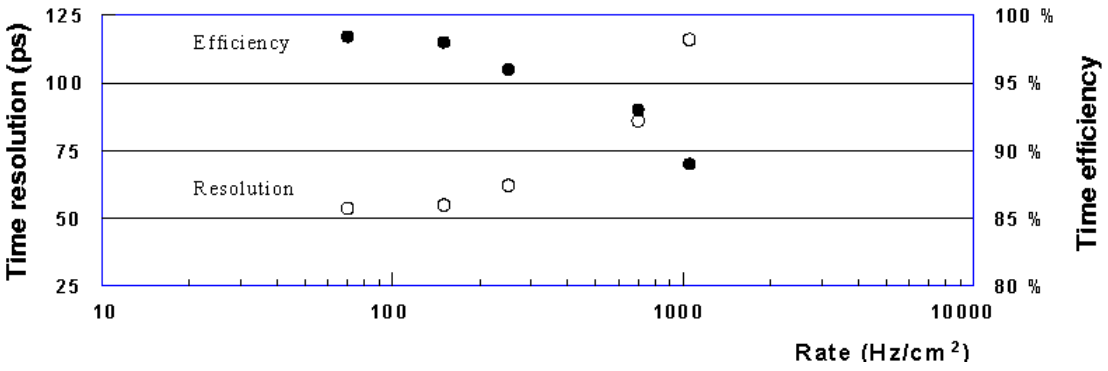

Figure 3.44: Efficiency and resolution for the large area chamber (see Figure 3.41) as function of counting rate density.

A more pronounced deterioration starts with rates higher than 500 Hz/cm^2. Since the rate capability is probably related to the resistivity of the glass electrodes, an improvement can be achieved when using glass with lower resistivity. The chamber used for the measurement has a bulk resistivity of $\rho \sim 2.\ 10^{12}$ Ω.cm, commercial "dark glass" (Schott 8540) is available with a resistivity of the order of few 10^{11} Ω.cm. Therefore the rate capability of the chamber should be improvable.

According to simulated UrQMD events in Au+Au central collisions the maximum particle density for a detector placed 5 m downstream the target should not exceeded 0.06 particles/cm^2. The maximal flux of particles hitting the plane at that given distance is in the order of 20 kHz/cm^2. Since the GRPC plane is placed at 10 m downstream, the maximum rate should be close to 5 kHz/cm^2.

Conclusion

The very promising results of the GRPCs, single cells or large chamber with and without multi-strip readout support the proposition of a GRPC detector array for the ToF Stop Detector. Nevertheless further developments are necessary in order to cope with the high flux of particles measured with a GRPC ToF detector.

3.2.2.6 Data Acquisition and Trigger

The data acquisition system has to provide i) the necessary bandwidth to process enough events to record a sufficiently large number of rare probes and ii) the flexibility to adjust to the different physics needs.

Aiming at reaction rates of 10^6 interactions per second with a 4π like detector is a challenging task corresponding to an equivalent Luminosity of $L = 6\ 10^{30}$ cm^{-2}s^{-1} for collider experiments.

Table 3.9: Subevent Data Sizes in bytes for various levels of data reduction[4]

	Raw	Hits	Tracks
TRD	5M	500k	100k
Silicon	0.5M	50k	50k
RICH	0.1M	10k	1k
TOF	70k	7k	7k

[4] The numbers are calculated for a multiplicity of 700 primary charged particles emitted into the acceptance of the detector causing the same number of secondaries being produced in the detector. Minimum bias events will have on average at most half of the listed event sizes.

With the data volumes presented in Table 3.9 for the various detector subsystems and a event size of 600 kbyte for central collisions on the Hit level it is obvious that the experiment needs a sophisticated trigger, readout and data reduction scheme in order to reconcile the data archive rate with manageable writing speeds. Online reconstruction of tracks leads to an event size of 160 (40) kByte for central (minimum bias) events. From present day knowledge a DAQ output rate of 1 GB/s (100TB/day) appears to be an upper boundary limiting the event rate to 6.2 (25) kHz for central (min bias) triggers.

The strategy of the trigger/data acquisition system is to fill the maximum tolerable data archive rate with different parallel triggers that can be generated for the different physics signatures.

Charmonium (J/ψ)

J/ψ events can be enhanced by requiring two high p_t electron candidate tracks of opposite charge. This information can be derived from the TRD detector with a pion misidentification probability (pion efficiency) of 1% at an electron efficiency of 90% within 5μs [112]. Full event tracking in addition allows to reduce the data volume from hit to track level. With 4 pions of p_t>1GeV/c emitted per central collision the probability for triggering on false pion pairs is $1.6 \cdot 10^{-3}$ per central collision (10^{-4} for minimum bias events). The number of false triggers can be further suppressed by requiring a match with a ring in the RICH detector for which an electron pion suppression of 10^{-2} is expected for p_{lab} > 1GeV/c. The main background in the procedure originates from accidental matches of TRD tracks and the centers of the circles in the RICH.

Open charm (D-mesons)

Since D mesons provide the natural reference for J/ψ yields their measurement within the same class of events is of crucial importance. The characteristic features are: they are produced in pairs and decay after a mean lifetime of cτ=317 (124) μm for the $D^{\pm}$ (D^0). 17 (6) % decay semileptonically into an electron + anything. The trigger therefore requires: a) an electron candidate in the RICH/TRD in coincidence with b) a displaced vertex from the silicon system. In order to obtain a reasonable efficiency for the D-mesons a relatively low transverse momentum threshold for the electron is necessary. The background surviving a p_t - threshold of 0.4 GeV/c originates from Dalitz decays of neutral pions ($5 \cdot 10^{-2}$ per central event) and from misidentified pions ($8 \cdot 10^{-2}$ per central event). This results in a total trigger probability of $3.3 \cdot 10^{-2}$ per event for minimum bias collisions. An additional online vertex trigger processor is envisaged to reduce the input trigger rate by another factor of 2. Its selectivity is limited due to the small distances of the decay vertices from the primary vertex.

Multistrange baryons

Due to their weak decay and their long lifetimes cτ=2.46 (4.91) cm for the $\Omega^-(\Xi^-)$, those particles can be tagged by detecting displaced vertices with the Silicon system.

Typical online vertex processor enhancement ratios are of order 10. Due to the expected large multiplicities of multistrange particles, however, there is no special trigger required for this observable.

The experiment should be able to cope with both central and minimum bias conditions, since all of the signatures will have to be studied as function of the impact parameter. The rate estimates for the different trigger levels, as well as the accumulated events per week of running are summarized in Table 3.10 (a machine duty cycle of 80% was assumed for the estimate of the number of events). The interaction rate of 10^6Hz is limited by the drift time of the TRD drift chamber which is about 1 μs for the detector type tested for ALICE. Alternative detector designs as envisaged for ATLAS have drift times of 100 ns. The use of such detectors at least for the region of small scattering angles would permit event rates of 10^7 Hz in accordance with the rates given in Table 3.2.

To accommodate these needs we propose a trigger system as sketched in Figure 3.45. Note that the minimum bias condition requires the Level 1 processes to run at 1MHz. For the TRD tracking trigger the electron drift time of 1.5 μs implies the necessity to handle the pile-up of events. On average 1.5 events will occur within 1.5 μs. To disentangle the different events the processing of the TRD data will be tagged by a coincidence of the Level 0 trigger with the beginning of the drift time. Once such a coincidence is registered the neighboring pads in x and y direction are also activated for readout. With an occupancy of less than 10% at least 90% of all of the detector pixels are available to register new events.

Table 3.10: Trigger rates

Process	Event Rate	Data Rate (Track level)	Accumulated events / week
Interactions	10^6 Hz		
J/Ψ			
Signal (detectable e^+e^- pairs)	0.02 Hz		9600
Misidentified pion pairs			
Minimum bias (TRD)	100 Hz	4 MB/s	$4.8\cdot 10^7$
Minimum bias (TRD+RICH)	10^{-2} Hz	0.4 kB/s	$4.8\cdot 10^5$
D mesons			
Signal	$2.4 \cdot 10^{-4}$ Hz		116
Single Electron Trigger			
Minimum bias (TRD)	10^6 Hz	40 GB/s	$4.8\cdot 10^{11}$
Minimum bias (TRD+RICH)	$3.3 \cdot 10^4$ Hz	1.3 GB/s	$1.6\cdot 10^{10}$
Minimum bias (TRD+RICH+VTX)	$1.6 \cdot 10^4$ Hz	0.7 GB/s	$7\cdot 10^9$

Figure 3.45: Trigger block diagram with rate estimates for the reaction Au+Au @ 25 GeV/u

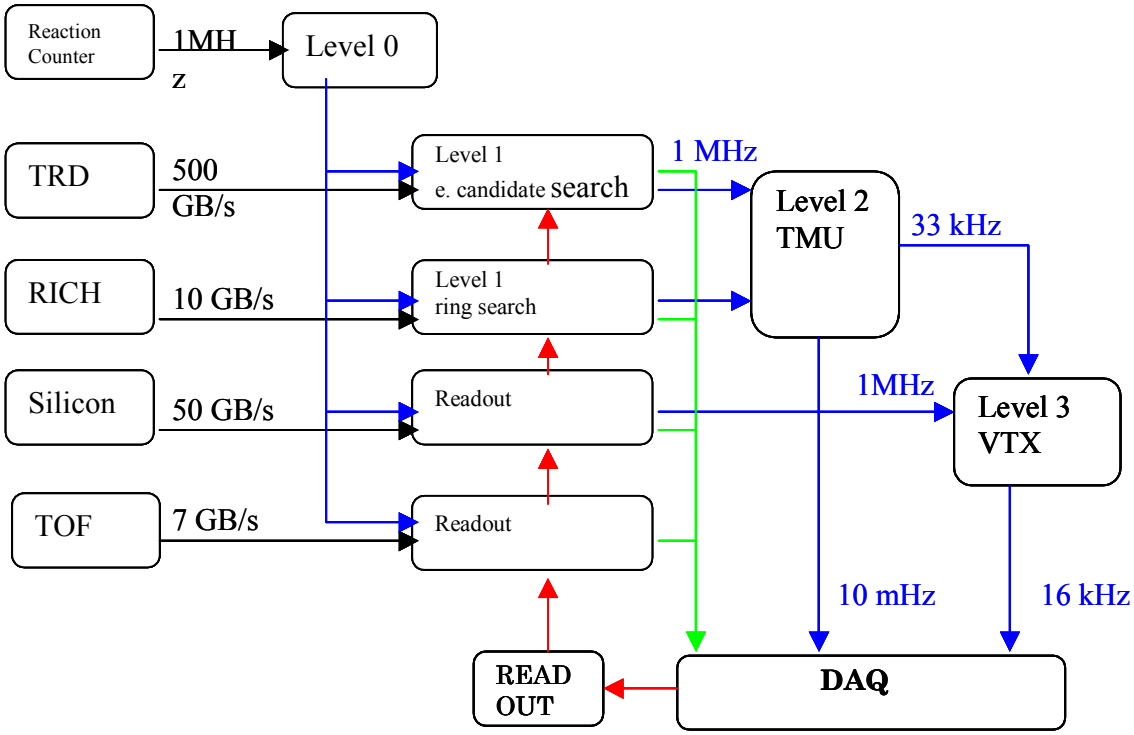

The Silicon detector system will have to take the full primary interaction rate. This trigger and readout rates of 1MHz have to be processed. Similar trigger rates are envisioned for Silicon tracking systems at LHC (LHCb) and require the application of ASIC based electronics. A trigger latency of 256 μs is planned for LHCb. With the data volume increased by a factor of 10 with respect to LHCb we estimated a VTX trigger latency of 1ms.

The synchronization of the subevents will be done on the basis of the Level 0 signal with an accuracy of 50ns (20 MHz). If no readout signal is issued from the DAQ system after a latency time of about 1ms (estimated for the VTX Trigger) the data stored in the readout pipes are discarded. The Level 1 processes therefore have to store the information of 10^3 events in the Level 1 readout pipes. The largest readout pipe (for the TRD) has a size of 0.5 Gbyte.

The data acquisition architecture will be based on a network of high speed links from the various data sources to the data storage nodes through a switch making use of commercial components. Such architectures are flexible and scalable and provide the necessary bandwidth for data rates as high as 1.25 Gbyte/s [112].

3.2.3 Performance simulations

3.2.3.1 GEANT simulations

In order to design the experiment we have performed simulations using the GEANT 3.21 code [113]. The setup as implemented in GEANT consists of a homogeneous magnetic field of B= 1 Tesla of 1 m length, a 1% interaction Au-target, 7 layers of Silicon of 300 μm thickness each inside the magnetic field and a detector at a distance of 5 m downstream from the target. In the calculation we assume that the beam and the particles propagate in vacuum. As event generators we have used the URQMD transport code [73] of the Frankfurt group and the program PLUTO [114] which was developed for the simulation of the HADES experiment. PLUTO generates a thermal source that emits the particles isotropically and moves with the center-of-mass velocity of a symmetric collision system at a given beam energy. The particle multiplicities and the inverse slope parameters were adopted from the URQMD results. One should keep in mind that the URQMD calculation seems to overpredict the pion multiplicities (as interpolated from data, see Table 3.1) by a factor of 1.7 – 1.9. Therefore, the calculated numbers on occupancies, background and data rates can be regarded as upper limits.

Figure 3.46 shows the trajectories of charged particles from a central Au+Au collision at a beam energy of 25 GeV/u as calculated with URQMD. The green, blue and red tracks correspond to negative pions, protons, and positive pions, respectively. The magnetic field is B = 1 T.

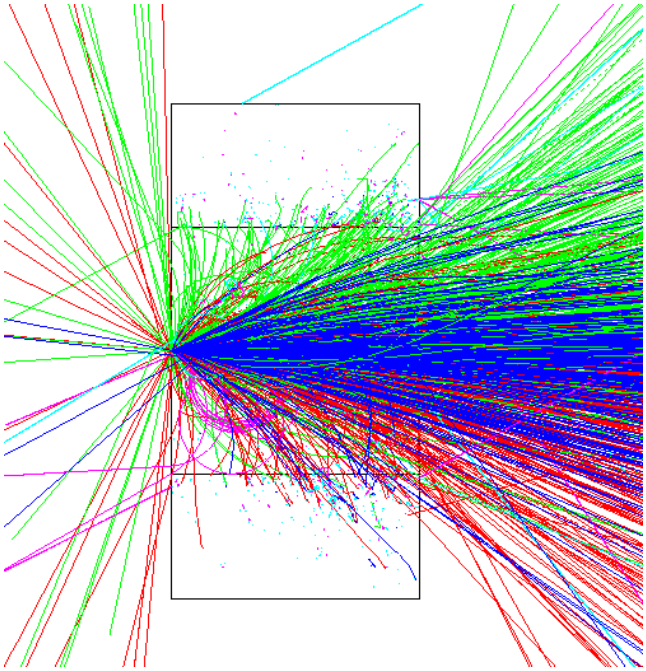

Figure 3.46: Charged particle tracks from a central Au+Au collision at 25 GeV/u as simulated with GEANT using URQMD as event generator. The magnetic field is B = 1 T.
Color code: negative pions (green), positive pions (red) and protons (blue). The tracks are projected onto the horizontal symmetry plane of the magnet.

Acceptances

Figure 3.47 shows the accepted phase-space distributions of protons, pions and kaons in the transverse momentum versus rapidity plane for a central Au+Au collisions at 25 GeV/u using PLUTO as event generator. In this case the magnetic field is B = 1 T. The red line corresponds to a polar angle of θ_{lab}=25° which is defined by the pole shoes of the magnet. A particle is accepted if it hits a detector that is positioned 5 m downstream from the target. This definition includes pion and kaon decays in flight. The calculated acceptances for various particles are given in Table 3.11.

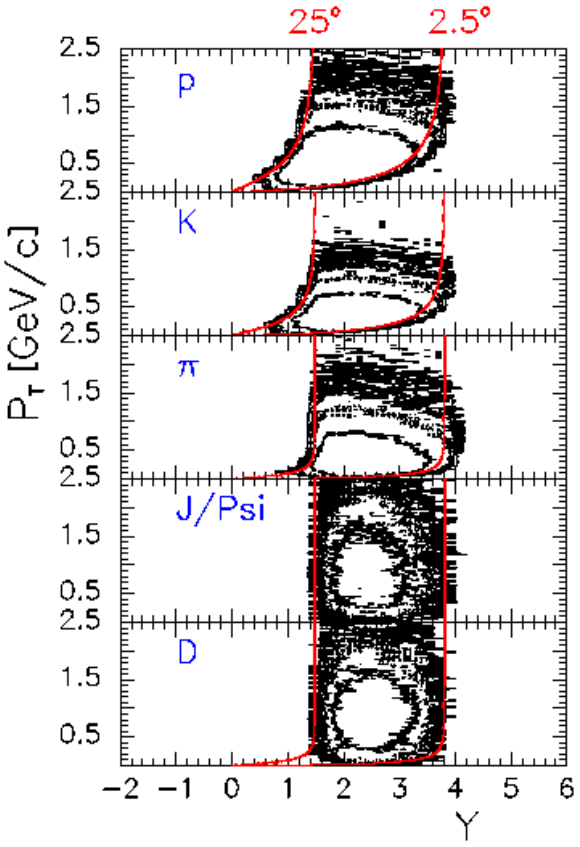

Figure 3.47: Phase space distributions of protons, kaons and pions from central Au+Au collisions at 25 GeV/u as calculated with GEANT using the PLUTO event generator. The red line corresponds to a laboratory polar angle of 25° defining the geometrical acceptance (midrapidity is at y=2).

Table 3.11: Acceptances for particles emitted in a Au+Au collision at 25 GeV/u (definition see text)

Particle	**Acceptance**
protons	0.86
pions	0.70
kaons	0.64
$J/\psi \rightarrow e^+e^-$	0.20
$D \rightarrow K \pi\pi$	0.40

At a beam energy of 10 GeV/u still about 50% of the participants are accepted within this angular range. If one aims for complete coverage in at least one hemisphere it is sufficient to accept polar angles up to $\theta_{lab}=25^{o}$.

Particle densities

In order to estimate the occupancy of the TRD and the RPC detectors we have calculated the particle density at a detector plane 5 m downstream of the target. Figure 3.48 presents the hit pattern of charged particles from a central Au+Au collision (URQMD event) in this detector plane. The particles are deflected by a magnetic field of B = 1 T. Figure 3.49 shows the number of charged particles per 100 cm^2 within a vertical and a horizontal window both 10 cm wide and crossing in the center of the detector.

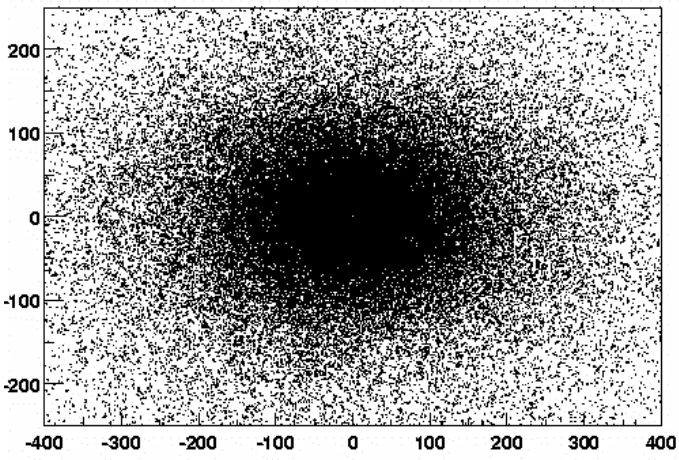

Figure 3.48: Hit pattern of charged particles from a central Au+Au collision at 25 GeV/u in a detector plane 5 m downstream the target. The magnetic field is B = 1 T (units in cm).

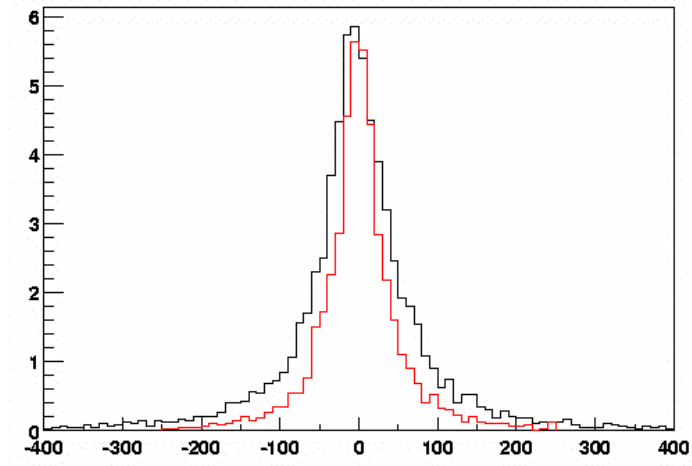

Figure 3.49: Particle density N/100 cm^2 along the horizontal axis (black line) and along the vertical axis (red line) within 10 cm wide windows which cross the center of the detector (units in cm).

Delta electrons

Using the GEANT code we have calculated the production of δ-electrons by Au ions impinging on a (1 % interaction) Au target with an energy of 25 GeV/u. About 3 electrons are produced per beam ion with energies above 60 MeV (corresponding to a radius of 20 cm in a magnetic field of B = 1 T). The count rate of δ-electrons seen by the Silicon tracking detectors is discussed in section 3.2.2.2.

3.2.3.2 Momentum Resolution

According to Figure 3.26 the transverse momentum kick is about p_T = 0.3 GeV/c for Bρ = 1 Tm (i.e. a constant field of B = 1 T over 1 m length). For a single charged particle with a momentum p and an incident angle of θ_{lab}= 0 the deflection angle is θ = atan(p_T/p) and the displacement at the exit of the dipole is x = 0.5 m tanθ. The resolution can be estimated by Δp = d/x with d = 50 μm the width of the Silicon strip detectors. Table 3.12 presents values for θ, x and Δp for different particle momenta and Bρ = 1 Tm.

The influence of multiple Coulomb scattering in the Silicon detectors on the momentum resolution is calculated using formula 23.9 in the Particle Physics Booklet [115]. We assume scattering in 8 layers of Silicon detectors of 300 μm thickness each. The width of the angular distribution θ_{mcs} and the resulting position uncertainty x_{mcs} =0.5 m tanθ_{mcs} are also listed in Table 3.12. The momentum uncertainty $\Delta p_{mcs} = x_{mcs}/x$ caused by multiple Coulomb scattering is $6.4 \cdot 10^{-3}$ for all momenta.

Table 3.12: Deflection angle, dispersion, momentum resolution, and their uncertainties due to multiple Coulomb scattering for single charged particles with different momenta

p [GeV/c]	θ [°]	x [cm]	Δp [10^{-3}]	θ_{mcs}[°] [10^{-2}]	x_{mcs} [cm] [10^{-2}]	Δp_{mcs} [10^{-3}]
1	17	15	0.33	11	9.6	6.4
2	8.5	7.5	0.66	5.5	4.8	6.4
4	4.3	3.75	1.3	2.75	2.4	6.4
6	2.86	2.5	2.0	1.8	1.57	6.4
8	2.14	1.9	2.6	1.37	1.2	6.4
10	1.72	1.5	3.3	1.1	0.96	6.4

3.2.3.3 Combinatorial background in charmonium experiments

The combinatorial background in the dielectron invariant mass spectrum has been estimated using the thermal source event generator PLUTO. We have calculated combinatorial background of electrons and positrons from the Dalitz decays $\pi^0 \rightarrow \gamma e^+ e^-$ and $\eta \rightarrow \gamma e^+ e$, from misidentified charged pions and from the leptonic decays of ρ and J/ψ. Figure 3.50 shows the transverse momentum spectrum of electrons and positrons

from these sources: the Dalitz decay of π^0 (black) and η (blue), from the dilepton decay of J/ψ (red) and from misidentified pions (green). The green histogram corresponds to the charged pion transverse momentum spectrum scaled with 10^{-4} according to the product of the pion suppression factors of RICH and TRD (10^{-2} each). Due to the large mass of charmonium the mean transverse momentum of its decay electrons is much larger than the mean p_T of the electron spectra from the pion and eta decays. Therefore, a condition on the electron transverse momentum ($p_T > 1$ GeV/c) will reduce the combinatorial background by several orders of magnitude.

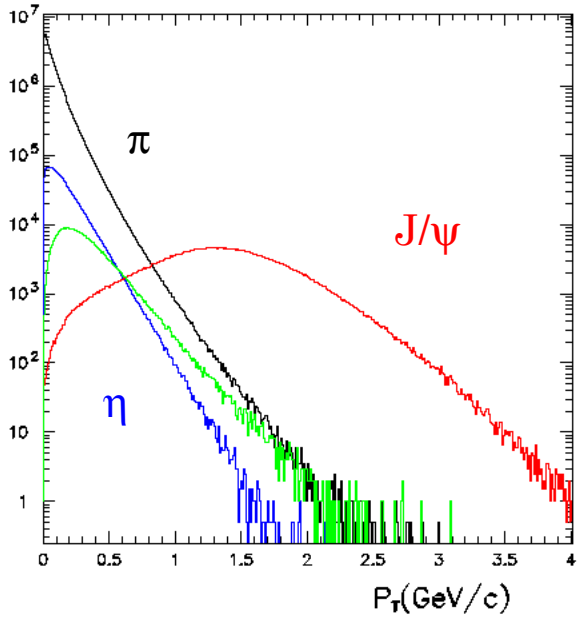

Figure 3.50: Electron and positron transverse momentum spectrum from the Dalitz decays of neutral pions (black), etas (blue) and J/ψ (red). The green histogram represents the charged pion spectrum scaled by 10^{-4} according to the expected contribution of misidentified pions.

In a first step we have calculated the combinatorial background caused by physical sources and misidentified pions. We have neglected the conversion in detector materials and the magnetic field. In order to simulate the J/ψ peak in the invariant mass spectrum we have calculated with one J/ψ per central collision but then scaled down the result by 10^{-5} according to the true multiplicity. Figure 3.51 displays the dilepton invariant mass spectrum including the combinatorial background without any condition on the leptons as simulated for 10 million events. The black histogram represents the combinatorial background of all physical electron sources including misidentified pions. In addition to the Dalitz-decays of π^0 (green) and η mesons (blue) and the leptonic decays of ρ (pink) and J/ψ mesons (red) we have taken into account the semi-leptonic decay of $D\overline{D}$ pairs (light blue).

In order to suppress combinatorial background we require the following conditions: (i) the lepton transverse momentum in larger than p_T=1GeV/c, (ii) the dilepton opening angle is larger than $\alpha=10^o$ and (iii) the polar angle acceptance of the detector is $\theta_{lab}<25^o$. It turns out that for 10 million events 1.6 dielectron pairs from the J/ψ and 8

background entries survive these conditions. The cut on transverse momentum is most effective: it is extremely unlikely that both electrons from two independent Dalitz decays have a p_T larger than 1 GeV/c. The J/ψ peak has a width of = 60 MeV FWHM. The signal to background ratio is about 10.

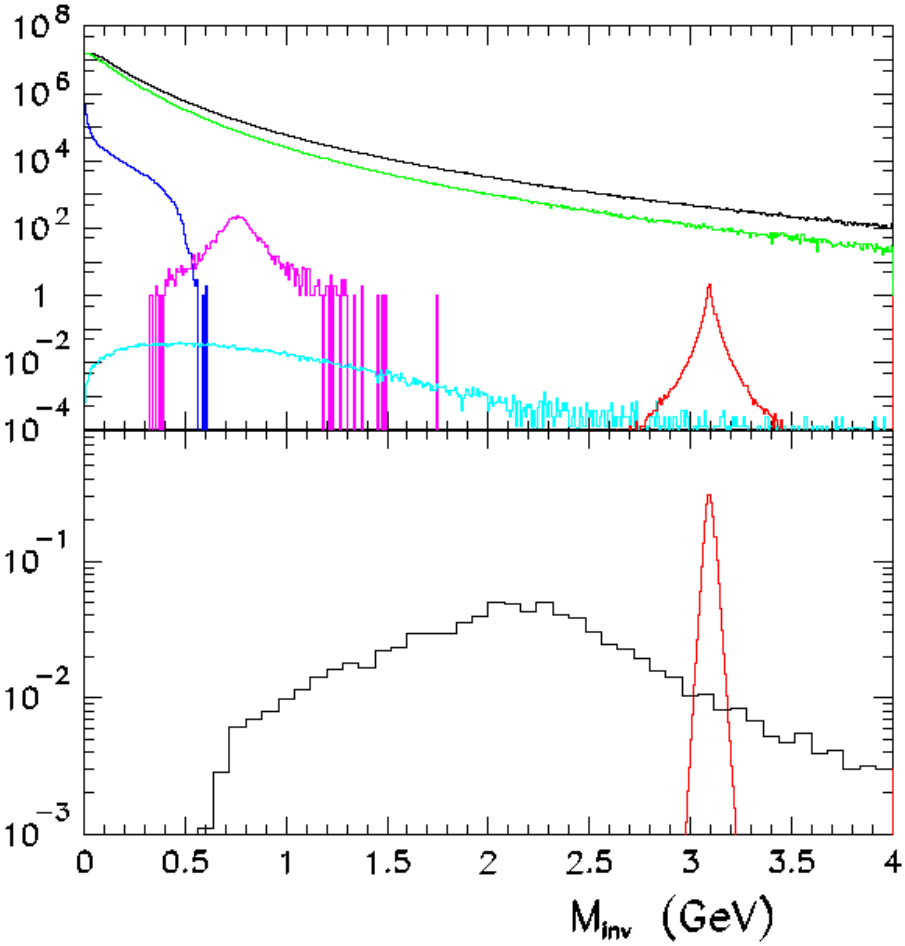

Figure 3.51: Di-electron invariant mass spectrum including combinatorial background as indicated without any conditions (upper panel) and with conditions (lower panel) (see text). Color code: π0 Dalitz decay (green), η Dalitz decay (blue), ρ pair decay (pink), $D\overline{D}$ decay (turquoise), J/ψ pair decay (red), sum (black)

Acknowledgment

This chapter, as all the other chapters of this document, was prepared with the help of many individuals. The appendix lists the names of all the individuals involved in the CDR document, from the contributions to the science discussions, workshops and working groups to the research and development, the detailed scientific and technical planning activities, and, last not least, the drafting of this Conceptual Design Report.

The concepts and presentations of the science and technical plans in this chapter were in particular developed by the following authors:

Anton Andronic, Peter Braun-Munzinger, Christian Finck, Bengt Friman, Norbert Herrmann, Romain Holzmann, Jörn Knoll, Wolfgang Koenig, Mathias Lutz, Peter Senger, Yanghwan Shin, Reinhard Simon, Herbert Ströbele, Joachim Stroth

Collaborating institutes and contact persons

- P. Senger,
  GSI Darmstadt
- H. Oeschler
  Institut für Kernphysik, TU Darmstadt,
- H. Ströbele
  Institut für Kernphysik, Univ. Frankfurt,
- N. Herrmann
  Physikalisches Institut, Univ. Heidelberg,
- V. Lindenstruth
  Kirchhoff Institut für Physik, Univ. Heidelberg
- E. Grosse
  TU Dresden and FZ Rossendorf
- Paolo Finocchiaro
  Instituto Nazionale di Fisica Nucleare, LNS, Catania, Italy
- F. Rami
  Institut de Recherches Subatomiques, IReS ,
  IN2P3-CNRS/ULP, Strasbourg, France
- P. Salabura
  Institute of Physics, Jagiellonian University, Cracow, Poland
- B. Sikora
  Institute of Experimental Physics, Nuclear Physics Division,
  Warszawa, Poland
- P. Fonte
  ISEC/LIP, Coimbra, Portugal

- M. Petrovici
  Institute for Physics and Nuclear Engineering IPNE, Bucharest, Romania
- J. Kecskemeti
  Research Institute for Particle and Nuclear Physics, KFKI, Budapest, Hungary
- F. Deak
  Eötvös University, Budapest, Hungary
- A. Kugler
  Czech Academy of Sciences, Rez, Czech Republic
- Stanislav Hlavac
  Slovak Academy of Sciences, Bratislava, Slovakia
- M. Korolija
  Rudjer Boskovic Institute, RBI, Zagreb, Croatia
- F. Guber
  Institute for Nuclear Research., Russ. Acad. of Science, Moscow, Russia
- V. Manko
  Russian Research Center “Kurchatov Institute”, Moscow, Russia
- A. Zhilin
  Institute for Theoretical and Experimental Physics, ITEP, Moscow, Russia
- Y. Murin
  Radium Institute, St. Petersburg, Russia
- B. Hong
  Department of Physics, Korea University, Seoul, Korea

References

[1] F. Weber, J. Phys. G: Nucl. Part. Phys. 27 (2001) 465

[2] F. Wilczek, Physics Today 53 (2000) 22

[3] J.C. Collins and M.J. Perry, Phys. Rev. Lett. 34 (1975) 1353

[4] M.B. Kislinger and P.D. Morley, Phys. Rev. D 13 (1976) 2771

[5] K. Rajagopal, Nucl. Phys. A661 (1999) 150c

[6] G.E. Brown and M. Rho, Phys. Rev. Lett. 66 (1991) 2720

[7] T.D. Cohen, R.J. Furnstahl and D.K. Griegel, Phys. Rev. C45 (1992) 1881;

[8] M. Lutz, S. Klimt and W. Weise, Nucl. Phys. A542 (1992) 521

[9] P. Gerber and H. Leutwyler, Nucl. Phys. B321 (1989) 387

[10] F. Karsch, to be published in the proceedings of Quark Matter 2001 Nucl. Phys. A (2001) in press

[11] D.T. Son and M.A. Stephanov, Phys. Rev. D 61 (2000) 074012

[12] M. Rho, E. Shuryak, A. Wirzba, I. Zahed, Nucl. Phys. A 676 (2000) 273

[13] B. Vanderheyden and A.D. Jackson, Phys. Rev. D62 (2000) 094010

[14] Z. Fodor and S.D. Katz, hep-lat/0106002

[15] M.A. Stephanov, K. Rajagopal and E. Shuryak, Phys. Rev. D 60 (1999) 114028

[16] P. Braun-Munzinger et al., Phys. Lett. B 465 (1999) 15

[17] R. Stock, Phys. Lett. B456 (1999) 277

[18] J. Cleymans and K. Redlich, Phys. Rev. Lett. 81 (1998) 5284

[19] P. Braun-Munzinger, Nucl. Phys. A 681 (2001) 119c

[20] Quark Matter 2001, Proceedings of the 15th int. Conf. on Ultra-Relativistic Nucleus-Nucleus Collisions, Stony Brook, Nucl. Phys. A (2001) in press

[21] G.E. Brown et al., Phys. Rev. C 43 (1991) 1881

[22] T. Waas, N. Kaiser, W. Weise, Phys. Lett. B 379 (1996) 34

[23] M. Lutz, Phys. Lett. B 426 (1998) 12

[24] M. Menzel et al., Phys. Lett. B 495 (2000) 26

[25] D. Best et al., Nucl. Phys. A 625 (1997) 307

[26] K. Wisniewski et al., Eur. Phys. J. A 9 (2000) 515

[27] G. Q. Li and G. E. Brown, Phys. Rev. C 58 (1998) 1698

[28] W. Cassing and E. Bratkovskaya, Phys. Rep. 308 (1999) 65

[29] F. Laue, C. Sturm et al., Phys. Rev. Lett. 82 (1999) 1640

[30] Y. Shin et al., Phys. Rev. Lett. 81 (1998) 1576

[31] P. Crochet et al., Phys.Lett. B 486 (2000) 6

[32] G.Q. Li, C.H. Lee, G.E. Brown, Phys. Rev. Lett. 79 (1997) 5214

[33] C. Fuchs et al., Phys. Rev. C 56 (1997) R606

[34] C. Sturm et al., Phys. Rev. Lett. 86 (2001) 39

[35] C. Fuchs et al., Phys. Rev. Lett. 86 (2001) 1974

[36] L. Ahle et al., Phys.Lett. B 490 (2000) 53

[37] J. Bächler et al., Nucl. Phys. A 661 (1999) 45c and H. Ströbele, priv. com.

[38] M. Gazdzicki, M. Gorenstein, D. Röhrich, hep-ph/0006236

[39] P. Braun-Munzinger et al., hep-ph/0106066
[40] J. Rafelski and B. Müller, Phys. Rev. Lett. 48 (1982) 1066
[41] F. Antinori et al., Nucl. Phys. A 661 (1999) 130c
[42] W. Cassing, nucl-th/0105069, subm. to Nucl. Phys. A
[43] R.J. Porter et al., Phys. Rev. Lett. 79 (1997) 1229
[44] G. Agakichiev et al., Phys. Lett. B 422 (1998) 405
[45] R. Rapp and J. Wambach, Nucl. Phys. A 661 (1999) 33c
[46] T. Matsui and H. Satz, Phys. Lett. B 178 (1986) 416
[47] M. Abreu et al., Phys. Lett. B 477 (2000) 28
[48] F. Klingl, S. Kim, S.H. Lee, P. Morath, W. Weise, Phys. Rev. Lett. 82 (1999) 3396 and W. Weise, Proc. of the XXIX internat. Workshop on gross properties of nuclei and nuclear excitations, Hadrons in Matter, Hirschegg/Austria Jan. 2001
[49] A. Sibirtsev, K. Tsushima, A.W. Thomas, Eur. Phys. J. A 6 (1999) 351
[50] R. Vogt, Phys. Rep. 310 (1999) 197
[51] W. Cassing, E. Bratkovskaya, A. Sibirtsev, Nucl. Phys. A 691 (2001) 745
[52] CERN-SPSC-2001-009, SPSC-M-662, Geneva, CERN
[53] H. Sorge, Phys. Rev. Lett. 78, (1997) 2309
[54] C. Pinkenburg et al., Phys. Rev. Lett. 83, (1999) 1295
[55] P. Danielewicz et al., Phys. Rev. Lett. 81, (1998) 2438
[56] A. Andronic et al., Nucl. Phys. A 661 (1999) 333c
[57] W. Reisdorf and H. G. Ritter, Annu. Rev. Nucl. Part. Sci. 47 (1997) 663
[58] A. Wagner et al, Phys. Rev. Lett. 85 (2000) 18
[59] Z. Wang et al., Eur. Phys. J. A 5 (1999) 275
[60] P. Chung et al., Phys. Rev. Lett. 86 (2001) 2533
[61] B.Friman, W. Nörenberg, V.D. Toneev, Eur. Phys. J. A3 (1998) 165
[62] P. Senger and H. Ströbele, J. Phys. G: Nucl. Part. Phys. 25 (1999) R59
[63] B. Friman, M. Lutz and G. Wolf, In Proc. Int. Workshop on Gross Properties of Nuclei and Nuclear Excitations, Hirschegg, Austria, 2000, p. 161
[64] R. Barth et al., Phys. Rev. Lett. 78 (1997) 4007
[65] A. Sibirtsev et al., Z. Phys. A 358 (1997) 101, Nucl. Phys. A 604 (1996) 455
[66] Bao-An Li, Phys. Rev. C 61 (2000) 021903
[67] A. Hayashigaki, Phys. Lett. B 487 (2000) 96
[68] J.-P. Blaizot, P. M. Dinh, J.-Y. Ollitrault, Phys. Rev. Lett. 85 (2000) 4012
[69] S. Chin, A. Kerman, Phys. Rev. Lett. 43 (1979) 1292
[70] E. Witten, Phys. Rev. D 30 (1984) 272
[71] E. Farhi, R.L. Jaffe, Phys. Rev. C 35 (1984) 2379
[72] C. Greiner, P. Koch, H. Stöcker, Phys. Rev. Lett. 58 (1987) 1825
[73] S.A. Bass et al., Prog. Part. Nucl. Phys. 41 (1998) 225
[74] P. Braun-Munzinger, private communication
[75] J. Stroth, Proceedings on the 15th Winter Workshop on Nuclear Dynamics, January 9-16, 1999, Park City, Utah, p.311

[76] The ALICE collaboration, ALICE TDR 4, CERN-LHCC-99-12

[77] The ATLAS collaboration, ATLAS TDR 4,5,11, CERN-LHCC-97-17, -97-17, -98-13

[78] THE CMS collaboration, CMS TDR-5, CERN-LHCC-98-6

[79] THE LHCb collaboration, LHCb-TDR-5, CERN-LHCC-01-011

[80] TESLA TDR Part IV, http://tesla.desy.de/new_pages/TDR_CD/start.html

[81] F. Hügging et al., Nucl. Instr. Meth. In Phys. Res. A439 (2000) 529

[82] L. Blanquart et al. Nucl. Instr. Meth. In Phys. Res. A439 (2000) 403 (Pixel readout electronics PIRATE chip)

[83] Online compilation by A. Vasilescu (INPE Bucharest) and G. Lindstroem (University of Hamburg), http://sesam.desy.de/~gunnar/Si-dfuncs.html

[84] The RD48 (ROSE) collaboration, Nucl. Instr. Meth. In Phys. Res. A466 (2001) 308

[85] B. Dolgoshein, Nucl. Instr. Meth. in Phys. Res. A326 (1993) 434

[86] B. Yu et al., IEEE Trans. on Nucl. Sci., vol. 38, no.2, (1991) 454

[87] R. Veenhof, Nucl. Instr. Meth. in Phys. Res. A419, pp.726-730, 1998

[88] G.F. Tartarelli, Nucl. Phys. B (Proc. Suppl.) 78, pp.348-353, 1999

[89] TRD Proposal, CERN/LHCC 99-13, available at http://www.gsi.de/~alice

[90] A. Andronic, ALICE TRD Collaboration, nucl-ex/0102017, IEEE Trans. Nucl. Sc. Vol. 48 (Aug.2001)

[91] H.G. Essel and N. Kurz, IEEE Trans. on Nucl. Sci., vol. 47, no.2, (2000) 337

[92] A. Büngener et al., Nucl. Instr. Meth. 214, pp.261-268, 1983

[93] M. Holder and H. Suhr, Nucl. Instr. Meth. in Phys. Res. A263, pp.319-324, 1988

[94] G. Bassompierre et al., Nucl. Instr. Meth. in Phys. Res. A411, pp.63-74, 1998

[95] K. Ackerstaff et al., Nucl. Instr. Meth. in Phys. Res. A417, pp.230-265, 1998

[96] E. Libby et al., Nucl. Instr. Meth. in Phys. Res. A367, pp.2344-247, 1995

[97] K. Zeitelhack et al., Nucl. Instr. Meth. A 433 (1999) 201

[98] J. Friese et al., Nucl. Instr. Meth. A 438 (1999) 86

[99] R. Gernhäuser et al., Nucl. Instr. Meth. A 438 (1999) 104

[100] E. Cerron et al, NIM A 374 (1996) 132

[101] P. Fonte A. Smirnitski and M.C.S. Williams, Nucl. Instr. Meth A 443 (2000) 201

[102] P. Fonte, R. Ferreira-Marques, J. Pinhao, N. Carolino and A. Policarpo, Nucl. Instr. Meth A 449 (2000) 295

[103] A. Akindinov et al., preprint CERN-EP-99-166

[104] P. Camarri, R. Cardarelli, A. Di Ciaccio and R. Santonico, Nucl. Instr. Meth A 414 (1998) 317

[105] Ch. Finck et al., GSI-Annual report (1999) 217

[106] M. Petrovici et al. , submitted to Nucl. Instr. Meth A.

[107] A. Blanco, Ch. Finck, R. Ferreira-Marques, P. Fonte, A. Gobbi, N. Carolino, A. Policarpo and M. Rozas, Conference proceedings VCI2001

[108] A. Blanco, R. Ferreira-Marques, Ch. Finck, P. Fonte, A. Gobbi, N. Carolino, A. Policarpo and M. Rozas, submitted to Nucl. Instr. Meth A.

[109] A. Blanco N. Carolino, P. Fonte, A. Gobbi, submitted to Nucl. Instr. Meth A.

[110] Ch. Finck et al., Proceedings of the XXXIX International Winter Meeting on Nuclear Physics (2001), Bormio.

[111] The Harp collaboration (PS214), CERN-SPSC/99-35 (1999)

[112] ALICE TDR 9, CERN/LHCC 2001-021

[113] R. Brun et al., GEANT3 users guide, CERN-DD/EE/84-1 (1987)

[114] M. Kagarlis, http://www-hades.gsi.de/computing/pluto/html/PlutoIndex.html

[115] Particle Physics Booklet, July 2000, Particle Data Group, http://pdg.lbl.gov/